

COHERENTLY STIMULATED BRILLOUIN SPECTROSCOPY

By Joel N. Johnson

A Dissertation

Submitted in Partial Fulfillment
of the Requirements for the Degree of

Doctor of Philosophy
in Applied Physics and Materials Science

Northern Arizona University

May 2025

Ryan O. Behunin, Ph.D., Co-Chair

Aaron R. Hawkins, Ph.D., Co-Chair

Inès Montaño, Ph.D.

Jennifer S. Martinez, Ph.D.

David Cole, Ph.D.

ABSTRACT
COHERENTLY STIMULATED BRILLOUIN SPECTROSCOPY
JOEL N. JOHNSON

Science is temporal arbitrage; invest in it.

Table of Contents

Abstract	ii
Table of Contents	iv
List of Tables	vi
List of Figures	vii
List of Acronyms	xi
1 Introduction	1
2 Laser Cooling of Traveling-Wave Phonons in an Optical Fiber	7
2.1 Introduction	7
2.2 Optomechanical Cooling	10
2.2.1 Physical Mechanism	10
2.2.2 Spectral Signatures of Cooling and Heating	12
2.3 Methods	15
2.3.1 CS_2 -Filled Liquid-Core Optical Fiber	16
2.3.2 Cooling Experiment A: Spontaneous Brillouin Cooling	17
2.3.3 Cooling Experiment B: Pump-Probe Verification	19
2.4 Results	21
2.4.1 Cooling Experiment A Results	21
2.4.2 Cooling Experiment B Results	25
2.4.3 Evidence of Transmission Degradation	29
2.5 Discussion	34
2.5.1 The C -Value: A Standardized Cooling Metric	34
2.5.2 Parallel Achievement: Max Planck Institute	35
2.5.3 Pathways to Net Cooling	36
2.5.4 Applications to Ground State Cooling	37
2.5.5 Conclusion	38
3 A Coherently Stimulated Phonon Spectrometer	41
3.1 Abstract	41
3.2 Introduction	41
3.3 Theoretical Framework	43
3.3.1 Coherently Stimulated Four-Wave Brillouin Scattering	43
3.3.2 Phase Matching Relaxation	44
3.4 Methods	45
3.4.1 Instrument Design	45
3.4.2 Experimental Techniques	47
3.5 Results	48
3.5.1 Instrument Sensitivity	48
3.5.2 Measurements	50
3.5.3 Phase Matching Bandwidth	53

3.5.4	Fano-Resonant Asymmetries at Small Signals	53
3.6	Conclusion	57
4	Brillouin-Induced Raman Modes and Device Exploration	59
4.1	Introduction	59
4.2	From Traveling-Wave to Raman-Like Standing-Wave Modes	60
4.2.1	Review of Brillouin and Raman Scattering	60
4.2.2	Brillouin-Induced Raman Modes	62
4.2.3	Key Parameters and Feasibility	64
4.3	Results	67
4.3.1	Ge-Doped Optical Fiber	67
4.3.2	Free-Space Optics with Liquid CS ₂	68
4.3.3	TeO ₂ Thin Film	71
4.3.4	Tellurium Thin Film	77
4.3.5	Carbon Disulfide Micrometer Cell	79
4.3.6	Suspended Silica Rib Waveguide	80
4.3.7	Elastically-Suspended Photonic-Phononic Waveguide	81
4.4	Discussion	87
4.4.1	Pathways to Brillouin-Induced Raman Modes	87
4.4.2	Conclusion	88
5	Conclusion	91
A	Supplementary Information for Chapter 2	95
A.1	Fabrication of CS ₂ -Filled Liquid-Core Optical Fiber	95
A.1.1	Splicing	95
A.1.2	Reservoir Assembly	99
A.1.3	Filling with Carbon Disulfide	102
A.1.4	Typical Optical Performance	103
A.2	Improvements in Yield and Efficiency of LCOF Samples	104
A.3	Tabulated Fit and Uncertainty Values Derived from the Observed Data	106
A.3.1	Cooling Experiment A Tabulated Values	106
A.3.2	Cooling Experiment B Tabulated Values	107
B	Supplementary Information for Chapter 3	109
B.1	Coupled-Wave Equations	109
B.1.1	Acoustic Field	110
B.1.2	Optical Fields	111
B.2	Scattered Power Comparison to Traditional Brillouin Scattering Processes	116
B.3	Observance of Fano-Resonant Asymmetries at Small Signals	121
B.3.1	Fano Experiment A: Extended 1 cm UHNA3 Fiber Spectra	121
B.3.2	Fano Experiment B: 1 mm CS ₂ Spectra and Fano Distortions	124
B.4	CoBS Mini Experiment: Equal Contribution of Pump, Stokes, and Probe	130
B.5	Measurement Protocol	133
C	Code and Data Availability	135
C.1	Plotting Data In Go	135
References		136

List of Tables

3.1	Experimental parameters used in observing $P_{\text{Sig}} \approx 5 \text{ fW}$ sensitivity of the Coherently stimulated Brillouin Spectrometer (CoBS) instrument.	50
4.1	Material parameters for TeO ₂ relevant to observing Brillouin traveling-wave modes and Raman standing-wave modes.	72
4.2	Material parameters for Te relevant to observing Brillouin traveling-wave modes and Raman standing-wave modes.	77
4.3	Material parameters for bulk liquid CS ₂ relevant to observing Brillouin traveling-wave modes and Raman standing-wave modes.	80
A.1	Measured anti-Stokes parameters for Experiment A.	106
A.2	Measured Stokes parameters for Experiment A.	106
A.3	Measured anti-Stokes parameters for Experiment B.	107
B.1	Parameters relevant to the coherently stimulated backward Brillouin scattering process for the example Ultra High Numerical Aperture 3 (UHNA3) fiber.	118
B.2	Parameters relevant to the spontaneous and/or stimulated backward Brillouin scattering processes for the example UHNA3 fiber.	119
B.3	Power values for each source (Pump, Stokes, Probe) across the three measurements, with the multiplicative total power for each setup.	130

List of Figures

1.1	Relative domains of typical frequency shifts for Rayleigh, Rayleigh-wing, Brillouin, and Raman scattering.	3
2.1	Illustration of optomechanical heating and cooling processes.	13
2.2	Schematic of liquid-core optical fiber (LCOF) design.	17
2.3	Schematic of experimental setup for Experiment A.	19
2.4	Schematic of experimental setup for Experiment B.	20
2.5	Stokes spectra for a range of pump powers obtained for Experiment A via spontaneous backwards Brillouin scattering.	22
2.6	Anti-Stokes spectra for a range of pump powers obtained for Experiment A via spontaneous backwards Brillouin scattering.	23
2.7	Lorentzian-fitted peak amplitudes of the observed Stokes and anti-Stokes spectra.	24
2.8	Stokes and anti-Stokes linewidths for each pump power, obtained from a lorentzian fit.	25
2.9	A simulated Brillouin gain spectrum G_B ($\text{W}^{-1} \text{m}^{-1}$), obtained from finite element simulations ¹ of the optical and acoustic modes of the LCOF, overtop the lowest power anti-Stokes spectrum	26
2.10	Anti-Stokes probe spectra collected for 0.0 mW intrafiber pump power in Experiment B. . . .	27
2.11	Anti-Stokes probe spectra collected for 22.7 mW intrafiber pump power in Experiment B. . .	28
2.12	Anti-Stokes probe spectra collected for 45.4 mW intrafiber pump power in Experiment B. . .	29
2.13	Anti-Stokes probe spectra collected for 68.0 mW intrafiber pump power in Experiment B. . .	30
2.14	Computed Lorentzian fits from the observed anti-Stokes probe spectra gathered for Experiment B.	31
2.15	Plot of peak spectral density amplitudes for the anti-Stokes spectra gathered for Experiment B.	32
2.16	Plot of the full-width half-max (FWHM) linewidths of the anti-Stokes spectra gathered for Experiment B.	33
3.1	Figure 3.1a illustrates standard (three-wave) stimulated Brillouin scattering.	43
3.2	Design schematic of a coherently stimulated phonon spectrometer.	46

3.3	Observed spectra demonstrating $P_{\text{Signal}} \approx 5 \text{ fW}$ sensitivity of the instrument.	49
3.4	Observed spectra of 1 cm UHNA3 fiber captured at maximum operating optical powers.	51
3.5	Observed spectra of 100 μm liquid CS ₂ captured at maximum operating optical powers.	52
3.6	Spectral peaks of 75 observed spectra of (1 \pm 1) cm UHNA3 across a range of pump-probe detunings.	54
4.1	Conceptual illustration of the transition from a traveling acoustic wave to standing-wave vibrational modes.	62
4.2	Illustration showing how geometry and sound speed of the material determine the allowed acoustic frequencies.	64
4.3	Brillouin gain of investigated materials.	66
4.4	Photographs of 1 cm and 1 mm lengths of UHNA3 fiber.	69
4.5	CoBS measurements of 1 cm and 1 mm UHNA3 fiber, in pursuit of observing Brillouin-induced Raman modes.	69
4.6	Photographs of 1 cm and 4 mm lengths of liquid CS ₂ in the beam path of the CoBS instrument.	70
4.7	CoBS measurements of 1 cm and 4 mm liquid CS ₂	70
4.8	Glass slide with a thin film of TeO ₂ deposited via physical vapor deposition (PVD).	73
4.9	Observed background-subtracted spectrum obtained through a CoBS measurement of 1 μm of TeO ₂	74
4.10	Observed background-subtracted spectra obtained through a CoBS measurement of 1 μm of TeO ₂	75
4.11	Observed background-subtracted spectrum obtained through a CoBS measurement of 500 nm of TeO ₂	76
4.12	Illustration of the material layers of a Te thin film sample.	78
4.13	Evidence of oxidization of the 500 nm Te thin film in the circular beam spot.	78
4.14	Three CS ₂ cells of different path lengths (1 mm, 100 μm , and 10 μm) secured in the beam path of the Coherently stimulated Brillouin Spectrometer.	81
4.15	Observed background-subtracted spectra from 1 mm, 100 μm , and 10 μm liquid CS ₂	82
4.16	CoBS measurement of a suspended silica rib waveguide for a backward scattering process.	83
4.17	CoBS measurement of the elastically-suspended photonic-phononic waveguide for a backward scattering process.	84
4.18	Needle profilometer force-deflection measurements (illustrated above) performed on the suspended polymer membrane of the photonic-phononic waveguide.	86

A.1	Picture of Vytran software interface camera imaging system showing a microscope view of the two fiber ends pre-splice.	96
A.2	Example images of LCOF splices.	97
A.3	Picture of both lengths of fiber braced by folded paper and two Kimwipe boxes.	98
A.4	Picture of splice successfully transferred onto a glass slide and tacked on either side with drops of epoxy.	99
A.5	Picture of a complete splice assembly	100
A.6	Picture of a complete sample under the fume hood with lights dimmed and red laser light injected into the end of the sample for monitoring.	101
A.7	Images of an LCOF sample in the filling process.	102
A.8	Images of a fully finished CS ₂ -LCOF sample.	103
B.1	Comparison of scattered power from a spontaneous Brillouin scattering process and our coherently stimulated Brillouin spectrometer.	119
B.2	All measured Brillouin spectra for 1 cm UHNA3 at detuning steps of 0.5 GHz from 5 GHz to 42 GHz.	123
B.3	All measured Brillouin spectra for 1 mm CS ₂ at detuning steps of 0.25 GHz from 10 GHz to 14 GHz.	125
B.4	Comparison of representative spectra at 11 GHz and 13 GHz, showing the positive vs. negative q asymmetry in 1 mm CS ₂	127
B.5	Comparison of representative spectra at 11 GHz and 13 GHz, showing the positive vs. negative q asymmetry in 1 mm CS ₂	128
B.6	Signal power contributions with error bars representing one standard deviation of the mean for each measurement.	131
B.7	Signal power contributions with error bars extended to two standard deviations of the mean for each measurement.	132

List of Acronyms

AC alternating current

AOM acousto-optic modulator

AMO atomic, molecular, and optical

BPF bandpass filter

BYU Brigham Young University

C Cooling metric

CARS Coherently stimulated Anti-Stokes Raman Scattering

CINT Center for Integrated Nanotechnologies

CoBS Coherently stimulated Brillouin Spectrometer

CW Continuous Wave

DC direct current

EDFA Erbium-Doped Fiber Amplifier

FBG fiber Bragg grating

FP fiber port

FWHM full-width half-max

IM fiber-optic intensity modulator

LCOF liquid-core optical fiber

LO local oscillator

PC polarization controller

PCF photonic crystal fiber

PBS polarizing beam splitter

PVD physical vapor deposition

RBW resolution bandwidth

RF radio frequency

RFSA radio-frequency spectrum analyzer

SBS Stimulated Brillouin Scattering

SMF-28 single mode fiber 28

SNR signal-to-noise ratio

UHNA3 Ultra High Numerical Aperture 3

UHNA7 Ultra High Numerical Aperture 7

VOA Variable Optical Attenuator

WGM whispering-gallery-mode

Chapter 1

Introduction

Optomechanics is the study of light-matter interactions; it is the study of how the intangible (light) can affect change in the tangible (matter) and vice versa. Injecting light into a material under specific conditions allows for an exchange of energy to occur between the light and the mechanical oscillations of the material which changes the mechanical energy of the material. This interaction can be controlled to deposit or withdraw mechanical energy into/from a system and thus leave the system in a more, or less, mechanically energetic state respectively. The same interaction can also be harnessed for passive observation of material properties. Mechanical systems from bulk to atomic scales can be probed and characterized with light by retrieving the inelastically scattered light resulting from interaction with the material. This retrieved light contains embedded information about the energy exchange that occurred, which, when considered as part of a population of scattering events, reveals natural resonances of a mechanical system.

Optomechanics comprises a broad range of phenomena involving the interaction of optical and mechanical systems, from basic photothermal absorption to more complex nonlinear processes. This section offers a brief overview of notable optomechanical phenomena and the remainder of this chapter is devoted to a more detailed description of the specific interactions that play a role in the research detailed in this document. Photothermal absorption is the process by which light is absorbed by a material, leading to an increase in temperature of the material and consequent changes in the material's dimensions (thermal expansion) or refractive index (thermo-optic effect). This effect has applications in optical switches, actuators, and sensors. Photothermal therapy in medicine is an emerging application of this effect, where light is used to target and heat specific areas, causing localized damage to diseased tissue. This technique becomes especially effective when combined with nanoparticle-enhanced absorption, allowing for dramatically increased absorption in ultra-localized zones within the body.

Light scattering, in its many forms, is also an optomechanical process as it involves the interaction of an optical field with the fluctuation, motion, or vibration of matter. Rayleigh scattering, perhaps the most well-known example, is the elastic scattering of light by particles much smaller than the wavelength of the

incident light, leading to scattering in possibly a new direction but without a change in wavelength. It is responsible for the blue color of the sky because the efficiency of Rayleigh scattering is inversely proportional to the fourth power of the wavelength (λ) of the light ($\frac{1}{\lambda^4}$) and so shorter (blue) wavelengths are scattered much more than longer (red) wavelengths by the molecules in the atmosphere.²

Raman scattering is the interaction of light with vibrational and rotational modes within a material (often molecular), resulting in scattered light with frequencies that are shifted from the incident light. This inelastically scattered light provides insights into the material's molecular structure and properties. Raman scattering is widely used in chemical and material science for identifying chemical compounds, analyzing molecular structures, and studying molecular dynamics. It finds application in the characterization of pharmaceuticals, monitoring changes in biological tissues for medical diagnostics, and investigation of stress and temperature distributions in engineering materials, among others.

Brillouin scattering, around which much of the work detailed in this document is centered, is the scattering of light with acoustic phonons or coherent traveling density waves in a material, resulting in scattered light with a frequency that is slightly shifted from the incident light. This inelastically scattered light reveals mechanical properties of the material such as its bulk and elastic moduli. This phenomenon is used in materials science to measure elastic properties and viscoelasticity of materials, in fiber optic sensing to monitor temperature and strain over large distances, and in physics to study phase transitions and mechanical properties of crystals, liquids, and gases.

Rayleigh-wing scattering is the broad, smooth extension of the Rayleigh scattering spectrum that results from interactions with low-frequency excitations in a material, providing insights into dynamic processes like rotational and translational diffusion of molecules that make up a material. This scattering is particularly useful in studying the dynamics of complex fluids, gases, and soft materials, where it can reveal information about molecular orientation, diffusion rates, and interactions within the medium. Applications include the analysis of atmospheric phenomena, characterization of liquid crystals, and investigations into the properties of polymers and biological materials, aiding in the understanding of their behavior at the molecular level.

Figure 1.1 shows the relative domains of typical frequency shifts for Rayleigh, Rayleigh-wing, Brillouin, and Raman scattering. Rayleigh-wing scattering is broad and shares part of its domain with Brillouin scattering. This makes sense because for any given molecule and within the timescale that it occurs, diffusive translational motion can be thought of as indistinguishable from motion caused by traveling density waves that host brillouin scattering. In this way, Rayleigh-wing scattering represents a sporadic distribution of fleeting, localized Brillouin scattering. Of course, the difference between incoherent diffusion of molecules and coherently traveling acoustic modes within a material is an important distinction. However, this thought experiment offers a perspective for bridging the gap between Rayleigh-wing and Brillouin scattering and for

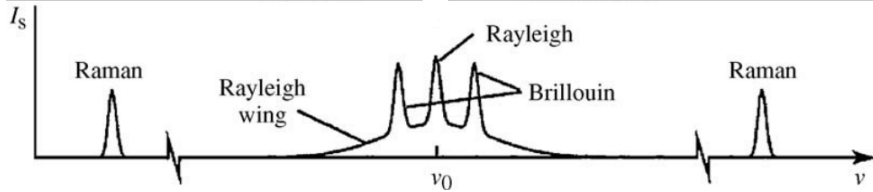


Figure 1.1: Relative domains of typical frequency shifts for Rayleigh, Rayleigh-wing, Brillouin, and Raman scattering. Figure adapted from Boyd Nonlinear Optics (2020).³

understanding their common frequency domains. Moreover, it serves as a reminder of the rich continuum of material behavior and responses that affect light scattering as opposed to the distinct categories we ascribe for convenience. This is a core concept of the research described in further chapters.

Returning to other optomechanical phenomena beyond scattering processes, the momentum of photons can exert forces on objects, leading to phenomena like radiation pressure, optical tweezing, and optical trapping. These effects are widely used in manipulating microscopic particles, biological cells, and atoms, enabling studies of single molecules, cold atoms, and quantum computing elements.

The final category of optomechanical interactions to be noted here is that of nonlinear optical phenomena. Second harmonic generation, parametric oscillation, and four-wave mixing all feature the interaction between light and material nonlinearities that lead to the generation of new light frequencies.³ The Kerr effect is the change in the refractive index of a material in response to an applied electric field, which can be induced optically with sufficient intensities of light. In general, nonlinear optical responses of materials are often only accessible with the use of high intensity laser light. This is emphasized by the fact that the field of nonlinear optics can be traced back to the discovery of second-harmonic generation in 1961⁴, just one year after the first demonstration of the laser by American physicist Theodor Maiman.⁵ These nonlinear effects provide the foundation for a range of technologies, including high-speed optical communication systems, frequency converters, and lasers for materials processing.

Also included within nonlinear optical phenomena is electrostriction. Electrostriction is a reversible material deformation induced by an electric field, which can be generated by light in electro-optic materials. This effect is quadratic, scaling with the square of the applied electric field, and hence a nonlinear optical effect. At sufficiently high intensities, electrostrictive forces serve to enhance Brillouin scattering whereby the scattered light electrostrictively reinforces the acoustic wave that caused its scattering, leading to a nonlinear positive feedback loop known as Stimulated Brillouin Scattering (SBS). Photostriction is a related phenomenon that occurs when light absorption causes a change in the lattice structure of a material, leading to mechanical strain. It combines photovoltaic and piezoelectric effects and can be seen as an optically induced strain. These effects are utilized in designing optical modulators, tunable photonic devices, and

smart materials that respond to light .

Chapter 2

Laser Cooling of Traveling-Wave Phonons in an Optical Fiber

Joel N. Johnson¹², Danielle R. Haverkamp¹², Yi-Hsin Ou³, Khanh Kieu³, Nils T. Otterstrom⁴, Peter T. Rakich⁵, Ryan O. Behunin¹²

This chapter elaborates on experiments and results related to the demonstration of optomechanical cooling of traveling-wave phonons in an optical fiber, which have been published as an article by the same name in Physical Review Applied by Johnson et al. (2023).¹ Any discrepancies, omissions, or errors that may exist between the published paper and this dissertation chapter are the sole responsibility of the author, as the text, analyses, and interpretations herein represent an independent and original presentation of the work.

2.1 Introduction

Over the past half-century, light-based techniques have dramatically reshaped how we control mechanical motion. Laser cooling has become indispensable across many branches of physics, allowing researchers to reduce thermal motion in ions, atoms, and mesoscopic oscillators to previously unimaginable levels. From the earliest proposals and demonstrations of Doppler cooling in dilute gases⁶ to the realization of ultracold quantum gases in Bose–Einstein condensates⁷, the ability to reduce thermal motion with light has profoundly transformed atomic, molecular, and optical (AMO) physics, enabling breakthroughs ranging from high-precision atomic clocks to quantum state preparation⁸. Equally impactful is the extension of laser cooling concepts into solid-state systems. In rare-earth-doped optical crystals, for example, anti-Stokes fluorescence cooling has now approached cryogenic temperatures, cooling Yb-doped solids down to \sim 87 K (the boiling point of liquid argon) and projected to reach 77 K (liquid nitrogen) in the near future.⁹ Such

¹Department of Applied Physics and Materials Science, Northern Arizona University, Flagstaff, AZ 86011, USA

²Center for Materials Interfaces in Research and Applications, Flagstaff, AZ 86011, USA

³College of Optical Sciences, University of Arizona, Tucson, AZ, USA

⁴Photonic and Phononic Microsystems, Sandia National Laboratories, Albuquerque, New Mexico, USA

⁵Department of Applied Physics, Yale University, New Haven, CT, USA

optical refrigeration offers a vibration-free route to cryocoolers and has steadily advanced since the first demonstration in 1995.¹⁰ Meanwhile, in mesoscopic mechanics, radiation-pressure laser cooling of solid-state oscillators has opened new frontiers. By coupling light to discrete mechanical modes in optical or microwave cavities, researchers can damp mechanical vibrations to the point of quantum ground-state occupancy.¹¹ Milestone experiments achieved sub-single-phonon populations in nanomechanical resonators cooled by laser light¹¹, laying the groundwork for quantum metrology and hybrid quantum devices. From AMO systems to solid-state platforms, laser cooling has become a cornerstone technique for reducing thermal noise and accessing novel quantum regimes.

Given this context, there is intense interest in applying laser cooling to optomechanical systems, where light interacts with vibrational modes of a material. The established paradigm in optomechanics involves discrete mechanical oscillators coupled to optical cavities.¹² In a typical cavity-optomechanical system, e.g., a tiny mirror or membrane attached to a cavity, the radiation pressure force provides a parametric coupling between an optical resonance and a mechanical mode.¹² By tuning a laser slightly red of a cavity resonance (i.e. the anti-Stokes sideband), photons can scatter inelastically from the mechanical vibration, gain energy (up-shift) by absorbing a phonon, and promptly leave the cavity, carrying away thermal energy. This sideband cooling process leads to a reduced phonon population in the mechanical mode, provided the anti-Stokes scattering dominates over the Stokes (down-shift) process that would add phonons. Using this approach, a variety of mechanical oscillators from gram-scale mirrors to nanoscale beams have been cooled near their ground state of motion.¹¹ A landmark example is the laser cooling of a 3.7 GHz silicon nanobeam mode to an average occupancy of $\langle n \rangle \approx 0.85$ (15% of one quantum) starting from 20 K environment.¹¹ Such achievements, along with comprehensive theoretical frameworks¹², firmly established the state-of-the-art: *discrete* mechanical modes can be laser-cooled via engineered light-matter interactions in optical cavities.

Early optomechanical cooling experiments focused on isolated resonant modes, but recent work has pushed toward cooling a *continuum* of vibrational degrees of freedom, in particular, traveling-wave phonons in extended media. One route to bridging this gap is to use whispering-gallery-mode (WGM) microresonators, which support both localized optical modes and traveling acoustic waves confined around the periphery. In 2012, Bahl et al. demonstrated the first observation of Brillouin optomechanical cooling in a silica microcavity.¹³ In that system, light circulating in the WGM resonator underwent spontaneous Brillouin scattering with an acoustic whispering-gallery wave. Because the scattering was in the forward direction (co-propagating light and sound), it accessed a low-frequency acoustic mode that had much lower damping than the usual high-frequency phonons of spontaneous backscattering. Satisfying this low acoustic dissipation condition (achieving phonon lifetimes longer than the optical storage time) allowed the optical field to cool the mechanical mode rather than amplify it. The experiment revealed two regimes: the normal Stokes

process where light amplifies acoustic vibrations, and a Brillouin cooling regime where anti-Stokes scattering dominantly *damps* the acoustic motion. This result was remarkable since Brillouin interactions in bulk or fiber had long been known primarily as a heating (Stokes) process; the microresonator provided the multi-mode, low-loss environment needed to tip the balance towards net cooling.

Even more surprising was the recent demonstration that one can cool a continuum of phonon modes in a completely non-resonant, traveling-wave configuration.¹⁴ Otterstrom et al. (2018) showed for the first time that laser cooling is possible in a continuous optomechanical waveguide, without any optical cavity or discrete mechanical resonance. In their experiment, light propagating through a 2.3 cm silicon photonic waveguide was observed to reduce the thermal occupancy of a band of acoustic phonons via Brillouin scattering. The key was to leverage intermodal Brillouin scattering, wherein the pump laser in one waveguide mode scatters to an anti-Stokes photon in a different optical mode while annihilating a phonon. This phase-matched anti-Stokes process selectively damped those phonons, cooling a spectral band by over 30 K relative to room temperature. Conceptually, the continuous-waveguide regime has an inherent advantage: the Stokes (phonon-creating) and anti-Stokes (phonon-annihilating) processes occur on different phonon modes in an extended medium. Thus, any unavoidable Stokes scattering does not re-excite the very phonon mode being cooled, avoiding the direct competition that limits cooling of a single isolated mode. Still, achieving net cooling in a traveling-wave system demands stringent conditions. The optical wave must interact sufficiently strongly with the acoustic waves (high acousto-optic coupling), and the phonons must remain dissipated long enough for the cooling scattering to outpace thermal re-population and for the light to exit the system carrying that stolen mechanical energy with it. In the silicon waveguide used by Otterstrom et al., engineered cross-section geometry provided large Brillouin gain, and the small device length ensured that anti-Stokes photons escaped the system faster than the phonons could dissipate, fulfilling these requirements.¹⁴ This demonstration has spurred growing interest in continuous optomechanical cooling, including new theoretical proposals to dynamically control phonon baths in waveguide systems.¹⁵

Laser cooling of traveling-wave phonons in an optical fiber is a natural next goal in this progression. Optical fibers represent the quintessential one-dimensional continuous medium for light and sound, with applications ranging from fiber lasers to quantum information transfer. Cooling phonons in fiber could, for example, suppress thermally driven noise (e.g. guided-acoustic-wave Brillouin noise) that limits the frequency stability of fiber lasers and squeezes light in fiber interferometers.¹⁶ It could also enable new in-fiber acousto-optic devices with reduced thermal noise, or even allow one to prepare traveling phonon wavepackets in low-entropy states for quantum phononics. However, extending optomechanical cooling to standard fibers poses several distinct challenges that were absent in chip-scale or microresonator systems. First, conventional single-mode fibers have relatively weak light–sound coupling. The Brillouin gain coefficient g_B in fused silica

fiber is on the order of $5 \times 10^{-11} \text{ m W}^{-1}$,^{17,18} many orders of magnitude smaller than in highly confinement-enhanced waveguides (such as silicon nanowires or resonant structures). This means achieving appreciable anti-Stokes scattering in a fiber typically requires either very long interaction lengths or high optical power.

Secondly, the acoustic modes in a fiber have finite lifetimes that can be quite short, especially for the high-frequency phonons usually involved in Brillouin scattering. In backwards spontaneous Brillouin scattering with a 1.5 μm pump, these phonons are typically $\sim 9\text{-}12 \text{ GHz}$ sound waves in silica, which experience significant acoustic damping (linewidths of tens of MHz) and thus live only on the order of nanoseconds.¹⁹ Such brief phonon lifetimes make it difficult to achieve net cooling: the anti-Stokes process must remove phonons faster than they are thermally replenished. Essentially, one needs phonon Q - (quality) factors high enough that the phonon lifetime exceeds the transit time of light through the interaction region. Meeting this condition in a meter-scale fiber (where light transit is only a few nanoseconds) is non-trivial. Prior experiments in resonators or short waveguides addressed this by using lower-frequency acoustic modes with inherently longer lifetimes¹³ or by effectively shortening the optical interaction length, but in a long fiber the default acoustic damping is too strong to allow cooling in the usual Brillouin regime.

These challenges help explain why, until now, laser cooling of phonons had not been realized in a fiber; no prior studies have achieved phonon cooling in an optical fiber. This chapter details how we overcome these obstacles and presents the results we achieved. By using a specially engineered liquid-core fiber platform, we satisfy the acousto-optic coupling and phonon dissipation requirements and achieve over 20 K of cooling in an optical fiber with modest pump power. This marks the first demonstration of laser cooling of a continuum of phonons in fiber and extends the reach of optomechanical cooling to macroscopic length scales. Through this work, we bridge the gap between chip-scale optomechanics and fiber optics, enabling new low-noise acousto-optic technologies and fundamental studies of traveling-wave phonons in the quantum regime.

2.2 Optomechanical Cooling

2.2.1 Physical Mechanism

Optomechanical laser cooling can be viewed as a coupling between a discrete or traveling-wave phonon mode and an external reservoir capable of removing vibrational energy. When light interacts with sound through anti-Stokes scattering (where photons are upshifted in frequency by absorbing phonons), the optical field acts as an effective “damping channel,” allowing mechanical excitations to exit the system in the form of higher-energy scattered photons. This additional pathway for phonon annihilation increases the net decay rate of the targeted mechanical mode, thereby reducing its occupation number below the thermal equilibrium level. Conceptually, one can think of this interaction much like placing a fingertip on a vibrating bell: the bell

(analogous to the mechanical mode) is no longer isolated but is now coupled to a broader set of mechanical modes in one’s hand, enabling rapid dissipation of vibrational energy into the surroundings. In laser cooling, the “finger” is replaced by the optical continuum associated with the anti-Stokes scattering process, which carries away phonon energy in the form of upshifted photons rather than mechanical vibrations.

This coupling arises from momentum and energy conservation between the pump photon at frequency ω , the phonon at frequency Ω , and the scattered photon at $\omega + \Omega$. Although the pump itself may be extremely narrow in linewidth, its interaction with the phonon mode broadens the resulting scattered light analogous to how a short-lived mechanical oscillator necessarily exhibits a broader frequency spectrum. The faster the phonon mode decays via anti-Stokes scattering, the more rapidly the mechanical amplitude (phonon occupation) drops, and thus the “effective” linewidth of that mode broadens. In other words, the very mechanism that damps the phonon occupation also manifests as a broadened distribution of scattered photon frequencies centered at $\omega + \Omega$. This is again analogous to the finger placed on the vibrating bell: the mechanical-mechanical coupling of the finger to the bell damps the bell’s vibration by offering a broad continuum of mechanical modes (a mechanical bath) for the bell’s vibration to dissipate into. Left behind in the finger is a broad distribution of mechanical modes, with the linewidth of this mechanical frequency distribution corresponding to the rate of damping (dissipation rate). Likewise, the applied optical field (laser) *opto*-mechanically couples to the phonon mode, lowering the phonon occupancy of the mechanical mode by offering a broad continuum of *optical* modes (a “light bath”) for the phonons to dissipate into. Produced in the scattered light is a broad distribution of *optical* modes, with the linewidth of this optical frequency distribution indicating the dissipation rate of the phonon mode.

Importantly, this does not require the intrinsic mechanical properties of the medium to change. Instead, once the optical field is present, the formerly isolated mechanical mode sees a new “escape route” for its energy. In a parametric picture, the simultaneous conservation of energy and momentum among the three waves enables phonons to be converted into higher-frequency photons that promptly leave the system, carrying away the vibrational quanta. The result is an enhanced net decay rate: intrinsic mechanical damping of the host medium plus the new optical damping channel coupled to the system. If these processes occur faster than the phonons can be re-supplied by thermal fluctuations (the natural dissipation rate of the medium), the phonon population is driven to a lower effective temperature.

While anti-Stokes scattering provides the mechanism for laser cooling, the inverse Stokes heating process simultaneously occurs. Spontaneous backward Brillouin scattering interacts with longitudinally traveling acoustic waves (phonons) according to both of these complementary processes, but the specific phonon mode is distinct for each. Figures 2.1a and 2.1b offer respective illustrations of these Stokes and anti-Stokes scattering processes. In the Stokes process, an incident pump photon scatters with a *retreating*

phonon, annihilating the *photon* and creating both an additional phonon and a backscattered photon at the difference energy. Both energy and momentum must be conserved for this process, demanding these Stokes components satisfy

$$\omega_S = \omega_P - \Omega, \quad -k_S = k_P + q, \quad (2.1)$$

where ω_S , ω_P , and Ω are the angular frequencies of the Stokes, pump, and phonon waves, respectively, and k_S , k_P , and q are their corresponding wavevectors. This can be understood by analogy of the incident light experiencing a doppler *down-shift* in frequency as though the photon were reflected from a *retreating* mirror (phonon). The Stokes processes results in increased phonon occupancy of the respective longitudinal mode of the material, and thus this process results in optomechanical heating. Optical energy is donated to the material in the form of mechanical (thermal) energy.

The anti-Stokes process is the inverse process (Figure 2.1b), whereby an *approaching* phonon scatters with a pump photon, annihilating the *phonon* and creating a backscattered photon at the additive energy. In the anti-Stokes process, the incident light experiences a doppler *up-shift* in frequency as if, to continue the analogy, the photon were reflected from an *approaching* mirror (phonon). Phase matching requirements demand the anti-Stokes components satisfy

$$\omega_{aS} = \omega_P + \Omega, \quad -k_{aS} = k_P - q, \quad (2.2)$$

where ω_{aS} and k_{aS} are the respective angular frequency and wavevector of the backscattered anti-Stokes light.

2.2.2 Spectral Signatures of Cooling and Heating

Optomechanical cooling reduces the phonon occupation of a given mechanical mode. Evidence of this phenomenon is offered by changes in two key spectral features of the backscattered light: linewidth and amplitude. Spectral linewidth is a measure of the mechanical dissipation rate of the phonon mode. A broader linewidth corresponds with a faster mechanical dissipation rate of a given mode as per the time-energy uncertainty principle: greater dissipation means shorter phonon lifetime, which introduces an uncertainty in the phonon frequency. Thereby, increasing the dissipation rate (cooling) broadens the spectral linewidth; conversely, decreasing the dissipation rate (heating) narrows the spectral linewidth. For spontaneous Brillouin



Figure 2.1: Illustration of optomechanical heating and cooling processes. Figure 2.1a shows an incident photon of frequency ω scattering with a retreating phonon of frequency Ω , resulting in the annihilation of the incident photon and the creation of both an additional retreating phonon of frequency Ω and a backwards propagating photon down-shifted in frequency ($\omega_{\text{Stokes}} = \omega - \Omega$). Figure 2.1b shows the inverse process, whereby an incident photon, ω , scatters with an approaching phonon, Ω , annihilating the incident photon and the phonon to produce a backwards propagating photon up-shifted in frequency ($\omega_{\text{anti-Stokes}} = \omega + \Omega$).

scattering this is given by¹⁴

$$\Gamma_{\pm} \approx \Gamma_0 \left(1 \pm \frac{G}{4} \right), \quad (2.3)$$

where Γ_0 is the mechanical dissipation rate at thermal equilibrium, Γ_{\pm} is the effectively broadened (+) or narrowed (-) dissipation rate due to an anti-Stokes or Stokes process, respectively. Here, G is the Brilouin scattering process gain factor $G = G_B P_P L$, where G_B is the effective Brilouin gain ($\text{W}^{-1} \text{m}^{-1}$), P_P is the pump power, and L is the effective length (see Section B.2 in Appendix B). Equation 2.3 is related to the effective temperature change of the mechanical mode via the quantized phonon dissipation rate (phonons dissipated per second) at equilibrium, given by

$$Q = n_{\text{th}} \Gamma_0, \quad (2.4)$$

where Γ_0 is the mechanical dissipation rate at thermal equilibrium and n_{th} is the mean thermal occupancy (phonon count) of the mode at equilibrium given by the Bose distribution,

$$n_{\text{th}} = \frac{1}{e^{\frac{\hbar \Omega_B}{k_B T_0}} - 1}. \quad (2.5)$$

Here, $\hbar = h/2\pi$ is the reduced Planck constant, Ω_B is the angular phonon frequency, k_B is the Boltzmann constant, and T_0 is equilibrium (room) temperature in kelvin. Laser cooling of the phonon mode increases the effective dissipation rate of the mode by offering a new escape channel by which phonons may exit the mode (converting to the optical domain). This altered dissipation rate gives the effective temperature via Equation 2.4,

$$n_{\text{eff}}\Gamma_{\pm} \approx n_{\text{th}}\Gamma_0, \quad (2.6)$$

where n_{eff} is the effective phonon mode occupancy of the cooled (+, widened dissipation rate) or heated (-, narrowed dissipation rate). For GHz phonon frequencies near room temperature, $k_B T \gg \hbar\Omega_B$, allowing the first order approximation

$$e^{\frac{\hbar\Omega_B}{k_B T}} \approx 1 + \frac{\hbar\Omega_B}{k_B T}, \quad (2.7)$$

which gives, for Equation 2.5,

$$n_{\text{th}} \approx \frac{k_B T_0}{\hbar\Omega_B}. \quad (2.8)$$

Inserting this approximation in Equation 2.6, and in combination with Equation 2.3, we find two independent approximations for the ratio of effective to equilibrium temperatures of the cooled phonon mode,

$$\frac{\Gamma_+}{\Gamma_0} \approx \frac{T_0}{T_{\text{eff}}} \approx 1 + \frac{G}{4}. \quad (2.9)$$

Rearranging for fractional degrees cooled ($\Delta T/T_0$), where $\Delta T = T_{\text{eff}} - T_0$ is degrees cooled from equilibrium, we find (to first order approximation)

$$\frac{\Gamma_+}{\Gamma_0} - 1 \approx \frac{\Delta T}{T_0} \approx \frac{G}{G + 4}. \quad (2.10)$$

Spectral amplitude provides additional evidence of optomechanical cooling. Spectral amplitude is a measure of the scattered power produced from pump light scattering with phonons occupying a given mechanical

mode. Higher phonon occupancy within a given mode provides a higher rate of scattering and thus a higher measured spectral amplitude of the backscattered light. Increasing pump power reduces the phonon population occupying the anti-Stokes mode and thereby lessens the otherwise scattered power, measured as spectral amplitude. The inverse process occurs for the Stokes process; increasing pump power increases the phonon population occupying the Stokes mode and thereby increases the otherwise scattered power, measured from spectral amplitude.

In the spontaneous Brillouin scattering process, however, scattered power increases not only with phonon population (linked to temperature via Equation 2.5), but also with pump power P_P (see Equation B.50 in Appendix B.2). As a result, both the Stokes and anti-Stokes spectral amplitudes increase with increasing pump power. Despite this, however, spectral amplitudes still provide evidence of laser cooling. Asymmetric growth rates of the relative Stokes and anti-Stokes spectral amplitudes with increasing pump power indicate underlying cooling of the anti-Stokes phonon mode relative to the Stokes. The anti-Stokes scattering process (phonon annihilation) leads to a sublinear growth trend in peak spectral amplitude even as increasing pump power raises the overall peak amplitude. Conversely, the Stokes scattering process (phonon creating) leads to a superlinear growth trend in peak spectral amplitudes as pump power raises. These divergent trends in peak spectral amplitudes are a direct result of the optomechanically-induced altering of the thermal state of the respective modes and provide key evidence of laser cooling.

To expand on this, one might imagine a process whereby a pump laser cools a medium through the anti-Stokes process while an independent probe laser is simultaneously co-injected and allowed to scatter with the same phonon mode being cooled by the pump. In this pump-probe arrangement, increasing pump power induces further cooling of the anti-Stokes mode just as before, but with the addition of a probe that may be held at constant power. Critically, while backscattered *pump* light would still feature an overall growth trend in peak spectral amplitude (proportional to pump power), scattered power of the *probe* would only be sensitive to the underlying phonon occupancy (temperature) of the mode. As such, for the anti-Stokes (cooling) process, peak amplitudes of the probe spectra would actually be seen to *decrease* with increasing pump power, commensurate with the mode being increasingly cooled by the pump. As such, this pump-probe spectroscopy regime offers a direct measure of phonon occupancy, and thus direct and independent confirmation of laser cooling occurring.

2.3 Methods

While spontaneous Brillouin scattering processes naturally alter phonon populations (and thus mode temperatures), practical demonstration and detection of these effects pose significant challenges. Foremost among

these is the requirement to remain in the spontaneous regime: we wish to probe the natural thermal phonons in a medium, so we cannot rely on artificially driving the mechanical modes to enhance scattered power (see Appendix B.2, and specifically Figure B.1, for a comparison of scattered power produced by different Brillouin techniques). Although stimulated Brillouin scattering (SBS) is often employed to boost signal levels, it actively drives phonon populations via injected optical fields, and thus no longer measures the intrinsic thermal phonons. In practical terms, SBS occurs when the overall process gain factor $G = G_B P_P L$ (where G_B is the effective Brillouin gain, P_P the pump power, and L the effective length) far exceeds unity ($G \gg 1$).

To demonstrate optomechanical cooling (i.e., an anti-Stokes process that lowers phonon energy), one must detect scattered light from a mode whose phonon population has been reduced. This is intrinsically difficult because a decreased phonon population means fewer scattering events, and hence diminished backscattered light. Consequently, an ideal testbed should provide sufficiently high single-pass gain (overall gain factor near unity) to enable clear detection, yet remain below the threshold that would drive the process into the stimulated regime. Although the Stokes and anti-Stokes processes address distinct phonon modes in a traveling-wave system, allowing any mode to become stimulated generates large driven phonon populations that can obscure or counteract spontaneous cooling. Achieving this balance ensures that measurements reflect genuine spontaneous cooling of a thermally populated phonon mode, rather than an artifact of optically driven phonons.

In addition to the requirement that the overall process gain be near but below unity, temporal constraints impose further critical conditions. Specifically, the rate at which phonons are removed from the system must exceed the rate at which they are replenished by the thermal bath to ensure net cooling of the anti-Stokes mode. This condition demands that backscattered photons leave the system rapidly, carrying away the extracted mechanical energy. A mean-field analysis (see Appendix A of Johnson et al. (2023)¹) shows that the relevant depletion rate is $4v_g/L$, where v_g is the group velocity of the anti-Stokes light and L is the system length. This must exceed the mechanical dissipation rate Γ_0 , which represents the natural return of the phonon mode to thermal equilibrium. Hence, a suitable platform for demonstrating optomechanical cooling of traveling-wave phonons must fulfill the fast escape condition $4v_g/L > \Gamma_0$. Meeting this requirement on system length, however, directly conflicts with the desire for a sufficiently high overall gain factor, illustrating the delicate balance needed for effective cooling.

2.3.1 CS_2 -Filled Liquid-Core Optical Fiber

To demonstrate optomechanical cooling of traveling wave phonons, we utilize 1 m of liquid-core optical fiber filled with carbon disulfide, first developed by Kieu et al. (2012).²⁰ This platform features large optomechani-



Figure 2.2: Schematic of liquid-core optical fiber (LCOF) design. A length of single mode fiber 28 (SMF-28) is arc-spliced to 5-10 cm of Ultra High Numerical Aperture 7 (UHNA7) fiber, with a post-arc process applied to taper the larger SMF-28 core down to the smaller UHNA7 core for better mode matching and coupling efficiency. The UHNA7 fiber is angle-cleaved and fusion-spliced to a flat-cleaved hollow-core fiber via a heated filament in a Vytran fusion splicer system. The angle cleave results in a splice that only partially fuses the two fibers, leaving a pathway for liquid to enter the hollow core fiber via capillary action once submerged. A mirrored splice configuration on the other end of the length of hollow-core fiber allows air to escape as the fiber fills, and a reverse taper again provides improved mode matching for the light to recouple into SMF-28.

cal coupling due to the high electrostrictive response of CS_2 ³ and the small effective area defining acousto-optic mode overlap offered by the small $0.9 \mu\text{m}$ core radius of the capillary fiber. These characteristics of the LCOF system combine to produce an effective Brillouin gain coefficient greater than $G_B = 2 \text{ W}^{-1} \text{ m}^{-1}$, enabling sufficient scattering within the relatively short length required to satisfy the fast-escape condition $4v_g/L > \Gamma_0$ ($4v_g/L \approx 0.82 \text{ GHz}$ and $\Gamma_0 \approx 2\pi \times 97 \text{ MHz} \approx 0.61 \text{ GHz}$).¹ Additionally, this CS_2 -filled LCOF system provides excellent acoustic and optical guidance due to the large electromagnetic and acoustic impedance differential between the CS_2 core and surrounding silica.²¹

Figure 2.2 shows a schematic of the LCOF design. Coupling into and out of the LCOF is facilitated by a short length of tapered UHNA7 for better mode matching between the $4.8 \mu\text{m}$ core radius SMF-28 and the $0.84 \mu\text{m}$ core radius of the capillary fiber. An angled cleave of the UHNA7 fiber allows for a small wedge gap to remain after fusion splicing to the capillary fiber. This gap allows liquid CS_2 to enter and fill the hollow core of the fiber via capillary action. Appendix A.1 describes the fabrication and filling processes of the LCOF and details key insights which contributed to significant reductions in failure rate as well as time and material cost of sample preparation.

2.3.2 Cooling Experiment A: Spontaneous Brillouin Cooling

We conducted two independent experiments to demonstrate and verify laser cooling of traveling wave phonons in our CS_2 -LCOF platform. The first experiment (Experiment A) employs a pump laser to launch $1.55 \mu\text{m}$

light into the LCOF. The backscattered Stokes and anti-Stokes components are filtered and collected by a detector. In this experiment, evidence of cooling is given by symmetry breaking between the amplitudes and widths of the Stokes and anti-Stokes spectra as pump power is varied. Backscattered pump light is shifted in frequency by a band of frequencies centered at the resonant Brillouin frequency of the LCOF ($\Omega_{B,LCOF} \approx 2\pi \times 2.27 \text{ GHz}$).

These backscattered signals exhibit a spectral linewidth corresponding to the mechanical dissipation rate in the phonon mode (conversely, finite phonon lifetime). The polarization state of the backscattered pump and probe light is recovered after retracing their paths, permitting only probe light to transmit through the polarizing beam splitter (PBS) for filtration and heterodyne detection. Output from the detector is again amplified by an radio frequency (RF) amplifier and routed to an radio-frequency spectrum analyzer (RFSA) for data collection. With the probe power inside the LCOF held constant, changes in the amplitude and width of the probe spectra provide direct evidence of laser cooling from varying pump powers within the LCOF.

Figure 2.3 shows a schematic diagram of the experimental setup for Experiment A. A Continuous Wave (CW) pump laser emitting at $1.55 \mu\text{m}$ (ω_P) is amplified by an Erbium-Doped Fiber Amplifier (EDFA) and its power is controlled by a Variable Optical Attenuator (VOA). This light is subsequently routed via a circulator to the CS_2 -LCOF, where some of the light backscatters within the length of the LCOF. Backscattered light is frequency-shifted, up for anti-Stokes ($\omega_{AS} = \omega_P + \Omega_B$) and down for Stokes ($\omega_S = \omega_P - \Omega_B$), by a band of frequencies centered around the Brillouin frequency of the LCOF ($\Omega_{B,LCOF} \approx 2.27 \text{ GHz}$). Backscattered light is routed by circulators to a 5 GHz bandpass filter (BPF) to allow selection of either the Stokes or anti-Stokes light while also reducing unwanted frequency noise. The filtered signal is then incident on a photodiode detector sensitive to GHz frequencies. A local oscillator (LO) is synthesized from the pump laser, polarization controlled, amplified, and combined with the signal pre-detector for heterodyne detection. Output from the detector is amplified with a RF amplifier and sent to a RFSA for data collection.

To conduct the experiment, pump power was varied from 10 mW to 290 mW in increments of 10 mW , as measured pre-injection into the LCOF, and respective Stokes and anti-Stokes spectra for each pump power were collected sequentially by tuning the placement of the BPF. For both the Stokes and anti-Stokes modes, five repeated measurements of each spectra and the background (pump off) were collected for each pump power, with each measurement comprising an average over $100 - 250 \text{ ms}$ sweeps at a resolution bandwidth (RBW) of 1 MHz . Optical transmission through the entire LCOF sample which was used for the published data was measured to be 17% , giving $100\sqrt{0.17} \approx 41\%$ transmission through just the first splice assuming equal transmission through both LCOF splices. This provided a scaling factor for obtaining intrafiber powers from injected pump power ($P_{\text{intrafiber}} = \sqrt{0.17}P_P$) which was used for data processing and

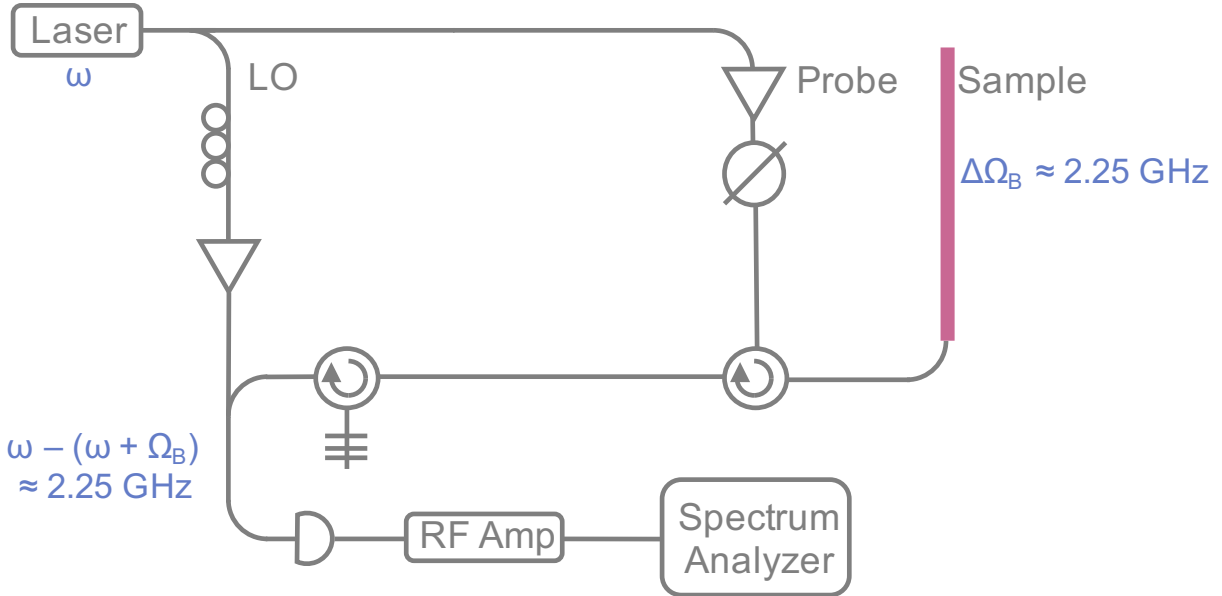


Figure 2.3: Schematic of experimental setup for Experiment A. In this experiment, a CW pump laser emitting at $1.55 \mu\text{m}$ is amplified, passed through a circulator, and injected into the CS_2 -LCOF. Backscattered light is routed to a BPF for selection of Stokes or anti-Stokes frequencies and sent to a detector. A LO is synthesized from the pump laser for heterodyne detection, whereby a polarization controller is used to align the polarization of the LO to that of the backscattered signal. The signal passes through a radio frequency amplifier before being sent to a RFSA for collection. Pump power is controlled by a VOA placed just after the EDFA. Stokes and anti-Stokes spectra are collected sequentially for each pump power by adjusting the placement of the BPF.

analysis for the publication.

2.3.3 Cooling Experiment B: Pump-Probe Verification

A second experiment (Experiment B) was conducted to provide direct evidence of cooling via pump-probe spectroscopy, whereby a separate probe laser is held at constant power while a pump laser is varied to affect cooling in the LCOF. In Experiment B, backscattered light from the probe laser provides direct evidence of cooling through spectral changes in amplitude and linewidth as pump power is independently varied. To achieve independence of the pump and probe, probe light was controlled to be polarized orthogonal to the pump.

Figure 2.4 shows a schematic of the experimental design for Experiment B. Starting from a single CW laser operating at $1.55 \mu\text{m}$, we generate a pump ω_P , probe ω_{P_r} , and LO. A PBS combines the pump and probe for co-injection into the LCOF. The pump light is amplified by an EDFA, and its polarization is adjusted so that it reflects at the PBS for launching into the LCOF. The probe light passes through a circulator and is polarization-adjusted to transmit through the PBS for injection into the LCOF. A 99-1



Figure 2.4: Schematic of experimental setup for Experiment B. A pump, probe, and LO are generated from a single CW laser operating at $1.55\text{ }\mu\text{m}$. Pump light is amplified and directed through a VOA and polarization controller (PC), where its polarization is adjusted to reflect at the PBS. Probe light passes through a VOA for careful power control across measurement sets before being routed by a circulator to the PBS. Polarization of the probe light is adjusted for transmission through the PBS for co-injection with the pump into the LCOF. A 99-1 splitter directs 1% of the total pump and probe light to a second PBS for monitoring of respective powers injected into the LCOF. Backscattered Stokes and anti-Stokes components of both the pump and the probe retrace to the first PBS, where the respective polarization states of each ensure a re-separation of backscattered pump and probe light. The probe light is filtered by a tunable BPF and heterodyned with the LO prior to detection. Detector output is amplified by an RF amplifier and fed to an RFSA for data collection.

splitter directs 1% of the combined pump and probe light to a second PBS for monitoring of respective powers injected into the LCOF.

Backscattered light from both the pump and the probe is shifted in frequency by approximately the Brilouin frequency of the LCOF ($\Omega_{\text{B,LCOF}} \approx 2.27\text{ GHz}$). The frequencies and wavevectors involved in both the pump and the probe scattering processes satisfy similar phase matching conditions given by Equation 2.2. Because this pump-probe technique provides a direct measure of laser cooling, only the anti-Stokes spectra need to be collected. In conducting the experiment, five repeated measurements of both the anti-Stokes spectra and the background (pump off) were collected for each pump power, with each measurement comprising an average over 100 250 ms sweeps at a RBW of 1 MHz.

Notably, this experiment relies on careful control of the polarization states of the pump and the probe. Upon backscattering within the LCOF, their respective polarization states are recovered after retracing their paths to the PBS, which ensures only probe light transmits through the PBS for filtration and heterodyne detection. Output from the detector is amplified by an RF amplifier and routed to an RFSA for data

collection. In this way, by holding the probe power inside the LCOF constant, changes in the amplitude and width of the backscattered probe spectra provide direct and independent evidence of laser cooling from varying pump powers within the LCOF.

2.4 Results

2.4.1 Cooling Experiment A Results

Figures 2.5 and 2.6 show the respective Stokes and anti-Stokes spectra gathered across a range of intra-fiber pump powers, from 4.12 mW to 119.57 mW. Both Stokes and anti-Stokes spectra sets are centered at approximately $f_B = 2.27$ GHz, representing the respective up- and downshift from the pump frequency by the Brillouin frequency of the CS₂-LCOF at 1.55 μm. For increasing pump power, we see an asymmetry in evolution of peak spectral densities and of the Stokes and anti-Stokes spectra, a key fingerprint of optomechanical cooling. Figure 2.7 plots the lorentzian-fitted Stokes and anti-Stokes peak amplitudes for each pump power. A dashed line showing a linear trend was obtained by applying a linear fit of all data points. Solid lines show the theoretical super- and sublinear scattered power for the Stokes and anti-Stokes processes, respectively, and were calculated using Equations A27 and A28 in Appendix A of Johnson et al. (2023)¹. Figure 2.7 shows that peak amplitudes of both processes are in good alignment of the theoretical trend, with anti-Stokes peaks increasing sublinearly and Stokes peaks increasing superlinearly.

This is consistent with one of the key signatures of laser cooling: as higher pump powers further reduce the phonon occupation within the anti-Stokes mode (cooling), scattered power falls farther short of the otherwise linear relationship with pump power (Equation B.50). This sublinear trend in scattered power produces the same trend in backscattered light incident on the detector and reveals itself in the data as a sublinear trend in peak spectral density with increasing pump power. The opposite effect occurs in the Stokes process; as higher pump powers further increase the phonon occupation within the Stokes mode (heating), scattered power rises further above the otherwise linear relationship with pump power (again given by Equation B.50). This superlinear trend in scattered power produces the same trend in backscattered light incident on the detector and reveals itself in the data as a superlinear trend in peak spectral density with increasing pump power. These respective super- and sublinear growth trends in peak amplitudes of the Stokes and anti-Stokes spectra as pump power increases provide a spectral fingerprint of optomechanical cooling of the anti-Stokes phonon mode within the LCOF.

Linewidths of the spectra shown in Figures 2.5 and 2.6 also exhibit key spectral signatures of laser cooling (and heating for the Stokes mode). With increasing pump power, the linewidths of the anti-Stokes spectra broaden, indicating a higher dissipation rate of phonons into the “optical bath” (cooling). The inverse



Figure 2.5: Stokes spectra for a range of pump powers obtained for Experiment A via spontaneous backwards Brillouin scattering. Intrafiber pump powers are displayed and were calculated from a measurement of 17% total through-fiber transmission and assuming equal losses through each of the two splices bookending the LCOF. To obtain each spectra, five repeated measurements of both the Stokes spectra and the background (pump off) were collected for each pump power, with each measurement comprising an average over 100 250 ms sweeps at a RBW of 1 MHz. Plotted are the resulting background-subtracted spectra, with uncertainties smaller than the data point markers.

trend is seen for the Stokes mode: with increasing pump power, the linewidths of the Stokes spectra narrow, indicating a reduced phonon dissipation rate (heating). Figure 2.8 plots the Stokes and anti-Stokes linewidths for each pump power, obtained from a lorentzian fit. Solid lines provide a linear fit to the respective Stokes and anti-Stokes measured linewidths. The secondary y-axis provides a temperature scale in degrees K, with room temperature (taken to be 293 K) centered at the equilibrium linewidth of the LCOF. Section A.3.1 provides a tabulation of the extracted fit parameters and their associated uncertainties for each of the Stokes and anti-Stokes spectra for all pump powers.

Using Equation 2.3 and the respective broadened and equilibrium anti-Stokes linewidths at the highest intrafiber pump power ($\Gamma_{P_P} = 119.57 \text{ mW} = 106.32 \text{ MHz}$) as compared to the lowest ($\Gamma_{P_P} = 4.12 \text{ mW} = 97.3 \text{ MHz}$),

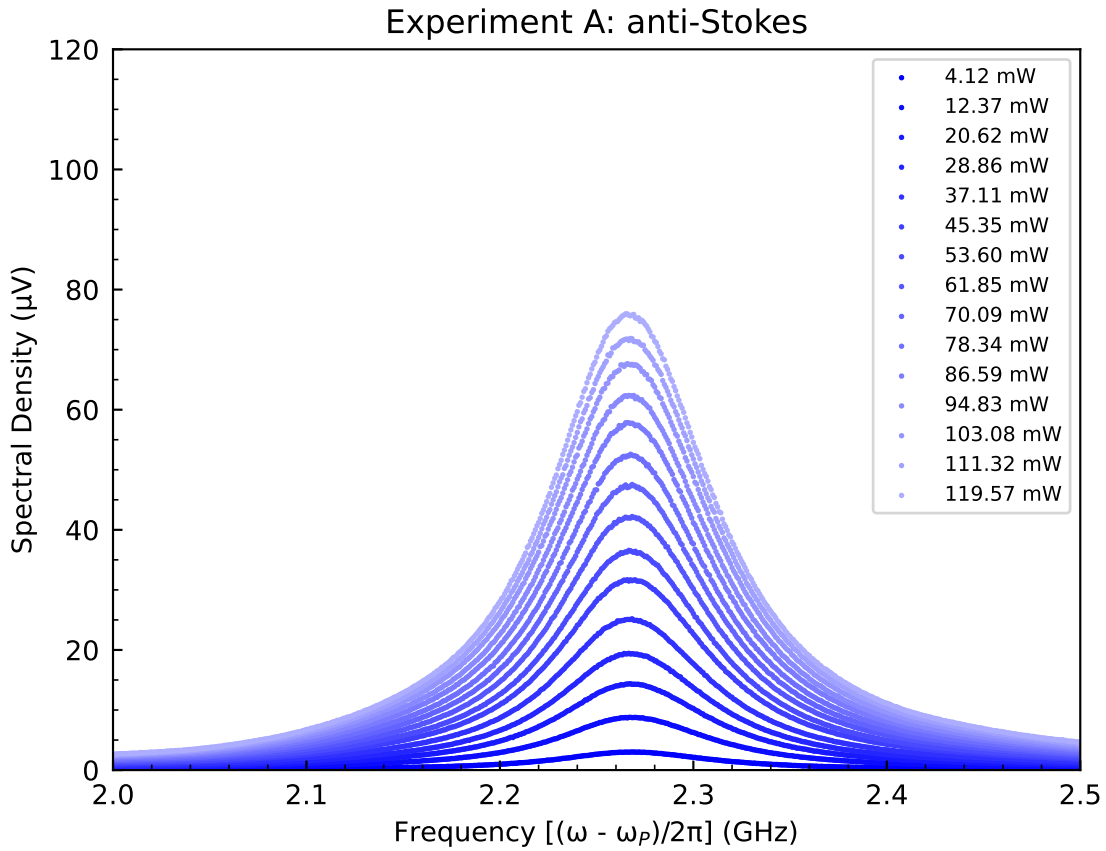


Figure 2.6: Anti-Stokes spectra for a range of pump powers obtained for Experiment A via spontaneous backwards Brillouin scattering. Intrafiber pump powers are displayed and were calculated from a measurement of 17% total through-fiber transmission and assuming equal losses through each of the two splices bookending the LCOF. To obtain each spectra, five repeated measurements of both the anti-Stokes spectra and the background (pump off) were collected for each pump power, with each measurement comprising an average over 100 250 ms sweeps at a RBW of 1 MHz. Plotted are the resulting background-subtracted spectra, with uncertainties smaller than the data point markers.

we find an effective Brillouin gain $G_B \approx (3.1 \pm 0.5) \text{ W}^{-1} \text{ m}^{-1}$. Using this gain factor, we find (right side of Equation 2.10) the temperature of the band of traveling wave phonons in the LCOF to reduced by $\Delta T \approx (25 \pm 2) \text{ K}$ from room temperature. Using instead the phonon occupancy method (left side of Equation 2.10) with the same respective linewidths, we find $\Delta T \approx (27 \pm 2) \text{ K}$, which agrees with the prior calculation and is independent of estimated Brillouin gain and intrafiber pump powers. All measured values and their associated uncertainties are tabulated for reproducibility in Tables A.1 and A.2 in Appendix A, Section A.3. The published article associated with this work reports a conservatively calculated Brillouin gain of $2.3 \text{ W}^{-1} \text{ m}^{-1}$, also obtained from measured linewidths and Equation 2.3. This discrepancy arises from slight differences in measured linewidths of the anti-Stokes spectra, which we attribute to variations among



Figure 2.7: Lorentzian-fitted peak amplitudes of the observed Stokes and anti-Stokes spectra. The dashed line showing a linear trend was obtained by applying a linear fit of all data points. The solid lines show the theoretical super- and sublinear scattered power for the Stokes and anti-Stokes processes, respectively, and were calculated using Equations A27 and A28 in Appendix A of Johnson et al. (2023)¹. Section A.3.1 provides a tabulation of the extracted fit parameters and their associated uncertainties for each of the Stokes and anti-Stokes spectra for all pump powers.

weighted fitting algorithms and resulting uncertainties. Using this reported value of $G_B \sim 2.3 \text{ W}^{-1} \text{ m}^{-1}$ for the Brillouin gain along with the right side of Equation 2.10 recovers the conservatively reported $\sim 21 \text{ K}$ of cooling.

Figure 2.9 plots a simulated Brillouin gain spectrum G_B ($\text{W}^{-1} \text{ m}^{-1}$), obtained from finite element simulations¹ of the optical and acoustic modes of the LCOF, overtop the 4.12 mW pump power (nearest to natural equilibrium) anti-Stokes spectrum. While the y-scaling between the two spectra is arbitrary, the lorentzian profile of the gain spectrum, and specifically the center frequency and natural-equilibrium linewidth, is predictive of scattered power expected from the LCOF across the frequency range. An uncertainty-weighted reduced χ^2 test for goodness of fit of the simulated gain spectrum to the observed anti-Stokes spectrum

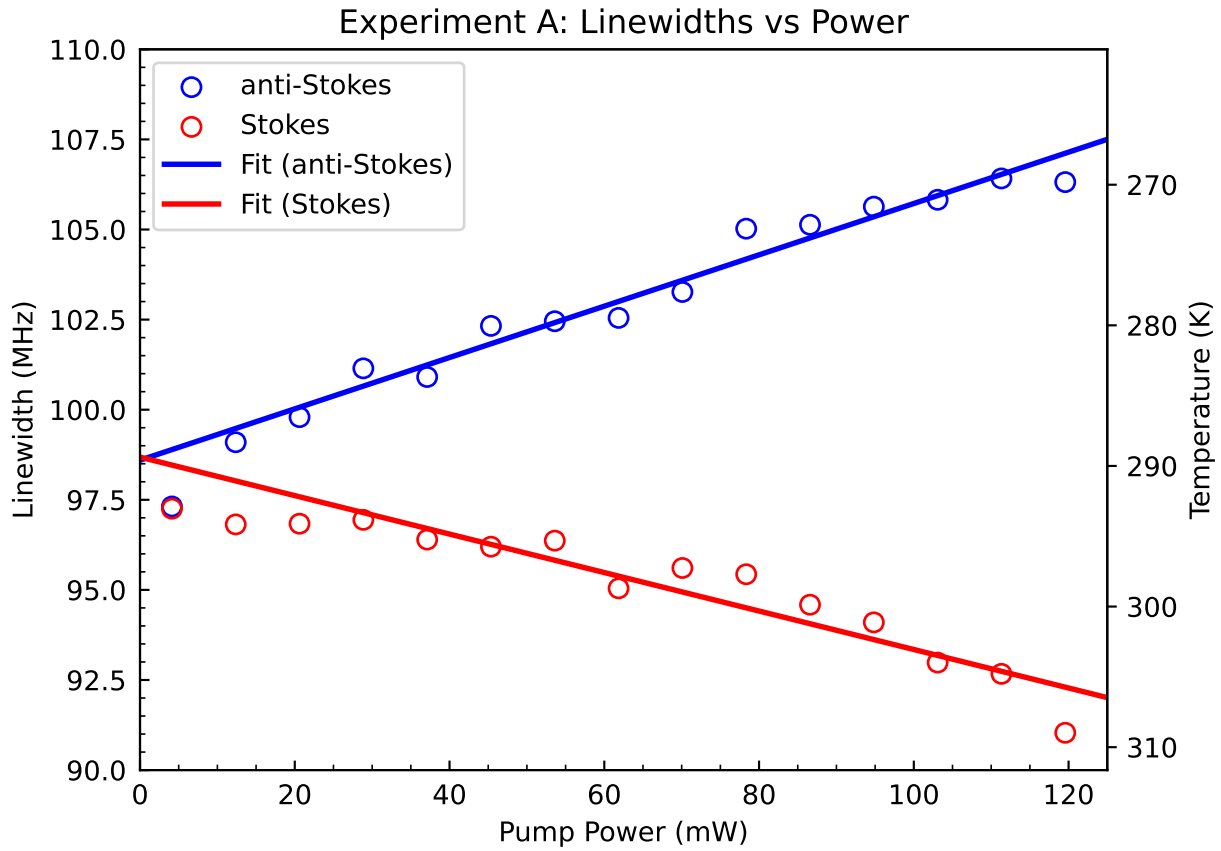


Figure 2.8: Stokes and anti-Stokes linewidths for each pump power, obtained from a lorentzian fit. Solid lines provide a linear fit to the respective Stokes and anti-Stokes measured linewidths. The secondary y-axis provides a temperature scale in degrees K, with room temperature (taken to be 293 K) centered at the equilibrium linewidth of the LCOF. Section A.3.1 provides a tabulation of the extracted fit parameters and their associated uncertainties for each of the Stokes and anti-Stokes spectra for all pump powers.

yields a value of 2.57. Reduced χ^2 values close to unity indicate a good fit.

2.4.2 Cooling Experiment B Results

Anti-Stokes scattered probe power was collected for four pump powers launched into the LCOF, providing intrafiber pump powers of 0.0 mW, 22.7 mW, 45.4 mW, and 68.0 mW. Figures 2.10, 2.11, 2.12, and 2.13 show these resulting spectra, respectively, along with associated weighted Lorentzian fit for each. The data plotted data has been binned within 10 MHz bins for clarity, with the Lorentzian fits and associated parameters having been derived from the unbinned data. Visual inspection confirms an excellent fit for each of the Lorentzian fits to their respective data, which have been plotted with error bars representing 1σ of the spectral density for each data point. All measured and calculated values are tabulated in Table A.3 in

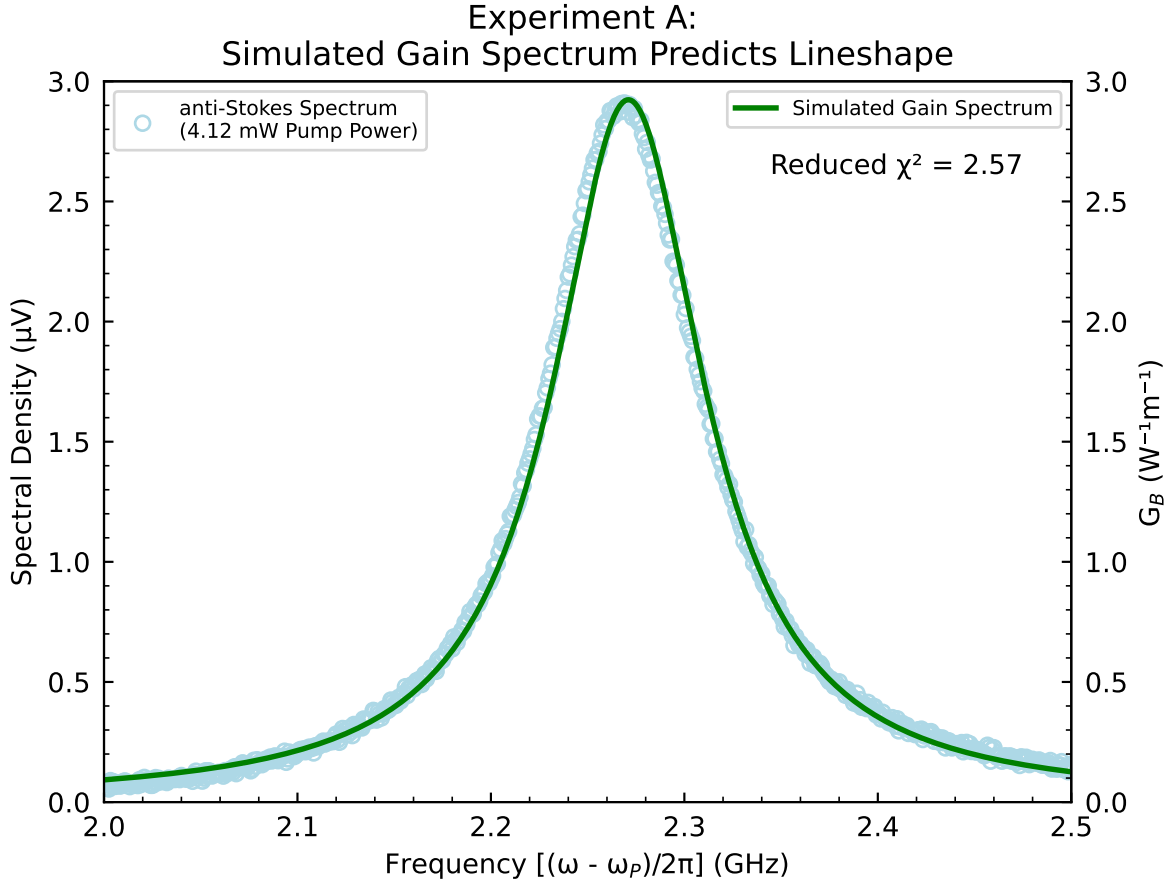


Figure 2.9: A simulated Brillouin gain spectrum G_B ($\text{W}^{-1} \text{m}^{-1}$), obtained from finite element simulations¹ of the optical and acoustic modes of the LCOF, overtop the lowest power (nearest to natural equilibrium) anti-Stokes spectrum (the 4.12 mW pump power spectrum). While the y-scaling between the two spectra is arbitrary, the lorentzian profile of the gain spectrum, and specifically the center frequency and natural-equilibrium linewidth, is predictive of scattered power expected from the LCOF across the frequency range. An uncertainty-weighted reduced χ^2 test for goodness of fit of the simulated gain spectrum to the observed anti-Stokes spectrum yields a value of 2.57. Reduced χ^2 values close to unity indicate a good fit.

Appendix A, Section A.3.2, including solved fit parameters and their associated uncertainties.

Figure 2.14 plots just the resulting fits for each spectra, showing a clear decrease in peak spectral amplitude with increasing pump power, consistent with the theory (see Equation B.50 in Appendix B.2, with constant power yet decreasing modal temperature). Figure 2.15 plots these peak spectral heights, derived from the fits, with their associated 1σ uncertainties. A linear fit has been applied, showing good correlation with the decreasing trend in peak spectral densities with increased pump power (cooling) corresponding to a lowering of the temperature of the anti-Stokes phonon mode. Figure 2.16 plots the spectral linewidths derived from the fits presented in Figure 2.14, with their associated 1σ uncertainties. A linear fit has been applied, showing fair correlation given the 1σ uncertainties displayed. The linear increase in spectral linewidths with

Experiment B: anti-Stokes Power Spectrum $P_P = 0.0 \text{ mW}$

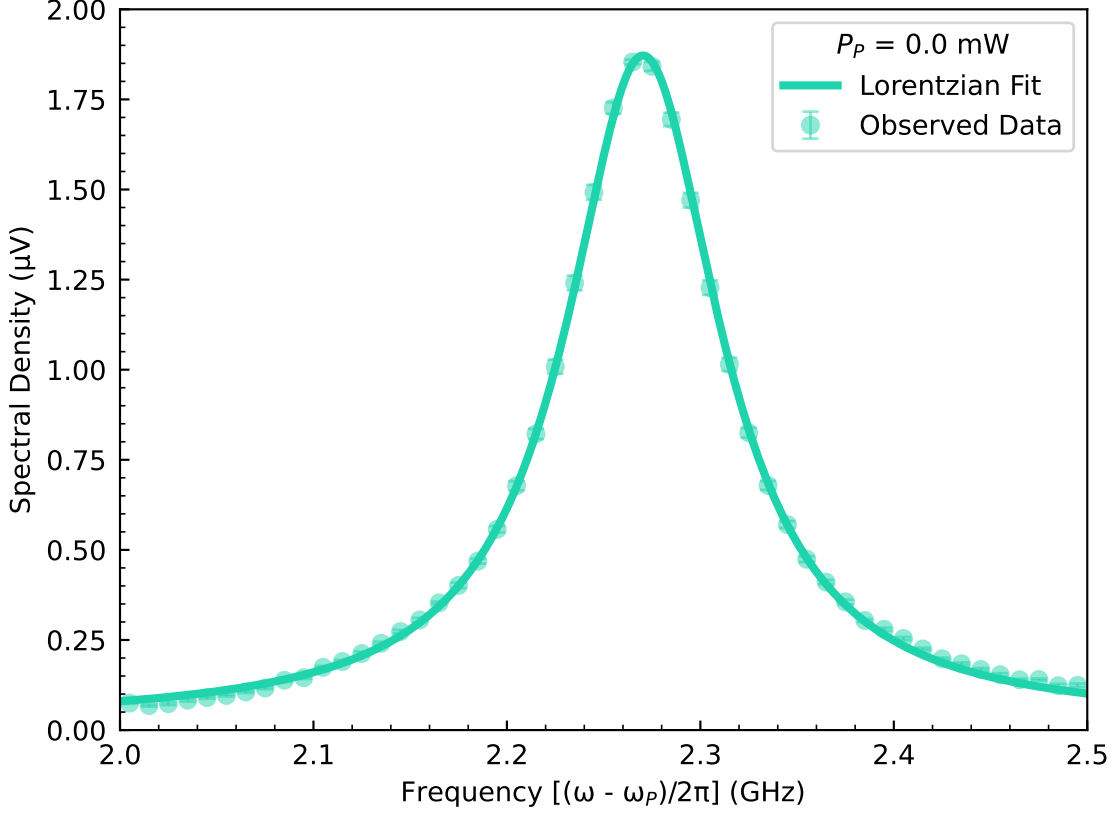


Figure 2.10: Anti-Stokes probe spectra collected for 0.0 mW intrafiber pump power in Experiment B. Data is binned within 10 MHz bins and displayed with error bars representing 1σ of spectral density. A Lorentzian fit has been computed based on the unbinned data and visual inspection confirms an excellent fit to the observed spectra. In conducting the experiment, five repeated measurements of both the anti-Stokes spectra and the background (pump off) were collected for each pump power, with each measurement comprising an average over 100 250 ms sweeps at a RBW of 1 MHz. The spectral data shown here are the resulting background-subtracted spectra, with uncertainties propagated accordingly.

increasing pump power (cooling) indicates, as with Experiment A, an increased dissipation rate due to laser cooling of the anti-Stokes phonon mode.

We can apply the same quantitative analysis for the data gathered in Experiment B as was performed for Experiment A. Using the 0.0 mW and 68.0 mW pump power spectral linewidths for the equilibrium and maximally cooled dissipation rate, respectively, in Equation 2.3, we find a Brillouin gain of $G_B \approx (8 \pm 2) \text{ W}^{-1} \text{ m}^{-1}$, taking the 2σ confidence interval in linewidths and allowing a 10% uncertainty in pump power within the LCOF. Applying this gain factor to the right side of Equation 2.10, we find the traveling-wave phonons in the anti-Stokes mode of the LCOF to have been cooled by $\Delta T \approx (35 \pm 2) \text{ K}$. Using the quantized thermal dissipation rate method to calculate degrees cooled (left side of Equation 2.10), we find

Experiment B: anti-Stokes Power Spectrum
 $P_P = 22.7 \text{ mW}$

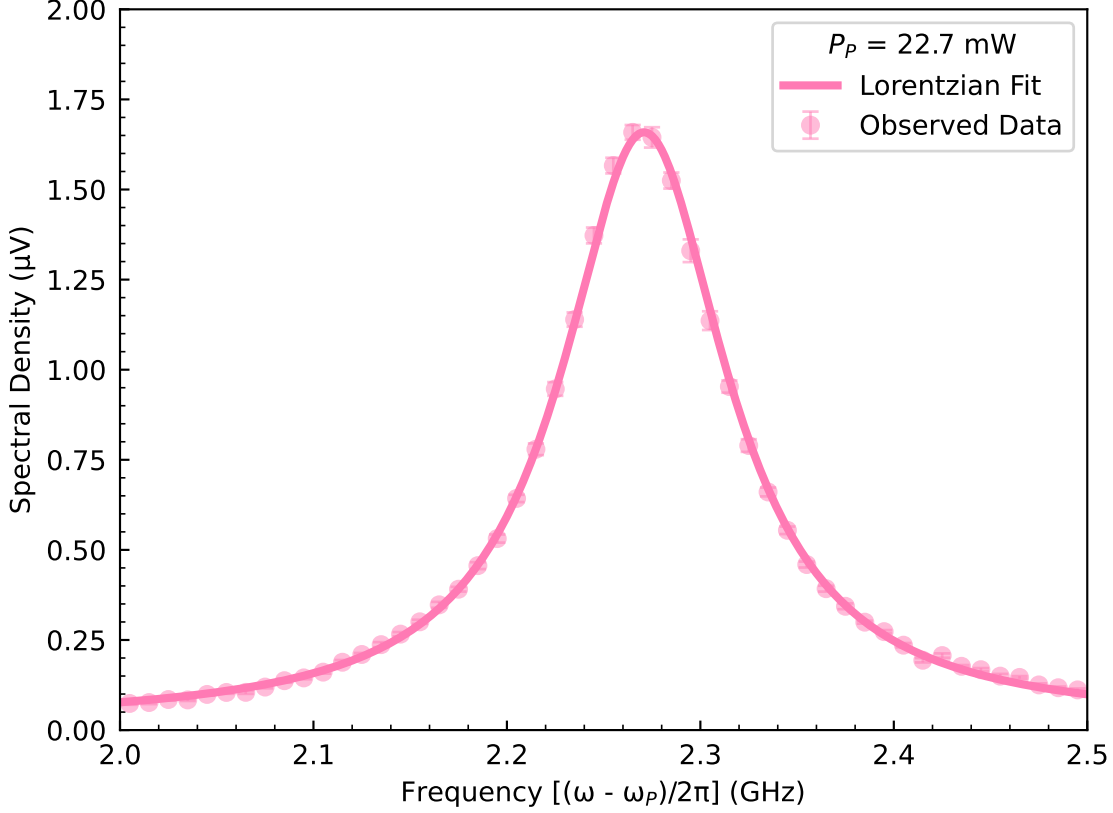


Figure 2.11: Anti-Stokes probe spectra collected for 22.7 mW intrafiber pump power in Experiment B. Data is binned within 10 MHz bins and displayed with error bars representing 1σ of spectral density. A Lorentzian fit has been computed based on the unbinned data and visual inspection confirms an excellent fit to the observed spectra. In conducting the experiment, five repeated measurements of both the anti-Stokes spectra and the background (pump off) were collected for each pump power, with each measurement comprising an average over 100 250 ms sweeps at a RBW of 1 MHz. The spectral data shown here are the resulting background-subtracted spectra, with uncertainties propagated accordingly.

$\Delta T \approx (36 \pm 2) \text{ K}$ of cooling, which is in agreement with the prior calculated value using the Brillouin gain approach. The discrepancy among Brillouin gain factors for the LCOF calculated from Experiment A and Experiment B is not expected and is explored in the next section. This Brillouin gain factor is a consequence of both the linewidths and the corresponding pump powers inside the LCOF, seen visually as the slopes of Figure 2.8 for Experiment A and Figure 2.16 for Experiment B.

Experiment B: anti-Stokes Power Spectrum
 $P_P = 45.4 \text{ mW}$

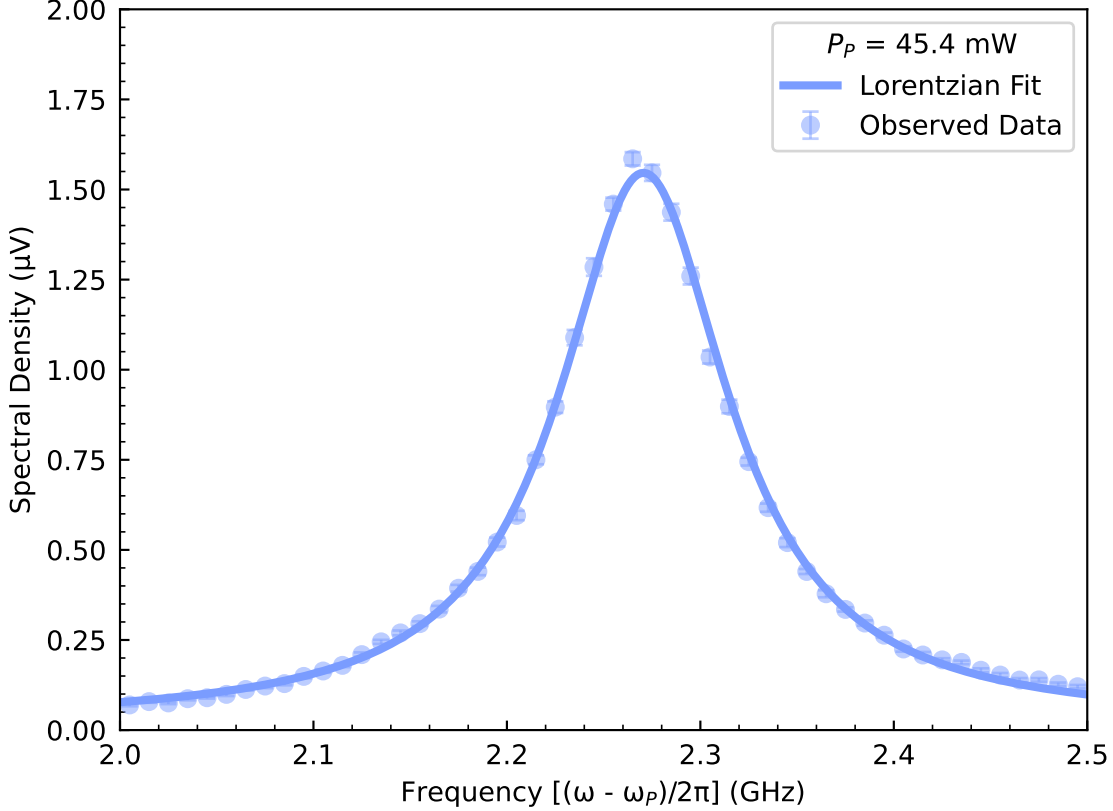


Figure 2.12: Anti-Stokes probe spectra collected for 45.4 mW intrafiber pump power in Experiment B. Data is binned within 10 MHz bins and displayed with error bars representing 1σ of spectral density. A Lorentzian fit has been computed based on the unbinned data and visual inspection confirms an excellent fit to the observed spectra. In conducting the experiment, five repeated measurements of both the anti-Stokes spectra and the background (pump off) were collected for each pump power, with each measurement comprising an average over 100 250 ms sweeps at a RBW of 1 MHz. The spectral data shown here are the resulting background-subtracted spectra, with uncertainties propagated accordingly.

2.4.3 Evidence of Transmission Degradation

After comparing the anti-Stokes linewidths measured in Experiments A and B, we conclude that significant splice transmission degradation occurred in the interim. Experiment B was performed first (with a through-fiber transmission of 17%), followed by Experiment A the next day. If the experimental conditions were unchanged between the two experiments, the slopes of the anti-Stokes linewidth versus pump power would be identical (Figures 2.8 and 2.16). Instead, Experiment B exhibits a noticeably steeper slope than Experiment A. A reanalysis shows that reducing the assumed transmission for Experiment A so the two slopes match would require the total fiber transmission to have dropped from 17% down to approximately

Experiment B: anti-Stokes Power Spectrum $P_P = 68.0$ mW

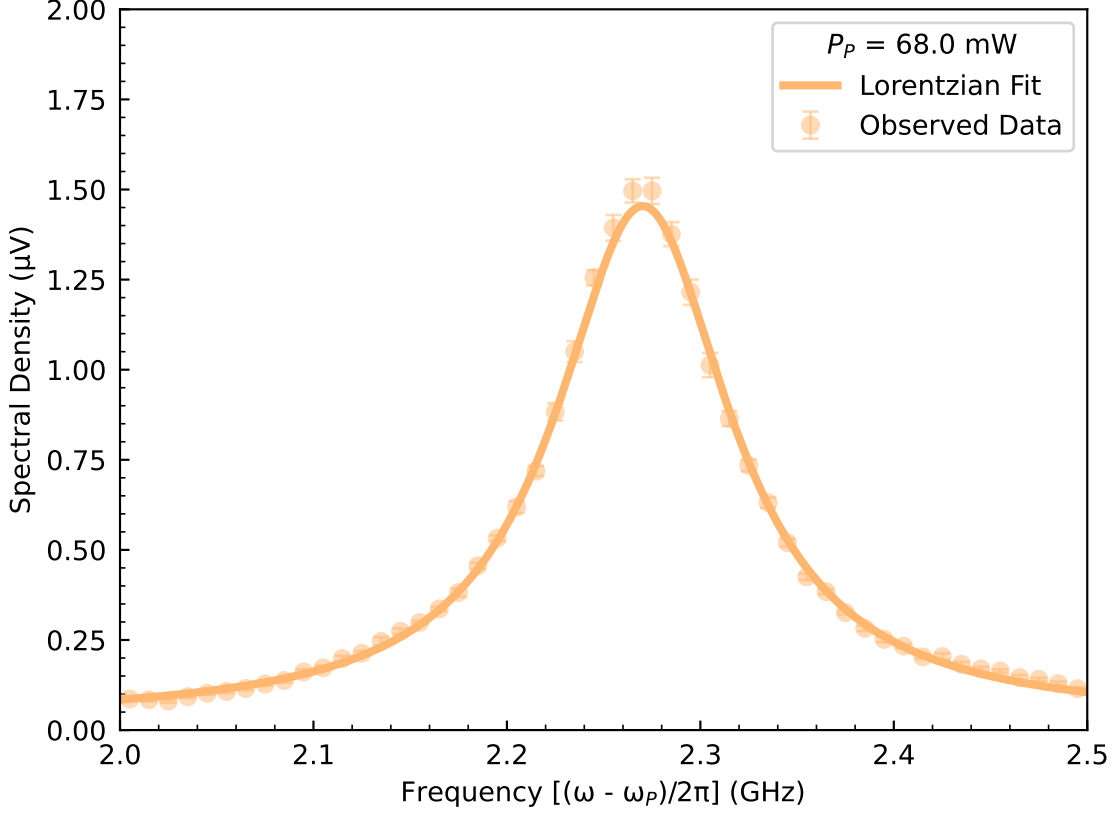


Figure 2.13: Anti-Stokes probe spectra collected for 68.0 mW intrafiber pump power in Experiment B. Data is binned within 10 MHz bins and displayed with error bars representing 1σ of spectral density. A Lorentzian fit has been computed based on the unbinned data and visual inspection confirms an excellent fit to the observed spectra. In conducting the experiment, five repeated measurements of both the anti-Stokes spectra and the background (pump off) were collected for each pump power, with each measurement comprising an average over 100 250 ms sweeps at a RBW of 1 MHz. The spectral data shown here are the resulting background-subtracted spectra, with uncertainties propagated accordingly.

3%. While large, degradation of this level is plausible and is supported by several further points of analysis.

First, the optical performance of the splices bookending the LCOF, already very delicate and susceptible to damage from nominal handling, are vulnerable to any particulates becoming lodged between the cores of the UHNA7 and LCOF. While epoxy is among the more chemically resistant adhesives, any particulate contamination adhered to the surface of the epoxy or reservoir walls introduced from the environment during fabrication could easily become dislodged and settle into the splice opening. Some chemical dissolution of the epoxy within the reservoir by the CS_2 after the prolonged soaking period (24 h) is also possible. Additionally, any unfortunate mechanical stress incurred during normal handling of the LCOF is liable to cause damage and incur significant optical loss through one of the splices. Optical losses of this rate and



Figure 2.14: Computed Lorentzian fits from the observed anti-Stokes probe spectra gathered for Experiment B, shown in Figures 2.10, 2.11, 2.12, and 2.13, with consistent coloring across plots corresponding to intrafiber pump power. Fits are identical to those displayed with their respective observed spectra, with the fit parameters computed from the unbinned spectra for each intrafiber pump power. The decreasing trend in peak spectral density (proportional to phonon population) with increasing pump power (cooling) provides direct evidence of laser cooling of a band of traveling wave phonons within the LCOF.

magnitude, while not common, have been observed in several prior LCOF samples.

Standard experimental procedure would catch this degradation in performance, however for this particular LCOF sample, the exit fiber immediately following the end splice broke off irreparably after testing its transmission, making it no longer possible to remeasure the full through-fiber transmission during Experiment A. In other words, if transmission had declined between experiments, we had no direct means of detecting it. Additionally, as seen in Figures 2.3 and 2.4, the pump power was recorded prior to launch into the LCOF for both experiments, providing no indication of change in performance of the splice between experiments. Hence, applying the same optical loss estimate to a splice that had experienced transmission degradation in the interim would have resulted in an overestimation of the actual power inside the LCOF

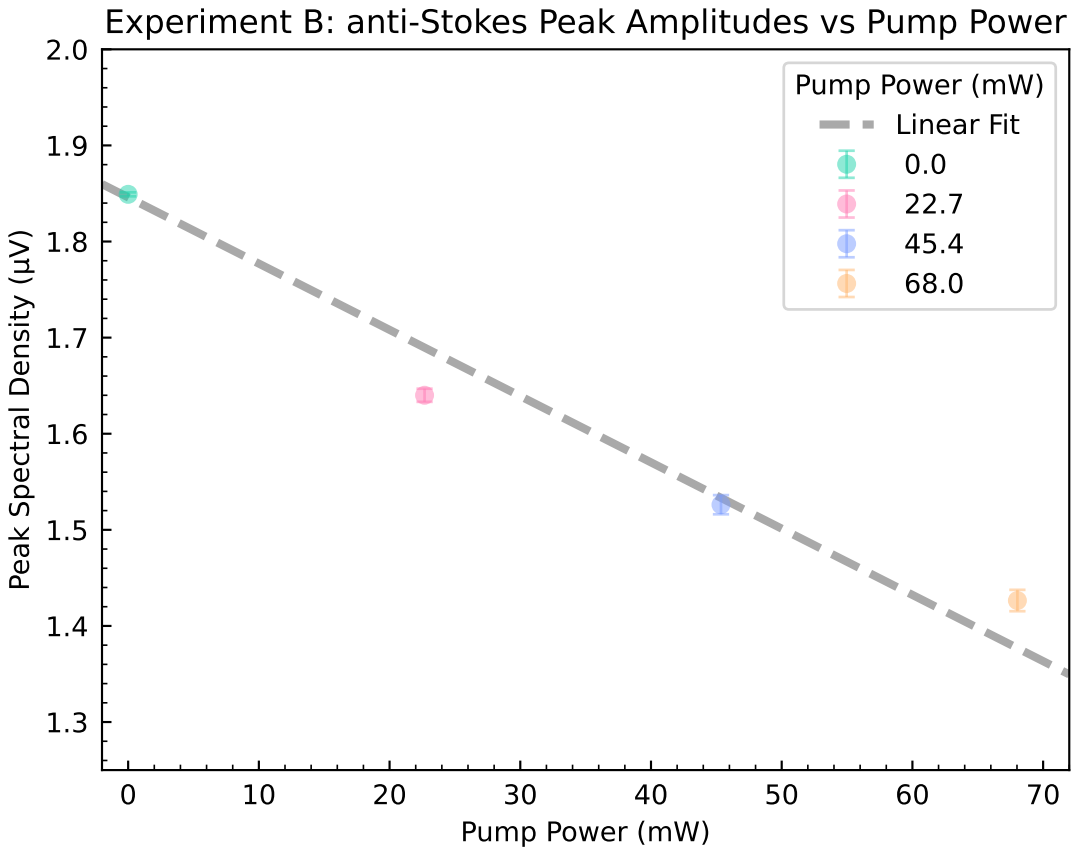


Figure 2.15: Plot of peak spectral density amplitudes for the anti-Stokes spectra gathered for Experiment B, corresponding to the four intrafiber pump powers used for the experiment. Values have been extracted from solved fit parameters for the Lorentzian fits displayed in Figure 2.14, as well as individually with their respective observed spectra (Figures 2.10, 2.11, 2.12, and 2.13). A linear fit has been applied to the data, showing a fair correlation to the data given the 1σ uncertainty representation for peak spectral density. The peak spectral amplitude is expected to decrease linearly with decreasing temperature of the mechanical mode due to anti-Stokes Brillouin cooling, consistent with Equation B.50 for scattered power of the spontaneous Brillouin scattering process.

during Experiment A (conducted after Experiment B).

Further quantitative analysis supports this hypothesis as well. As we reported in Johnson et al. (2023)¹, Experiment A yields a Brillouin gain of approximately $2.3 \text{ W}^{-1} \text{ m}^{-1}$, calculated using Equation 2.3. This value is smaller than the $(6 \pm 1) \text{ W}^{-1} \text{ m}^{-1}$ reported by Behunin et al. in 2019²¹ for a near-identical LCOF geometry and fabrication method. If instead we calculate the Brillouin gain based on the linewidths and corresponding intrafiber pump powers seen in the earlier Experiment B, we find the Brillouin gain to be approximately $(8 \pm 2) \text{ W}^{-1} \text{ m}^{-1}$, which is in good agreement with the prior published value from the literature. In estimating the uncertainty here, we have taken the 2σ confidence level in linewidths and allowed a 10%

Experiment B: anti-Stokes Linewidths vs Pump Power

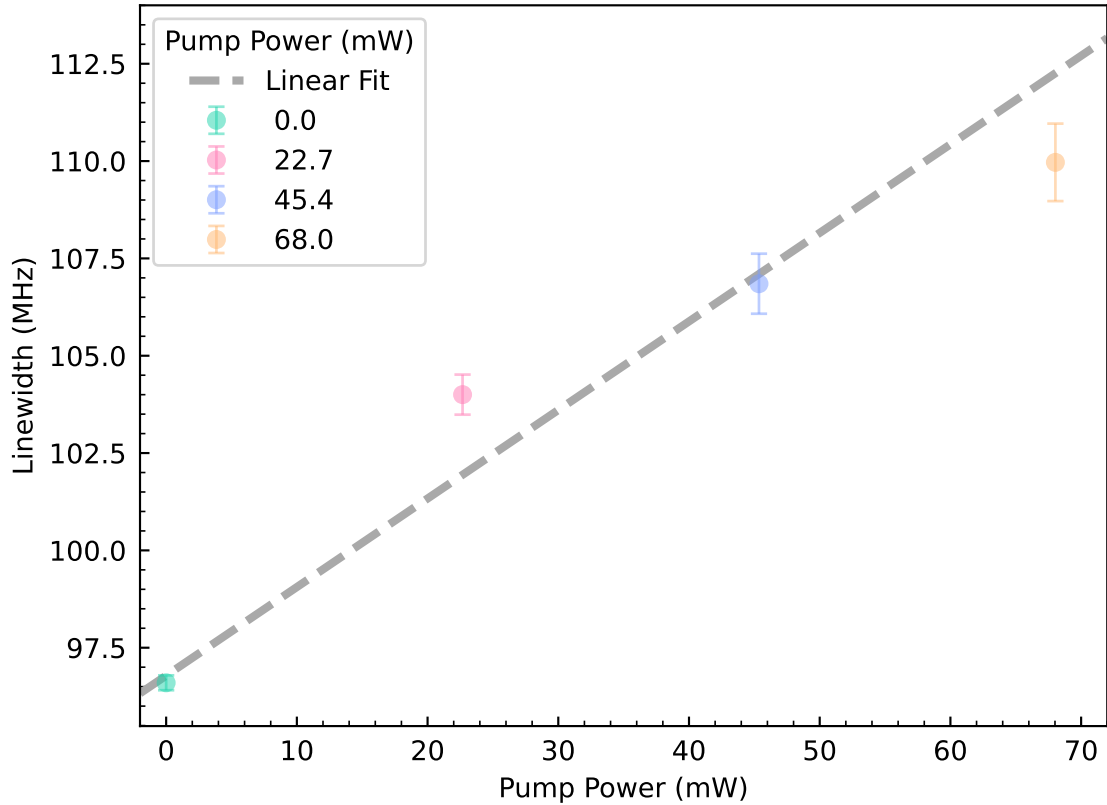


Figure 2.16: Plot of the full-width half-max (FWHM) linewidths of the anti-Stokes spectra gathered for Experiment B, corresponding to the four intrafiber pump powers used for the experiment. Values have been extracted from solved fit parameters for the Lorentzian fits displayed in Figure 2.14, as well as individually with their respective observed spectra (Figures 2.10, 2.11, 2.12, and 2.13). A linear fit has been applied to the data, showing a fair correlation to the data, given the 1σ uncertainty representation for peak spectral density. Effective anti-Stokes linewidths are expected to increase linearly with increased pump power (cooling) according to Equation 2.3, absent pump depletion or any saturation effects. Discrepancies with a linear trend among the data presented with their associated vertical uncertainties are likely due to an underestimation of uncertainty in intrafiber pump power, which would be represented by some horizontal uncertainty associated with each data point. In the possible event of thermal saturation effects in the LCOF, or unlikely pump depletion, we would expect to see linewidths exhibit a sublinear trend above a critical threshold of intrafiber pump power. While it is possible some minor saturation occurred at these powers, a more conservative accounting of uncertainties in both linewidths and intrafiber pump powers is sufficient to explain a linear trend.

uncertainty in intracore pump powers. The natural conclusion is that for Experiment A we overestimated the intrafiber pump power due to the undetected splice transmission degradation between experiments. This produced an apparent smaller dependence of linewidth on pump power in Experiment A and a consequent underestimation of the true gain of the LCOF.

Finally, the linewidths of Experiment B appear to exhibit a slight sublinear trend with power (Figure 2.16), indicating the possibility of a saturation effect occurring at higher pump power. However any saturation effect or similar which could cause this trend should then also be activated at the higher pump powers used in Experiment A, if the optical transmission were the same across experiments. If instead the transmission of the LCOF entrance splice had been significantly greater for the earlier-run Experiment B than for Experiment A, the powers inside the LCOF in Experiment B could have been similar to or even greater than those in Experiment A. This might explain why Experiment B linewidths appear to exhibit slightly sublinear growth with pump power despite the lower pump powers launched into the LCOF while Experiment A does not seem to exhibit this same trend, despite the use of higher nominal pump powers. This is consistent with an estimated factor of 5 drop in transmission through the LCOF splice between experiments, as indicated by the discrepancy in linewidth vs power slopes of each experiment.

In summary, all these lines of evidence strongly indicate that the LCOF splice transmission fell substantially in the time between Experiments B and A, by an approximate factor of five. This fully reconciles the differing slopes in the anti-Stokes linewidth data and explains the otherwise surprising discrepancy in inferred Brillouin gain compared to values published in the literature for identical CS_2 -filled LCOFs. This conclusion implies even higher performance of our LCOF example than was previously understood and reported in Johnson et al. (2023)¹: the amount of cooling achieved (unaffected by this reanalysis) was accomplished with far less pump power.

2.5 Discussion

2.5.1 The *C*-Value: A Standardized Cooling Metric

Cooling results are often reported in degrees kelvin cooled, sometimes only implicitly stated from room temperature. While this is understood by researchers closely following laser cooling, it can be misleading to those who are looking to apply these published techniques to systems not starting at room temperature. A lack of clarity of cooling performance as being a function of starting temperature may cause buyer's remorse among researchers who expend resources to employ the technique only to realize less than advertised absolute degrees cooling of a material below room temperature. Even for the more careful researcher this introduces frustration in the literature review process. To address this, we propose a normalized cooling metric be adopted to report the fractional degrees cooled relative to initial temperature. We introduce the *Cooling metric (*C*)*, or *C-value*, expressed as a percentage of degrees cooled from initial temperature,

$$C = \frac{\Delta T}{T_0}. \quad (2.11)$$

Reporting the C -value of a cooling technique offers greater transparency, clarity, and universal applicability of performance across cooling techniques and application fields. Recent discussions in the optical refrigeration community have similarly called for standardized cooling metrics to ensure fair, reproducible comparisons of cooling results.²² Indeed, reporting only absolute degrees cooled may significantly *underrepresent* the performance of a given technique if applied to a material above room temperature (as is often the case for data center and information processing applications). Adopting the C -value for cooling performance will expand the perceived viability and utility of laser cooling techniques to researchers outside of optomechanical physics and related fields, potentially spurring greater investment interest in the advancement of laser cooling techniques. As such, we report a C -value of 12%, achieved with 68.0 mW of intrafiber pump power (Experiment B).

By contrast, the recent result by Martinez et al. (Max Planck Institute, 2024)²³ demonstrated a much larger $\Delta T \approx 219\text{K}$ cooling from room temperature, an unprecedented C -value of 73% cooling of the phonon mode's temperature. This emphasizes the Max Planck group's achievement of removing nearly three-quarters of the thermal energy from that acoustic mode, a level on par with the best solid-state optical cryocoolers, which have reached $\sim 91\text{ K}$ from ambient ($\sim 70\%$ cooling) in Yb-doped crystals.²² The fractional metric thus allows us to compare techniques across disparate systems such as optical fibers and bulk crystals on equal footing for their cooling effectiveness. As approaches push toward lower starting temperatures (e.g. pre-cooled or cryogenic environments), absolute ΔT naturally shrinks, but a high C -value will remain notable. Adopting the C -value, in combination with a commitment to publishing sufficiently rigorous experimental context,²² yields a transparent gauge of performance across diverse temperature regimes and material platforms.

2.5.2 Parallel Achievement: Max Planck Institute

The principles demonstrated in this chapter can be directly compared to parallel work by other groups using different fiber platforms. In particular, Martinez et al. (2024)²³ reported optoacoustic cooling of traveling phonons in a tapered chalcogenide photonic crystal fiber (PCF). In their experiment, a 50 cm long PCF with a microstructured, tapered core was used to enhance optomechanical coupling. Like our system, the Max Planck group employed Brillouin backscattering in a continuous waveguide to achieve phonon cooling of traveling-wave phonons. The underlying mechanism is the same: anti-Stokes scattering removes

thermal phonons by converting them into higher-energy photons that promptly leave the system. Both platforms therefore rely on traveling-wave Brillouin interactions and leverage the fast escape of anti-Stokes light compared to phonon thermalization times to cool a band of acoustic modes.

Despite these similarities in principle, there are important differences in the experimental implementation. The PCF platform uses a solid chalcogenide fiber with a patterned microstructure, which was tapered to a small core diameter. The combined material and geometric parameters yield an acoustic mode at 7.38 GHz (higher than the 2.27 GHz acoustic band in our liquid-core fiber) and a very large effective Brillouin gain coefficient $G_B \sim 180 \text{ W}^{-1} \text{ m}^{-1}$. The higher acoustic frequency in the PCF means each phonon carries more energy ($\hbar\Omega_B/k_B \approx 0.35 \text{ K}$ vs 0.1 K for our system), but also that the mean thermal occupation at room temperature is lower (on the order of 10^2 vs. a 10^3 in our lower frequency mode). The two experiments also operated at different pump power: our work used a modest 68.0 mW of laser power to achieve 35 K of cooling (Experiment B), whereas the PCF results employed a maximum pump power of nearly 250 mW to achieve the reported 219 K cooling from room temperature, or a C -value of 74.7%.²³

2.5.3 Pathways to Net Cooling

While the experiments to date (including this work and Martinez et al.) achieve cooling of a phonon mode relative to the ambient lattice temperature, the phonon population of the overall system remains uncooled due to the inverse process (Stokes) simultaneously depositing energy into the Stokes phonon mode. Net cooling would imply extracting heat faster than it is replenished by both thermalization (the natural dissipation rate of the system) *and* Stokes scattering of the Stokes phonon mode. Engineering a system to reach this regime is a challenge, but we envision several pathways that could tip the balance toward net cooling.

One strategy is to bias the gain in favor of anti-Stokes scattering within a single transit of the medium, by suppressing or preventing Stokes processes through waveguide design. In a standard fiber, any pump photon has some probability to scatter into a Stokes photon, creating a phonon, which counteracts cooling. If we can reduce the likelihood of Stokes scattering while allowing anti-Stokes scattering to proceed, the net effect in one pass will be phonon removal without equivalent phonon creation. For example, one could design a fiber or waveguide that does not efficiently guide the Stokes-shifted wavelength, similar to a photonic bandgap fiber that places the Stokes frequency in a bandgap. In such a fiber, a pump photon could still undergo anti-Stokes scattering, but a would-be Stokes photon falls outside the guided modes and is effectively not generated.

Another approach is to incorporate an out-of-plane coupling mechanism to an absorbing medium or a frequency cutoff for only the Stokes. By asymmetrically enhancing loss for Stokes, one can bias the single-

pass Brillouin interaction toward net phonon annihilation. By diverting the Stokes field away from the guided mode through an engineered out-of-plane coupling, we can effectively “dump” the Stokes into a loss channel while preserving the anti-Stokes within the waveguide core, thus favoring net phonon removal. For instance, one might introduce a side-etched structure or grating that phase-matches only to the Stokes frequency, routing Stokes photons into an absorbing or radiative mode. Meanwhile, the anti-Stokes remains confined to the original waveguide, continuing to interact with the target phonon mode. Such a design ensures that Stokes photons, once generated, are immediately evacuated before they can drive the reverse (phonon creation) process. When combined with sufficiently strong anti-Stokes gain, this asymmetric loss channel could break the symmetry of phonon creation and annihilation within a single transit, thereby accelerating phonon cooling. Although this approach demands precise control over waveguide geometry and materials to selectively scatter and absorb Stokes without degrading anti-Stokes propagation, it holds promise for realizing net cooling in practical fiber architectures.

Another promising avenue for enhancing net phonon cooling in continuous Brillouin systems is the deliberate engineering of a group-velocity bias between the Stokes and anti-Stokes waves. By differentiating their propagation speeds, one introduces a temporal asymmetry in interaction strength that preferentially enables phonon annihilation over phonon creation. Some works explore this idea via enhancement of the optical density-of-states at the anti-Stokes frequency via slow-light or resonance effects while reducing it at the Stokes frequency.^{13,24} Crucially, however, any group velocity bias strategy must be designed with the phonon lifetime and effective system length in mind, as effective cooling demands that anti-Stokes photons carry away energy faster than the phonon mode thermally repopulates.

2.5.4 Applications to Ground State Cooling

Reaching lower phonon occupancies and ultimately approaching the quantum ground state of a traveling acoustic wave mode is not only a scientific milestone but also an enabling step for quantum applications. Cooling traveling-wave phonons toward the ground state means drastically reducing their thermal noise, to the point that quantum mechanical effects of the phonons emerge. In the quantum regime, a traveling acoustic phonon mode in an optical fiber can serve as a memory or intermediary for quantum states of light. Photons can be coherently converted to phonons and back, effectively storing the photonic state in a mechanical degree of freedom. Coupling light to acoustic phonons has already been used to demonstrate all-optical signal storage and delay in classical contexts. For example, light pulses can be fully converted into acoustic waves and retrieved after a storage interval.²⁵ If those acoustic waves are in a near-ground-state (low-noise) condition, one could perform the same feat at the single-photon level, realizing a broadband quantum

memory at telecom wavelengths. Such a memory would be reversible and coherent, capable of storing quantum information (amplitude and phase of a single-photon wavepacket) for microsecond durations.²⁵ Moreover, a low-phonon-temperature waveguide could function as a quantum optical delay line or buffer with minimal added noise, preserving quantum states during the delay.

If the traveling acoustic mode approaches its ground state, one can begin to prepare and manipulate non-classical phonon states. This could include generating single phonons on demand, phonon Fock states, or entangled states between phonons and photons. One exciting prospect is creating entangled states between a traveling phonon and a propagating photon. The cooled phonon mode would have low enough noise to allow high-fidelity entanglement generation via stimulated scattering processes. In fact, a recent proposal by Zhu et al. (2024) suggests that even without ground-state preparation, one can generate entangled photon–phonon pairs in a fiber using pulsed Brillouin processes.²⁶ Their scheme relies on a two-pump configuration to create correlated Stokes and anti-Stokes photons along with a phonon, and remarkably it does not require the phonon to start in the ground state. If the phonon mode were already near its ground state, one can imagine the entanglement rates and purity could be even higher. Beyond two-party entanglement, could facilitate multi-mode quantum state engineering, for example, creating squeezed phonon states.²⁷ The ability to manipulate a continuum of phonon modes at the quantum level might also enable quantum acoustic signal processing, where information is encoded in phononic wavepackets and processed (filtered, delayed, interfered) with quantum coherence.²⁸

Achieving ground-state cooling of a macroscopic, traveling-wave phonon mode will likely require a hybrid approach: combining conventional cryogenics with our laser cooling techniques. Cavity optomechanics experiments regularly precool the device to liquid helium temperatures before applying laser cooling to reach the quantum ground state²⁹, and the same idea applies to continuous systems. Placing the optical fiber or waveguide in a cryostat lowers the baseline phonon occupancy, dramatically reducing the gap to the ground state. Laser cooling could then be applied to overcome the remaining thermal quanta.

2.5.5 Conclusion

In conclusion, the work presented in this chapter establishes a robust foundation for fiber-based optomechanical cooling of traveling-wave phonons, pushing the boundaries of what can be achieved in continuous-wave Brillouin systems. By demonstrating Brillouin anti-Stokes cooling in a carefully engineered LCOF platform, we have shown that laser cooling need not be relegated to highly specialized chip waveguides or microresonators. The advantageous optomechanical properties of the LCOF enabled clear evidence of laser cooling under ambient conditions and marks the first demonstration of its kind in a fiber format. This proof of prin-

ciple opens up numerous opportunities for fiber-based applications, including precision metrology, low-noise acousto-optic devices, and quantum information schemes requiring mechanically cooled states. By demonstrating the capacity to cool traveling-wave phonons in an optical fiber, this work lays the groundwork for future low-noise photonic devices and advanced acousto-optic technologies, marking a significant step toward quantum-limited acoustic control.

Chapter 3

A Coherently Stimulated Phonon Spectrometer

This chapter presents a preview of an article in-prep for publication. Neither the author nor the publisher are responsible for any errors or omissions in any future publication derived from this version of the manuscript.

3.1 Abstract

We present a novel coherently stimulated Brillouin spectrometer utilizing a detuned pump-probe design that exploits a relaxation of phase-matching requirements at small lengths, enabling room-temperature traveling-wave phonon spectroscopy at the micrometer scale with sub-10 fW sensitivity. This approach overcomes the limitations of traditional stimulated Brillouin techniques, particularly regarding phase-matching constraints and spatial resolution. We validated our instrument's sensitivity with 1 cm of Ultra High Numerical Aperture 3 (UHNA3) fiber and 100 μm of bulk carbon disulfide liquid, demonstrating its capability to measure Brillouin scattering in materials with low Brillouin gain or, with particular advantage, small effective lengths. This advancement opens new possibilities for nanometer-scale Brillouin spectroscopy and the development of nano-acousto-optic devices.

3.2 Introduction

Brillouin scattering, the inelastic interaction between light and acoustic phonons, is a fundamental phenomenon for probing the mechanical and structural properties of materials at microscopic scales. In spontaneous Brillouin scattering, thermally excited acoustic phonons scatter incident light, causing frequency shifts that reveal information about the material's elastic properties and acoustic modes³. However, the weak signal inherent to spontaneous Brillouin scattering often demands long acquisition times and limits spatial resolution, posing challenges for high-resolution material characterization.

Stimulated Brillouin Scattering (SBS) uses intense optical fields to amplify the acoustic wave through a

nonlinear optical process³⁰. In SBS, a strong pump laser interacts with a counter-propagating Stokes wave in the medium, generating acoustic phonons via electrostriction. As the phonon population grows, it further amplifies the Stokes wave. In turn, that amplified Stokes wave interferes with the pump and reinforces the acoustic field, creating a positive feedback loop that drives exponential amplification. This mechanism enables more efficient excitation and detection of acoustic phonons and underpins numerous applications in optical signal processing, sensing, and high-resolution spectroscopy including mechanobiology^{31–40}.

However, conventional SBS techniques struggle with short samples or materials of inherently low Brillouin gain and strict phase matching requirements continue to pose a challenge.^{41–43}. Because the Stokes amplitude depends on the product of the Brillouin gain coefficient, pump power, and interaction length, small volumes often yield weak signals unless extremely high optical powers are used. Moreover, while backward SBS sends the scattered wave in the opposite direction of the pump, parasitic reflections and pump leakage can still obscure the Stokes signal, demanding careful optical isolation and sometimes elaborate filtering. These constraints make it difficult to measure thin films and micro- and nanoscale devices, particularly if high optical intensities risk damaging sensitive samples. As a result, standard SBS approaches are not easily adapted to sub-centimeter lengths or low-gain media, prompting the need for new methods that maintain high sensitivity in short interaction regions.

To overcome these challenges, researchers have explored various approaches^{44–49}. Techniques based on optical cavities increase the effective interaction length, but require precise alignment and are sensitive to environmental fluctuations⁵⁰. Forward Brillouin scattering methods, such as those demonstrated by Kittlaus et al.⁵¹, offer relaxed phase-matching conditions but introduce increased modal complexity. Meanwhile, coherent probe beam amplification can boost sensitivity, yet it can introduce additional noise and complexity because phase noise in laser sources can cause significant gain fluctuations⁵².

Here, we demonstrate a detuned pump-probe design that relaxes the usual phase-matching constraints at short lengths. This approach offers a new route to measure traveling-wave phonons in sub-centimeter or even micrometer-scale samples at room temperature with unprecedented sensitivity. We demonstrate the capabilities of the instrument by measuring Brillouin scattering in 1 cm of UHNA3 fiber and 100 μm of bulk carbon disulfide (CS₂) liquid. These measurements highlight the instrument's ability to characterize materials with low Brillouin gain or small effective lengths.

The development of this coherently stimulated Brillouin spectrometer opens new avenues for nanometer-scale Brillouin spectroscopy and advances the characterization and design of nano-acousto-optic devices. It holds promise for pushing research in material science, photonics, and sensing technologies toward higher spatial resolution and sensitivity, marking a significant step toward practical, room-temperature Brillouin-based spectroscopy and sensing solutions.

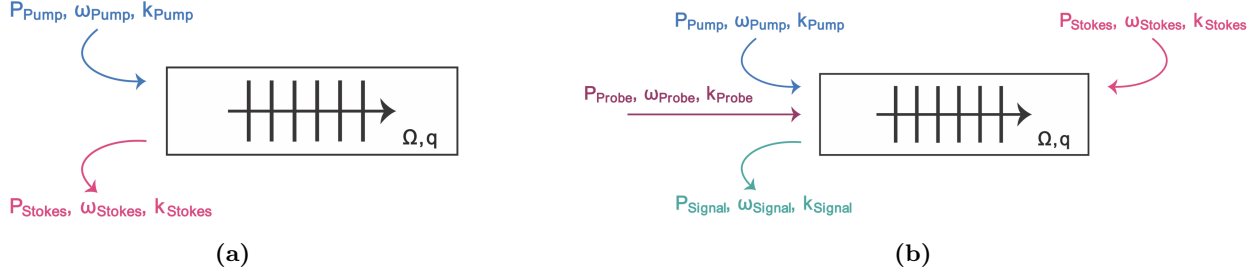


Figure 3.1: Figure 3.1a illustrates standard (three-wave) stimulated Brillouin scattering (SBS), showing a single optical pump field P_{Pump} , the backscattered Stokes field P_{Stokes} , and the acoustic (phonon) wave of frequency Ω and wavevector q . Here, ω_i and k_i represent the frequency and wavevector of the optical fields, respectively. Figure 3.1b illustrates coherently stimulated (four-wave) Brillouin scattering (CoBS), where an additional optical probe P_{Probe} mixes with the pump to generate both the Stokes wave and a new signal P_{Signal} , mediated by the same acoustic wave. We refer to this as four-wave because four optical fields (pump, probe, Stokes, signal) participate, although one may also count the acoustic wave as a “fifth” wave.

3.3 Theoretical Framework

3.3.1 Coherently Stimulated Four-Wave Brillouin Scattering

Traditional SBS, illustrated in Figure 3.1a, is a three-wave mixing process in which incident pump laser light of frequency ω_{Pump} inelastically scatters from a traveling-wave phonon of frequency Ω to produce light that is frequency-shifted by the phonon frequency. In the Stokes process the phonon is retreating from the incident laser light and the scattered light is shifted down in frequency ($\omega_{\text{Stokes}} = \omega_{\text{Pump}} - \Omega$). Spatial overlap of the backscattered light with the incident laser light allows for interference of the two optical fields to produce a frequency at the difference of the two ($\omega_{\text{Pump}} - \omega_{\text{Stokes}}$). Since this difference frequency is exactly equal to the frequency of the acoustic field Ω , the beating of the incident pump light with the backscattered Stokes light produces an electrostrictive reinforcement of the acoustic wave. This driving of the acoustic wave in turn increases the scattering rate of the incident pump light, producing a positive feedback process and an exponential increase of the amplitude of the backscattered Stokes wave.

Figure 3.1b illustrates coherently stimulated four-wave Brillouin scattering for the Stokes process, mediated by an acoustic wave. We introduce a strong, controlled external Stokes wave of frequency ω_{Stokes} that drives electrostrictive reinforcement of the acoustic field in the medium. The backscattered Stokes light is normally collected in an SBS process, but the external Stokes laser overwhelms it. To resolve this, we inject light of a distinct frequency ω_{Probe} from an additional external laser which copropagates with the Pump and backscatters in the medium from the strongly driven acoustic field. This produces backscattered Signal light to be collected ($\omega_{\text{Signal}} = \omega_{\text{Probe}} - \Omega$) which is spectrally distinct from the high-powered Stokes laser light.

To describe this interaction and characterize the performance of the instrument, we derive the coupled-

wave equations for the four-wave mixing process in Appendix B.1. These equations describe the relationship between the optical fields and the acoustic field in the material and result in the following expression for the scattered power of the backscattered signal,

$$P_{Sig} = \frac{1}{4}(G_B L)^2 P_P P_S P_{Pr} \text{sinc}^2\left(\frac{\Delta k L}{2}\right), \quad (3.1)$$

where P_P , P_S , and P_{Pr} are the powers of the pump, Stokes, and probe lasers, respectively. G_B is the effective Brillouin gain, given by

$$G_B = \frac{g_0}{A_{eff}} \frac{\left(\frac{\Gamma_B}{2}\right)^2}{(\Omega - \Omega_B)^2 + \left(\frac{\Gamma_B}{2}\right)^2}, \quad (3.2)$$

with the on-resonance gain factor of the material given by

$$g_0 = \frac{\gamma_e^2 \omega^2}{n v c^3 \rho_0 \Gamma_B}. \quad (3.3)$$

Here, γ_e is the electrostrictive constant, ω is the pump frequency, n is the refractive index of the material, v is the sound speed of the material, c is the speed of light, ρ_0 is the mean density of the material, and Γ_B is the Brillouin linewidth, or phonon dissipation rate, of the material. In Equation 3.2, Ω_B is the resonant Brillouin frequency of the material, A_{Eff} is the effective area of the material, Δk is the wavevector mismatch between the optical fields, to be discussed next, and L is the effective length of the material.

3.3.2 Phase Matching Relaxation

In all nonlinear optical processes, efficiency is maximized when phase matching conditions are satisfied. A frequency mismatch (energy unconservation) or a wavevector mismatch (momentum unconservation) each result in drastically reduced efficiency of a given process.⁵³ This can be seen by Equation 3.1, where the wavevector mismatch, Δk , is contained within a sinc^2 function. This sinc^2 term thereby defines the phase matching bandwidth of the system, notably scaling with effective interaction length L .

We apply this wavevector mismatch allowance to the pump and probe waves ($\Delta k = k_{\text{Pump}} - k_{\text{Probe}}$) so that the backscattered signal is different than the applied Stokes wave. This choice allows for selection of the signal and rejection of the Stokes with a bandpass filter. Expressed in terms of wavelengths, this gives

$$\Delta k = \frac{4\pi n \Delta \lambda}{\lambda_{Pump} \lambda_{Probe}} \approx \frac{4\pi n \Delta \lambda}{\lambda_{Pump}^2}. \quad (3.4)$$

We can apply this to the phasematching bandwidth term to find the fraction of maximum scattered power, Φ , that can be expected for a given interaction length, L , and phase mismatch $\Delta\lambda$ between the pump and probe,

$$\Phi \equiv \text{sinc}^2 \left(\frac{2\pi n \Delta \lambda L}{\lambda_{Pump}^2} \right). \quad (3.5)$$

Using this expression for Φ , we see that for an effective length of 1 m, a wavelength mismatch of only 0.6 pm from a typical wavelength of 1.55 μm pump light in UHNA3 fiber drops the scattered power to half of the maximum. However, for shorter effective lengths the wavevector mismatch becomes more forgiving; a 36 pm mismatch preserves 82.5% of the maximum signal for a length of 1 cm under identical conditions. This separation translates to about 4.5 GHz, providing enough spectral separation for the backscattered signal to be isolated from the applied Stokes light.

Furthermore, for decreasing lengths, Equation 3.5 predicts an increase in the fraction of maximum signal produced, given equivalent pump–probe detuning, as the sinc^2 function is sampled closer to its peak center. Alternatively, as length decreases, the probe may be further detuned from the pump and still achieve the same fraction of the maximum signal as for longer lengths, perhaps offering a slight advantage in noise reduction. It should be noted that the scattered power, as given by Equation 3.1, scales with the square of the effective length. Thus, while smaller lengths allow for the ability to capture a larger fraction of this maximum scattered power, the actual amount of scattered power decreases dramatically as length decreases.

3.4 Methods

3.4.1 Instrument Design

Figure 3.2 shows the instrument’s design. A pump and Stokes wave is synthesized from a single tunable laser source for coherent stimulation of a sample. The pump wave (ω_{Pump}) is amplified by an Erbium-Doped Fiber Amplifier and passed through a Variable Optical Attenuator for power control. The output is then polarization-controlled to reflect at a polarizing beam splitter for injection into the sample. For Stokes synthesis, an alternating current signal (Ω) is supplied to an fiber-optic intensity modulator with carrier frequency nulled and a tunable filter is used to select the lower-frequency Stokes side band ($\omega_{Pump} - \Omega$). This Stokes light is then amplified by an EDFA, passed through a VOA, and polarization-controlled to reflect

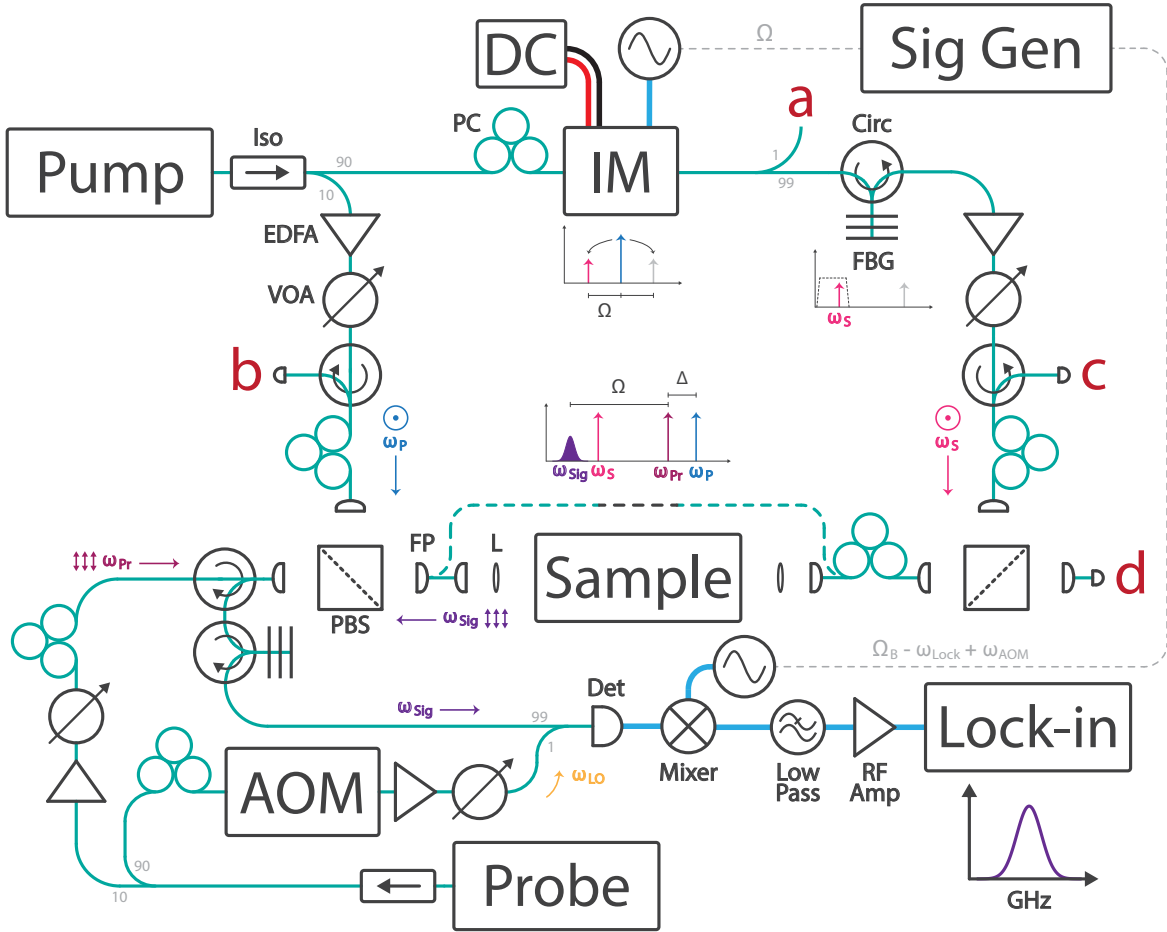


Figure 3.2: Design schematic of a coherently stimulated phonon spectrometer. A tunable Continuous Wave (CW) laser at approximately $1.55\text{ }\mu\text{m}$ emits light that passes through an isolator (Iso) and a splitter, diverting 10% to a 27 dBm Erbium-Doped Fiber Amplifier (EDFA) followed by a Variable Optical Attenuator (VOA). This pump light (ω_P) is polarization-controlled to reflect off a polarizing beam splitter (PBS) and is recoupled to fiber via a fiber port (FP), then directed to the sample either by direct fiber coupling or through a pair of FPs and lenses (L) for free-space samples. After passing through the sample, the pump light traverses a corrective polarization controller that mitigates fiber twists and bends before reflecting off a second PBS, where it is routed to port (c) for power monitoring. To synthesize the Stokes wave, a 90% split from the original pump is processed through a fiber-optic intensity modulator (IM) and a fiber Bragg grating (FBG), generating a Stokes sideband downshifted from the pump by Ω . This frequency shift is swept via a signal generator to capture Ω_B . A 99/1 splitter provides a tap at port (a) to optimize Stokes synthesis. The Stokes wave (ω_S), amplified by a 1 W EDFA and VOA-controlled, counter-propagates along the pump path and is monitored at port (b). A second tunable CW laser, detuned from the pump, generates the probe wave (ω_{Pr}), which is amplified by a 1 W EDFA, attenuated variably, and polarization-controlled to pass through the initial PBS where it is incident on the sample. Backscattered signal light (ω_{Sig}) transmits back through the PBS, while unscattered probe light transmits to a power meter at port (d). A circulator parts the signal from the probe path, with an FBG filtering out any unwanted noise or Stokes light. Finally, the signal is heterodyned with an EDFA-amplified, acousto-optic modulator (AOM)-shifted local oscillator (LO) derived from the probe laser and directed to a photodiode for detection. The resulting radio frequency (RF) signal is mixed with an alternating current (AC) LO supplied by the signal generator which sweeps synchronously with the Stokes synthesis frequency, and collected by a lock-in amplifier for data processing.

at a second PBS for counter-propagation to the pump through the sample.

A separate tunable laser is used to supply a probe wave ($\omega_{\text{Probe}} = \omega_{\text{Pump}} + \Delta k$) and local oscillator. Probe light is amplified by an EDFA and passed through a VOA and a polarization controller aligns the polarization for transmission through the first PBS whereby it copropagates with the pump through the sample. Backscattered light exits the sample and transmits back through the first PBS, whereas the orthogonally polarized Stokes light reflects at this same point to be diverted to a tap for power monitoring. The backscattered signal ($\omega_{\text{Signal}} = \omega_{\text{Probe}} - \Omega$) then routes through two subsequent circulators for spectral filtering by a 5 GHz bandpass tunable filter. This filter allows the desired backscattered signal to pass while rejecting any reflected probe light as well as any reflected, transmitted, or backscattered light from the pump or Stokes waves that was not already diverted by the PBS.

The filtered signal then heterodynes via a 99-1 splitter with the LO which is frequency-upshifted by an acousto-optic modulator ($\omega_{\text{LO}} = \omega_{\text{Probe}} + \omega_{\text{AOM}}$) and controlled to be copolarized with the signal. Of the resulting frequencies from the heterodyne process, only the difference frequency term is considered, as all others are beyond the range of detection. This heterodyned signal ($\omega_{\text{Signal}} = \Omega + \omega_{\text{AOM}}$) is then captured by a photodiode detector and heterodyned again by a radio frequency mixer with a second AC signal ($\Omega + \omega_{\text{AOM}} - \omega_{\text{Lock}}$), where ω_{Lock} is a fixed-frequency to be detected by a lock-in amplifier set to this frequency after being passed through a low-pass filter and amplified by an RF amplifier. Synchronous sweeping of both AC signals, each involving Ω , allows for ω_{Lock} to remain fixed throughout measurement over a frequency range.

3.4.2 Experimental Techniques

We optimized the signal-to-noise ratio (SNR) of the instrument through specific design choices and device settings. Our setup simultaneously generates pump, Stokes, and probe optical fields for coherently stimulated Brillouin scattering. The pump laser provides ~ 45 mW total output, of which 10% is split and amplified to ~ 0.5 W for the pump field; the remaining 90% is frequency-shifted and amplified to ~ 1 W for the Stokes field. Likewise, the probe laser also outputs ~ 45 mW, with 10% amplified to ~ 1 W for the probe field and the remaining 90% reserved for the LO. To combine the backscattered signal and LO with minimal loss, we use a 99/1 splitter instead of a typical 50/50, preserving 99% of the signal. The LO is therefore amplified to ~ 230 mW so the total optical power at the detector remains below the 2.4 mW damage threshold. After detection, the electronic signal is mixed with a 17 dBm AC reference and further amplified by 23 dBm before input to the lock-in amplifier. We find that running both the pump and probe lasers in “whisper” mode (as opposed to “dither”) significantly enhances the measured SNR.

We use a Zurich Instruments HF2LI 50 MHz lock-in amplifier whose demodulator settings are carefully tuned to maximize SNR. A 10 MHz reference clock from the signal generator is fed into the lock-in to synchronize timing. The input-signal range, which sets the analog input amplifier’s gain, should exceed the measured signal (including any direct current (DC) offset) by at least a factor of two. This is best achieved by using the lock-in software’s auto feature, which continuously adjusts the range over a rolling 100 ms window. We set the input coupling to AC, insert a high-pass filter to remove DC components, and choose $1\text{ M}\Omega$ input impedance. For noise suppression, we also engage the lock-in’s eighth-order low-pass filter (roll-off 48 dB Oct^{-1}) and sample the data at 1.84 MSa s^{-1} , the maximum rate available.

Further SNR improvements are gained by narrowing the lock-in’s low-pass filter bandwidth to match both the sub-Hz natural linewidth of the heterodyne signal and the thermally-driven frequency drift of the apparatus. After a ~ 30 min warm-up, we observe less than 100 Hz of drift in the detected signal frequency, so we typically set a 100 Hz low-pass bandwidth for multi-hour measurements. For shorter scans (< 15 min), we can reduce this bandwidth to 40 Hz if needed. In addition to linewidth variability, the signal’s center frequency can shift due to thermal changes in the AOM and related electronics. Although Ω is nominally controlled to sub-hertz precision by the signal generator, our AOM’s shift ω_{AOM} drifts from 40 MHz up to $\sim 40.000\,82$ MHz over roughly 30 min. Once at thermal equilibrium, the AOM remains stable within ± 50 Hz, enabling a reliable lock-in frequency reference and minimal filter bandwidth. This stability is crucial for repeatable, high-resolution Brillouin measurements.

3.5 Results

3.5.1 Instrument Sensitivity

We begin by testing the sensitivity of the instrument as a way of defining a performance metric for the instrument which can be used to indicate what material, power, and length combinations might be possible to measure. From Equation 3.1, the sensitivity of the instrument is the minimum scattered power, P_{Sig} , to produce a statistically significant measurement. To determine this, we target a specific length, L , of a sample of known effective Brillouin gain, G_B . We keep the pump-probe detuning, $\Delta\lambda$, constant across measurements and record the pump, Stokes, and probe optical powers to calculate the scattered power. Starting with sufficient optical powers to produce a clearly distinguishable measurement, we gradually reduce the optical powers until the sensitivity floor is reached.

To serve as our sensitivity testbed, we prepared 1 cm of Nufern’s Ultra High Numerical Aperture 3 fiber, a well-studied fiber with known effective Brillouin gain⁵⁴. Additionally, UHNA3 fiber offers several properties that make it ideal for this task of unambiguous detection of the Brillouin signal as it diminishes with each

CoBS Measurement: 1 cm UHNA3

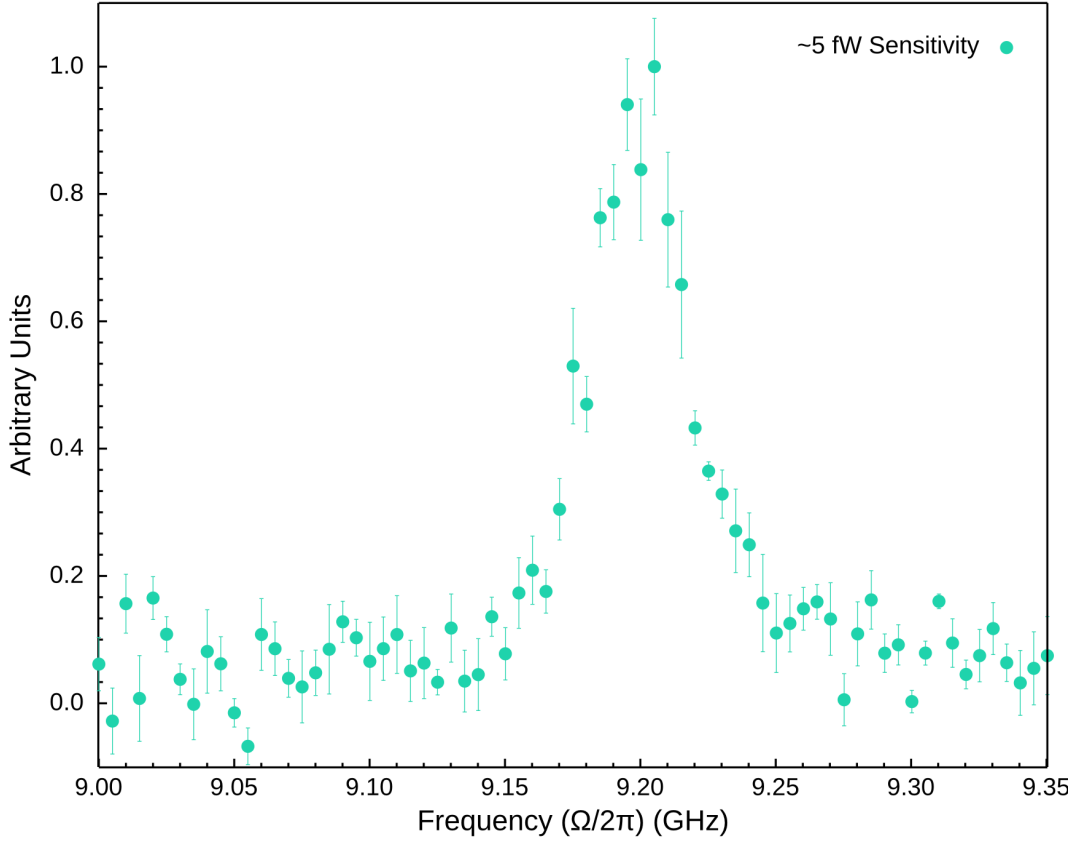


Figure 3.3: Observed spectra demonstrating $P_{\text{Signal}} \approx 5 \text{ fW}$ sensitivity of the instrument. Experimental parameters for this measurement are tabulated in Table 3.1. In obtaining the spectra, five repeated measurements of both the signal and background (probe off) were collected at a 100 Hz resolution bandwidth (RBW), dwelling for 1 s at each 5 MHz frequency step. Plotted is the resulting background-subtracted spectrum. Uncertainties represent 1σ standard error of the mean. By comparing the peak amplitude at resonance to the off-resonance baseline, we estimate an SNR greater than 5, which, under a normal-noise assumption, corresponds to a 5σ significance level (99.99994% confidence).

subsequent reduction in optical powers. First, it offers a Brillouin shift that is spectrally far from that of the single mode fiber 28 (SMF-28) which constitutes much of the instrument. This ensures that the Brillouin response of the sample is not conflated with the Brillouin response of the instrument itself. Additionally, the core of UHNA3 fiber features a high concentration of germanium which improves the optical and acoustic guidance in the fiber as a result of the large refractive index difference between core and cladding. Finally, UHNA3 fiber offers a high optomechanical nonlinear response, with an effective Brillouin gain of $0.6 \text{ W}^{-1} \text{ m}^{-1}$ measured at room temperature⁵⁴. This gain factor is larger than that of SMF-28 by an order of magnitude⁵⁵.

Figure 3.3 presents a measurement in which the instrument's sensitivity reaches $P_{\text{Sig}} = 2 \text{ fW}$. Table 3.1 provides the experimental parameters used to gather this measurement and calculate the sensitivity. Each trace is the average of five consecutive scans, and an average of five background scans has been subtracted

to isolate the signal. Error bars represent the standard error (1σ of the mean). By comparing the peak amplitude at resonance to the off-resonance baseline, we estimate an SNR greater than 5. Under a normal-noise assumption, an SNR of 5 corresponds to a 5σ significance level (99.7% confidence). Achieving this 5 fW threshold demonstrates the feasibility of measuring weaker signals in materials with lower Brillouin gain or smaller effective lengths.

G_B (W $^{-1}$ m $^{-1}$)	L (m)	P_P (μ W)	P_S (μ W)	P_{Pr} (mW)	$\Delta\lambda$ (pm)	Φ
0.6	0.01	506	504	2.01	20	0.90

Table 3.1: Experimental parameters used in observing $P_{Sig} \approx 5$ fW sensitivity of the Coherently stimulated Brillouin Spectrometer (CoBS) instrument. The resulting spectra is shown in Figure 3.3.

3.5.2 Measurements

We demonstrate the capabilities of the instrument on two common sample classes: fiber and bulk material. For a fiber sample we again choose UHNA3 for its higher nonlinear response and excellent optical and acoustic guidance. In contrast to the sensitivity measurements, we now seek to demonstrate the full measuring capabilities of the instrument and so apply all available optical power (~ 1.5 W) to maximize the backscattered signal from the sample. We target the same 1 cm segment of UHNA3 fiber as was used for determining sensitivity.

Figure 3.4 shows the spectral profile captured for 1 cm of UHNA3 fiber, revealing the expected lorentzian profile consistent with Equation 3.2. The peak amplitude of the spectra occurs at 9.1704 GHz, indicating the Brillouin resonance frequency of the longitudinal traveling-wave mode in the fiber. The full-width half-max (FWHM) linewidth of the measurement is 80 MHz and provides a measure of the phonon dissipation rate. Both values match what is seen in the literature for SBS measurements of UHNA3 fiber.⁵⁴ The data shown are a background-subtracted average of five successive measurements taken over ten minutes with error bars corresponding to 1σ of the mean.

To achieve this measurement of UHNA3 fiber, the instrument design was altered to include only fiber-coupled segments connecting the fiber ports between the two PBSs. We set the pump laser wavelength to 1549.000 nm and the probe laser wavelength to 1549.020 nm, giving a frequency mismatch of approximately 2.5 GHz. The pump–probe mismatch is chosen to be only as large as needed to allow the edge of the passband of the probe filter to split the backscattered pump and probe light, thus rejecting any backscattered light from the pump laser and accepting only the backscattered signal from the probe laser. We placed the Stokes filter at 1549.073 nm, an offset of approximately 9.18 GHz from the pump laser to capture the Stokes

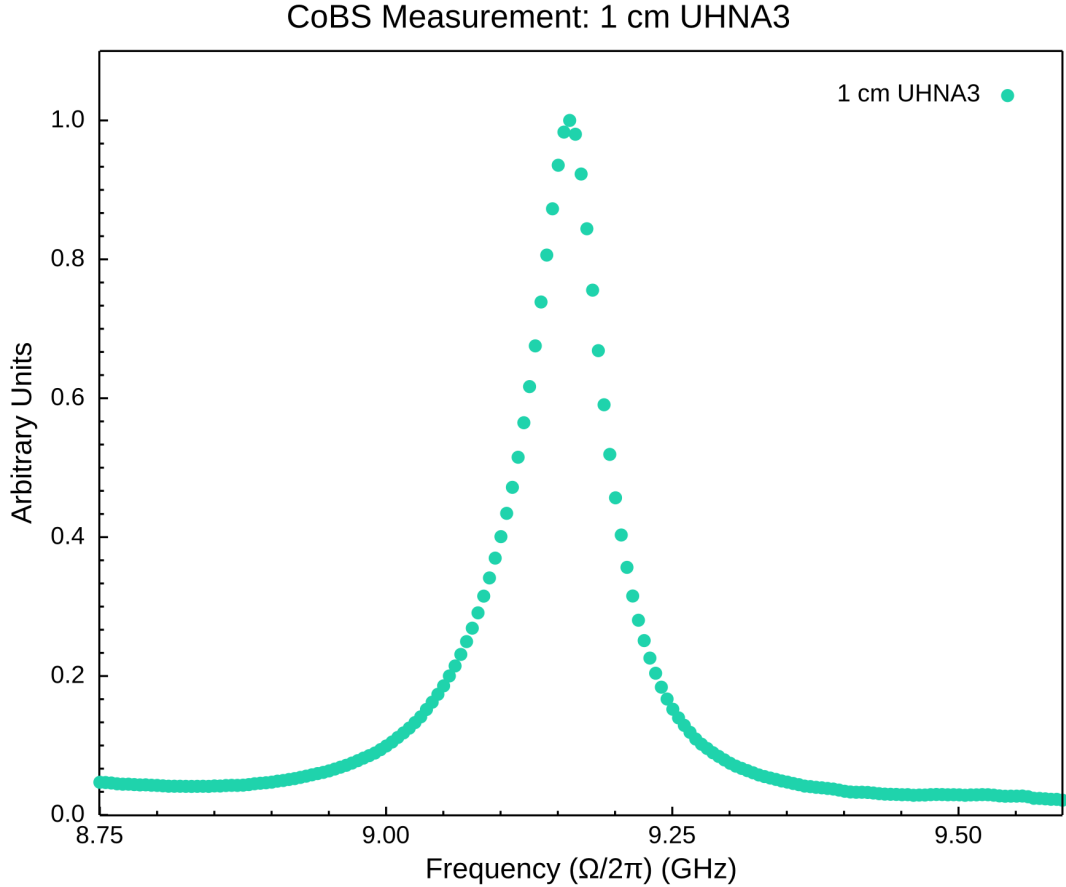


Figure 3.4: Observed spectra of 1cm UHNA3 fiber captured at maximum operating optical powers $P_P P_S P_{Pr} \sim 0.25 \text{ W}^3$. The data exhibits the familiar Lorentzian profile for frequency-dependent dissipation probed by Brillouin scattering. This response is reflected in the CoBS process gain $G_{\text{CoBS}} = \frac{1}{4}(G_{BL})^2 P_P P_S P_{Pr}$ given in Equation 3.1, with Equation 3.2 for effective Brillouin gain offering the off-resonant Lorentzian lineshape. In obtaining the spectra, five repeated measurements of both the signal and background (probe off) were collected at a 100 Hz RBW, dwelling for 1 s at each 5 MHz frequency step. Plotted is the resulting background-subtracted spectrum, with 1σ uncertainties smaller than the data point markers.

sideband from the intensity modulator. This corresponds to the center of the measured frequency range and was chosen to allow the Stokes sideband output from the intensity modulator to remain within the pass band of the Stokes filter as the RF signal fed to the intensity modulator is swept through the full measurement range. The probe filter was set to 1549.109 nm, an offset of approximately 11.18 GHz from the probe laser, to capture the Stokes-shifted backscattered signal from the probe. The center frequency of the backscattered signal is of course shifted 9.18 GHz from the probe laser, however an extra offset of 2 GHz is chosen for improved rejection of any pump light as the pass band of our filter extends approximately 2.5 GHz on either side of center.

For a free-space bulk example we target liquid CS₂ for its exceptionally high Brillouin gain factor of

CoBS Measurement: 100 μm CS₂

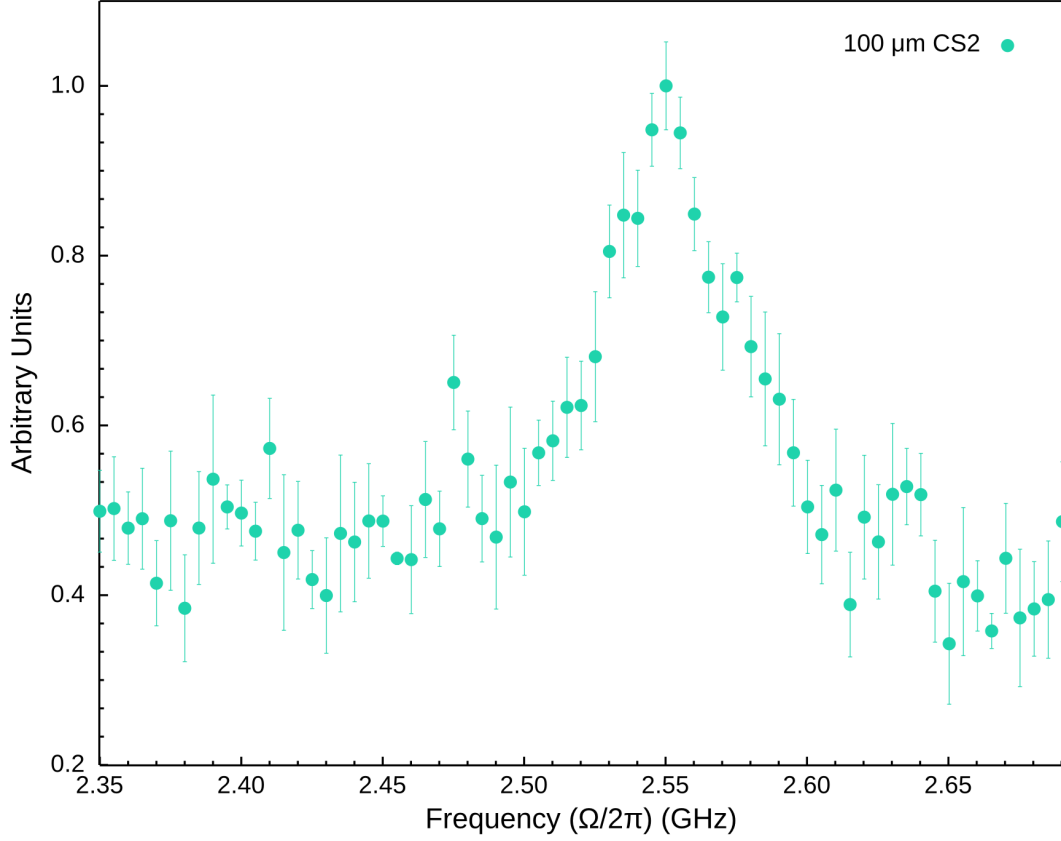


Figure 3.5: Observed spectra of 100 μm liquid CS₂ captured at maximum operating optical powers $P_{\text{P}}P_{\text{S}}P_{\text{Pr}} \sim 0.25 \text{ W}^3$. Within the uncertainties, the data exhibits the familiar Lorentzian profile for frequency-dependent dissipation probed by Brillouin scattering. This response is reflected in the CoBS process gain $G_{\text{CoBS}} = (G_{\text{BL}})^2 P_{\text{P}}P_{\text{S}}P_{\text{Pr}}$ given in Equation 3.1, with Equation 3.2 for effective Brillouin gain offering the off-resonant Lorentzian lineshape. In obtaining the spectra, five repeated measurements of both the signal and background (probe off) were collected at a 100 Hz RBW, dwelling for 1 s at each 5 MHz frequency step. Plotted is the resulting background-subtracted spectrum. Uncertainties represent 1σ standard error of the mean.

1.5 m GW⁻¹.³ Figure 3.5 reveals the Brillouin signal of bulk CS₂ liquid contained in a 100 μm path length cell. To our knowledge, measurement of longitudinal Brillouin scattering at this scale has not been reported in the literature. A scattered power comparison would reveal that achieving such a measurement using traditional SBS techniques would require excessively high optical powers or cooling the material to cryogenic temperatures, which, of course, would be prohibitive for carbon disulfide in the liquid state.

For this measurement of CS₂, the pump and probe laser wavelengths were set to 1548.808 nm and 1548.898 nm, respectively. The short path length of the sample significantly broadens Φ , the sinc² term defining the phasematching bandwidth, allowing for further separation of the pump and probe wavelengths for improved signal isolation without significant reduction in scattered power of the signal produced in the

CS_2 . Specifically, the additional pump–probe wavelength separation of 70 pm employed for this measurement compared to the UHNA3 measurement results in a negligible 0.045% reduction in scattered power. This additional separation contributes meaningfully, however, to improved rejection of pump light by the probe filter and thus higher SNR of the signal.

Placement of the Stokes filter is critical for measurements of materials that give small Brillouin shifts, such as with CS_2 2.55 GHz shift. We offset our 5 GHz bandwidth Stokes filter an additional 2 GHz to ensure the nearby carrier signal and anti-Stokes sideband from the intensity modulator are rejected and only the Stokes sideband is allowed to pass. For the measurement shown in Figure 3.5, this corresponds to a Stokes and probe filter placement of 1548.844 nm and 1548.934 nm, respectively.

3.5.3 Phase Matching Bandwidth

To characterize the phase matching tolerance of the instrument for a given length of sample, we performed an additional experiment whereby we took a series of measurements of 1 cm of UHNA3 at constant optical powers while letting the detuning of the pump and probe lasers vary. In the language of Equation 3.1, this experiment holds G_B , L , P_P , P_S , and P_{Pr} constant while letting Δk vary. For the experiment to support the validation of Equation 3.1, we would expect the peak amplitudes of these measurements to trace out a sinc^2 profile, also given by Equation 3.5. Figure 3.6 shows the results of this experiment. We performed 75 measurements between 5 GHz and 42 GHz pump–probe detuning, at 0.5 GHz intervals. We found peak amplitudes by fitting each spectra with a Fano profile (see Section 3.5.4) and represented each peak as a data point in Figure 3.6. The theoretical sinc^2 function matching the parameters used in the experiment is shown on the plot with a solid red line.

3.5.4 Fano-Resonant Asymmetries at Small Signals

Under certain conditions where the resonant Brillouin amplitude approaches the background continuum level, we observe an asymmetric, Fano-type line-shape^{56–59}. These Fano distortions can shift the apparent peak frequency, complicate simple Lorentzian fitting, and affect the extracted linewidth in small-signal measurements.⁶⁰ To properly handle these occurrences, it is necessary to understand when they are likely to arise with this technique and how they may be corrected for or controlled. Fano resonances arise when a discrete resonance (in our case, the Brillouin mode) interferes with a continuum background (e.g., noise floor or broad, non-resonant scattering). When the resonance amplitude is no longer much larger than the continuum, the interference leads to an asymmetric line-shape described by the Fano formula⁵⁶,

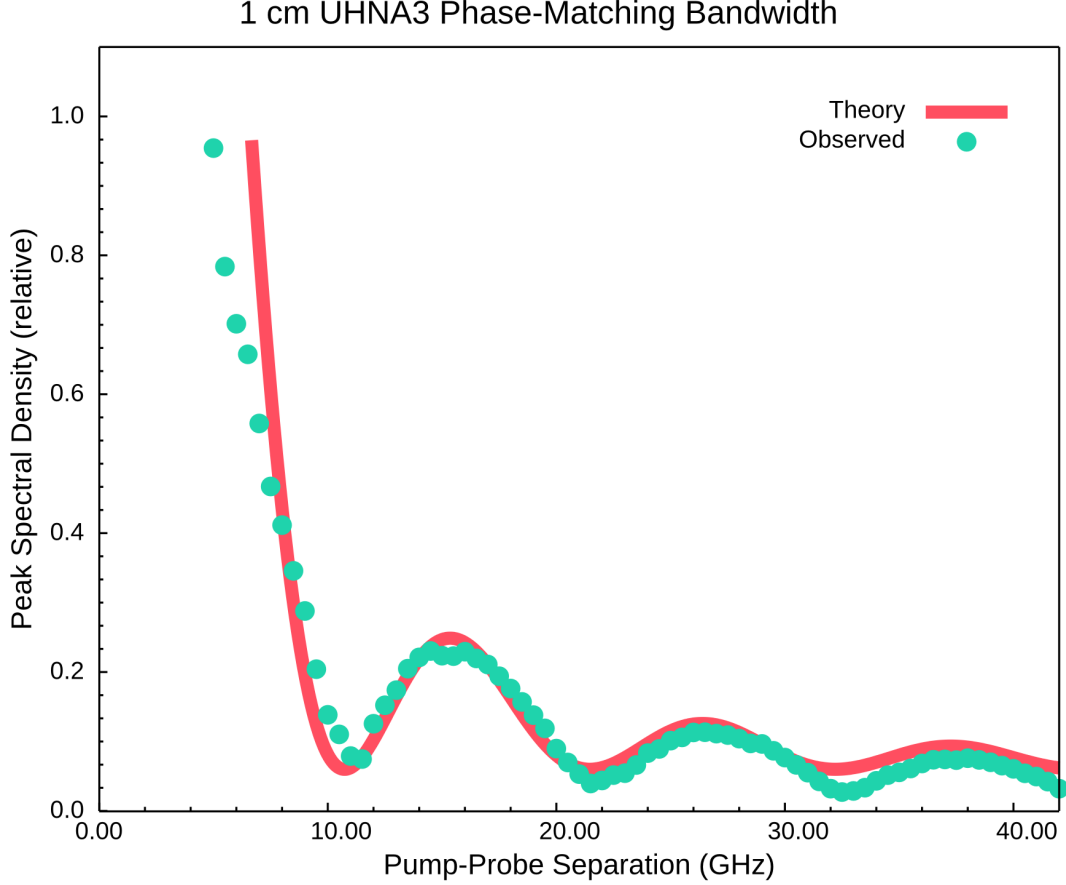


Figure 3.6: Spectral peaks of 75 observed spectra of (1 ± 1) cm UHNA3 across a range of pump-probe detunings $(\omega_{\text{Pump}} - \omega_{\text{Probe}})/2\pi$ from 5 GHz-42 GHz in 0.5 GHz increments. Values are obtained from uncertainty-weighted Fano fits of the observed spectra (see Appendix B.3). The solid theoretical line shows the expected theoretical trend (a sinc^2 lineshape) given by Equation 3.5, plotted here for the experimental parameters used in collecting the data and a fiber length of ~ 0.9 cm. Section B.3.1 in Appendix B.3 offers an extended discussion of the observed spectra and contains a plot of the full set of 75 spectra (Figure B.3.1). In obtaining each spectra, five repeated measurements of both the signal and background (probe off) were collected at a 100 Hz RBW, dwelling for 1 s at each 5 MHz frequency step. Uncertainty-weighted Fano fits were computed from the resulting background-subtracted spectra. Plotted here are the fit-extracted spectral peaks, with 1σ uncertainties smaller than the data point markers.

$$I(\omega) \propto \frac{(q + \epsilon)^2}{1 + \epsilon^2}, \quad (3.6)$$

where $\epsilon \equiv (\Omega - \Omega_B)/(\Gamma_B/2)$ is the dimensionless detuning from the Brillouin peak (measured in half the spectral linewidth) and q is the Fano asymmetry parameter. The Fano asymmetry parameter captures the ratio of the resonant scattering to the background scattering amplitudes as well as the relative phase of each. It can be defined as

$$q = \frac{(\text{resonant amplitude})}{(\text{background amplitude})} \cot(\Delta\phi), \quad (3.7)$$

where $\Delta\phi$ is the phase difference between the oscillation driven by the discrete resonant mode and that of the background continuum^{57,61,62}.

In the event of Fano interference, the complex background amplitude often varies slowly with energy and can be seen as having a fixed phase reference, while the resonant amplitude undergoes a rapid π phase change as the energy passes through the resonance.⁵⁷ When the resonant and background contributions are exactly out of phase at the resonance frequency (phase difference $\Delta\phi = \pi/2$, meaning destructive interference), the spectral line exhibits a dip to zero (anti-resonance) at the discrete resonance frequency, corresponding to $q = 0$ in Equation 3.6. If they are exactly in phase ($\Delta\phi = 0 \text{ or } \pi$, fully constructive interference at resonance), the resonance appears purely Lorentzian without asymmetry and $|q| \rightarrow \infty$. For intermediate phase offsets, one lobe of the resonance is enhanced while the other is suppressed, yielding an asymmetric peak or dip with finite q . The sign of q indicates the direction of asymmetry (which wing of the resonance is enhanced). A positive q means the discrete mode *leads* the background in phase. In this case, the spectral profile has a sharp rise on the low-frequency side and a more gradual fall-off on the high-frequency side. Conversely, a negative q means the discrete mode *lags* the background in phase, leading to a flipped orientation featuring a sharp rise on the *high*-frequency side and a gradual fall-off on the *low*-frequency side.

We first noticed this behavior appearing in our small-length CS₂ data, where a small shift in probe wavelength revealed an asymmetric line-shape. For the measurements of 100 μm CS₂ (Figure 3.5) and 1 cm UHNA3 fiber at low power (Figure 3.3), the amplitude of the resonant Brillouin peak is on the order of that of the non-resonant continuum, giving a strong chance for Fano interference. Whenever $\frac{I_{\text{res}}}{I_{\text{bkg}}} \approx 1$, the parameter q as given by Equation 3.6 can become finite rather than $\pm\infty$ in the limit that the background is negligible, and Fano interference arises. To explore this further, we performed a similar phase-matching experiment as was done for 1 cm UHNA3 (see Phase Matching Bandwidth subsection), this time with 1 mm of CS₂. Results from this experiment are presented in Appendix B.3 and offer examples of line shapes with pronounced asymmetry and featuring clear characteristic morphologies associated with Fano interference. These pronounced distortions in spectral line shape for small signal measurements underscore the role Fano interference in small resonant amplitudes relative to the background.

Because our instrument offers sub-10 fW sensitivity signal amplitudes have the potential to approach the order of the background continuum amplitude. For this reason, and because the instrument offers an advantage in measurements of samples of short length (<10 m) (see Appendix B.2), Fano effects may often arise with usage of this technique and must be handled appropriately. This includes properly fitting data

with a Fano profile as opposed to a Lorentzian to ensure accurate capture of relevant parameters such as linewidth, resonant frequency, and peak amplitude. Beyond fitting and parameter extraction, it is important to be mindful that these effects are likely to occur in ambitious measurements at the limits of equipment sensitivity. Expectation and proper handling of Fano effects in measurements of this nature ensures that they may be more easily recognized and confirmed, as the data is likely to present a spectrum that deviates considerably from the standard Lorentzian. Appendix B.2 offers a comparative analysis of two example spectra featuring highly assymetric profiles fitted with a naïve Lorentzian vs. a more appropriate Fano function.

In some cases, and of particular interest for ambitious measurements, Fano interference may even *boost* the measured peak above the naïve Lorentzian amplitude—i.e., ‘amplify’ it—when $q \neq 0$. In principle, a Fano-type lineshape can exhibit a locally higher peak amplitude than a pure Lorentzian if the discrete Brillouin response constructively interferes with the background continuum near the resonance. Crucially, this does not represent net energy gain but rather a redistribution of intensity through interference. Although the resonance peak may appear taller, the continuum also contributes noise and can partially interfere destructively elsewhere, so the global SNR may or may not improve. Nonetheless, our technique offers the ability to dynamically tune the phase of the Brillouin response relative to the background via adjustment of the probe laser wavelength. This interference-tuning of the continuum and discrete components allows some control over constructive or destructive interference. Moreover, we can achieve this without sacrificing independent control of the pump–probe detuning: by simultaneously shifting the pump laser in step with the probe, we can preserve the desired phase-matching bandwidth while optimizing the relative phase for Fano interference.

In the phase-matching bandwidth experiment on 1 cm of UHNA3 fiber (Figure 3.6), several effects—noise floor, alignment drifts, fiber dispersion, etc.—slightly distort the ideal sinc^2 response. Near the troughs of the sinc^2 function and for larger pump–probe detunings, the measured Brillouin peaks are weaker and exhibit small spectral asymmetries (see Appendix B.3). This is consistent with a Fano-type distortion in which the Brillouin amplitude and background continuum are comparable, allowing interference to skew the lineshape and shift the peak away from the naïve Lorentzian center. Consequently, a simple Lorentzian fit underestimates the true peak amplitude in these regimes. By fitting a standard Fano profile, we more accurately capture the asymmetric peak and its shifted center frequency.

3.6 Conclusion

In conclusion, we have introduced a coherently stimulated Brillouin spectrometer utilizing a detuned pump-probe design to achieve high sensitivity and room-temperature operation in μm -scale samples. This approach successfully overcomes the spatial resolution limitations imposed by conventional SBS methods, demonstrating sub-10 fW sensitivity in UHNA3 fiber and enabling Brillouin measurements in bulk liquid carbon disulfide with unprecedented efficiency. By relaxing phase-matching constraints, this instrument opens new possibilities for characterizing nanoscale material properties and developing nano-acousto-optic devices in standard laboratory settings without the need for cryogenic environments. Moving forward, our methodology could facilitate advancements in high-resolution phonon spectroscopy and inspire further innovations in the study of material mechanics at the microscale, reinforcing the broader applicability of Brillouin-based techniques across materials science, photonics, and sensing technologies.

Chapter 4

Brillouin-Induced Raman Modes and Device Exploration

4.1 Introduction

This chapter explores progress towards the goal of demonstrating Brillouin-induced Raman-like modes at room temperature. We aim to show that acoustic traveling-wave phonons generated by a Brillouin scattering process in a confined medium can organize into discrete standing-wave vibrational modes. This goal represents a convergence of several themes in modern photonics: cavity optomechanics, coherent phonon control, and nonlinear light–matter interactions. Cavity optomechanics has traditionally focused on discrete mechanical resonances such as drumhead membranes or whispering-gallery (whispering-gallery-mode (WGM)) microresonators to achieve effects like laser cooling of vibrational modes or phonon lasing.^{11,12,63,64} In parallel, Brillouin scattering provides a route to manipulate traveling-wave acoustic phonons in extended media, as demonstrated by our Brillouin-based laser cooling in optical fiber (a “cavity-less” system).^{1,13,14,31} The research in this chapter aims to bridge these domains, leveraging traveling-wave Brillouin scattering in a finite-length system so that the phonons become self-confined, resembling the vibrational modes that give rise to Raman scattering.

This investigation is grounded in the broader context of controlling phonons and light at the mesoscale. High-coherence phonons are garnering interest for precision metrology and quantum information,^{65,66} spurring new strategies for phonon coherent optomechanical interactions.^{12,63} Earlier chapters of this dissertation advanced this frontier: Chapter 2 demonstrated the laser cooling of propagating acoustic phonons in an optical fiber, extending optomechanical control to continuous media at room temperature,¹ and Chapter 3 introduced a novel Brillouin spectrometer which offers especially high sensitivity for short (<1 cm) lengths over traditional Stimulated Brillouin Scattering (SBS). Building on such results, the present work tackles the next challenge: inducing standing-wave acoustic modes in a bulk-like sample through Brillouin processes. Achieving this at room temperature would be significant, as to date strong acoustic mode formation has been mostly limited to cryogenic systems where phonon lifetimes are long.^{14,67} By pursuing Brillouin-induced modes under ambient conditions, we push toward practical phonon devices and new regimes of light–sound

interaction without the strict need for optical cavities.⁶⁸

4.2 From Traveling-Wave to Raman-Like Standing-Wave Modes

4.2.1 Review of Brillouin and Raman Scattering

Brillouin scattering and Raman scattering are two related light-matter interactions that involve inelastic scattering of photons by phonons, but they differ in the nature of the phonons involved. In Brillouin scattering, an incident photon exchanges energy and momentum with a long-wavelength acoustic phonon (a propagating sound wave in the medium). In contrast, Raman scattering typically involves optical phonons or molecular vibrations, which are localized oscillations (e.g., bond vibrations within a molecule or internal lattice vibrations) rather than a continuum acoustic wave. In other words, Brillouin scattering is mediated by traveling acoustic waves in a bulk material, whereas Raman scattering probes standing-wave intramolecular or lattice modes. This fundamental difference is reflected in the frequency scales: acoustic phonons have relatively low frequencies (GHz or below) and are responsible for the small Stokes/anti-Stokes shifts in Brillouin spectra, whereas optical phonons and molecular vibrations have much higher frequencies (THz) yielding the larger shifts seen in Raman spectra (see Figure 1.1).⁶⁹ It is also reflected in momentum conservation conditions: Brillouin scattering requires phase-matching between the optical wave and an acoustic phonon of a particular wavevector, essentially picking out a traveling phonon mode with a definite momentum. Raman scattering, on the other hand, often involves phonons with near-zero wavevector (e.g., zone-center optical modes in crystals or whole-molecule vibrations) due to the selection rule of crystal momentum conservation in perfect lattices.⁷⁰

Despite these distinctions, the line between Brillouin and Raman processes can blur in certain situations. If the medium lacks long-range order or the phonon coherence length is short, the usual momentum-selection rules break down. Shuker and Gammon (1970)⁷¹ showed that in amorphous materials, translational symmetry is lost and essentially all vibrational modes can participate in light scattering. In such cases, even low-frequency acoustic-like modes (normally the realm of Brillouin) become “Raman-active.” This insight explained the observation of broad low-frequency Raman scattering (the so-called boson peak) in glasses by attributing it to acoustic vibrations made allowable by disorder.^{72–79} Conversely, in a small or confined system, the vibrational modes are discrete rather than forming a continuous acoustic band. In effect, they approach the molecular limit where each normal mode can scatter light akin to a Raman transition. Thus, one can view Brillouin and Raman scattering as two limits of the same fundamental interaction, distinguished by whether the phonons act as continuous waves or as localized normal modes.

Spatial confinement of acoustic waves can convert the Brillouin regime into a Raman-like regime. In

an unbounded or large medium, acoustic phonons exist over a continuum of frequencies and wavevectors (a traveling-wave picture). But if the medium is bounded (e.g., a micron-scale particle or a cavity of finite length) the acoustic field must satisfy boundary conditions, leading to a set of allowed eigenmodes. Classic elasticity theory by Lamb (1882)⁸⁰ provided the first analysis of this: a homogeneous elastic sphere supports only certain quantized vibration modes (classified into spheroidal and torsional families) dictated by the sphere's finite size and free-surface boundary condition. These quantized vibration modes are true standing-wave modes confined to the sphere. Subsequent work extended Lamb's theory to include various effects such as surface tension and clamping for small particles, but the essential result is that a finite object has discrete acoustic eigenmodes. Experimentally, Duval et al. (1986)⁸¹ performed a notable demonstration by observing very-low-frequency Raman scattering from nanometer-sized microcrystals embedded in glass. The Raman spectra showed distinct peaks whose frequencies scaled inversely with the particle diameter, exactly as expected for Lamb's vibrational modes in a sphere. Duval identified these peaks as the confined acoustic eigenmodes ("particle vibrational modes") of the microcrystallites, which had become Raman-active. This exemplified how a Brillouin-like acoustic wave (here, a sphere's breathing or shear wave) can become Raman-like when spatially confined. When an acoustic phonon is restricted by boundaries, it is no longer a freely propagating wave but rather a normal mode with a discrete frequency, effectively turning a Brillouin interaction into a Raman-style interaction with a set of allowed modes.

Figure 4.1 offers a conceptual illustration of the transition from a traveling acoustic wave to standing-wave vibrational modes. In a bulk material (left), light scatters from a continuum of acoustic waves (Brillouin scattering), whereas in a confined medium (right), only discrete phonon modes are allowed, producing Raman-like spectral lines. Spatial confinement and acoustic reflections thus shift the scattering from the Brillouin regime toward a Raman-like regime. Contemporary research in cavity optomechanics and related fields has leveraged this wave-to-mode transition as well. For instance, Renninger et al. (2018)⁸² showed that by shaping the geometry of a cm-scale crystal, one can support long-lived acoustic standing-waves even in a bulk solid. At low temperature, the phonon coherence length in their system exceeded the system size, and the crystal effectively behaved as a giant "phonon cavity" with high-Q (quality) acoustic modes.^{82,83} These modes were accessed via Brillouin interactions, blurring the line between traditional Brillouin and Raman: the process was Brillouin in origin (photoelastic coupling to sound waves) but the phonons were in discrete cavity modes like Raman vibrations. These studies underscore that confined acoustic phonons can take on the character of Raman modes.

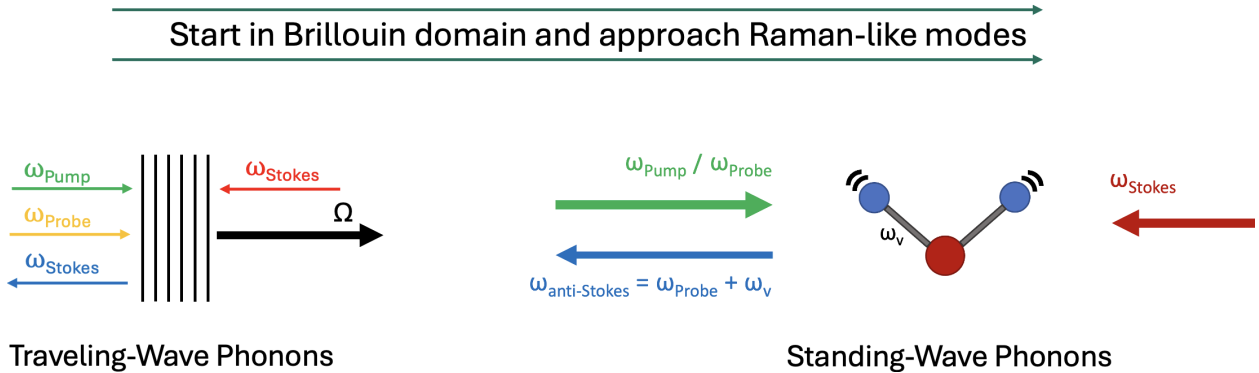


Figure 4.1: Conceptual illustration of the transition from a traveling acoustic wave to standing-wave vibrational modes. In a bulk material (left), light scatters from a continuum of (traveling) acoustic waves (Brillouin scattering), whereas in the molecular vibrations of atomic bonds (right), only discrete (standing-wave) phonon modes are allowed. The left diagram is a conceptual visualization of the Coherently stimulated Brillouin Spectrometer (CoBS) process for a longitudinally-traveling phonon Ω while the right diagram gives a conceptual visualization of an analogous Coherently stimulated Anti-Stokes Raman Scattering (CARS) process with the standing-vibrations ω_v among bonded atoms in a molecule.

4.2.2 Brillouin-Induced Raman Modes

In a traditional SBS experiment, a pump laser drives an acoustic wave through electrostriction, and the scattered Stokes light is down-shifted by the acoustic frequency f_B , given by³

$$f_B = \frac{2v_s n}{\lambda}, \quad (4.1)$$

where v_s is the longitudinal sound speed, n is the refractive index, and λ is the optical frequency. In an unbounded or long medium, the frequency response of the scattered light is determined by material properties (sound speed and optical dispersion) and the acoustic wave can be thought of as a traveling grating moving through the medium. If the medium is shortened such that the acoustic wave can reflect off the sample boundaries, the traveling acoustic wave can auto-interfere with itself to form a standing-wave pattern in the medium. Under these system conditions, a phonon induced by SBS will propagate to the sample end, reflect (assuming a high acoustic impedance mismatch at the boundary), and traverse the medium in the reverse direction. If the length L between acoustic interfaces is a half-integer number of acoustic wavelengths, the forward and backward phonon waves can interfere to form a standing wave pattern (i.e., a resonance), in essence trapping the traveling phonon in the cavity defined by the sample. This standing wave in turn acts like a stable grating, enhancing the scattering of light at well-defined frequencies corresponding to its resonances. We term these resonant phonon excitations “Brillouin-induced Raman modes” to reflect their hybrid character.

In more concrete terms, the finite-length system behaves like an acoustic Fabry-Pérot cavity. For a longitudinal acoustic mode, the condition for a standing wave is that an integer number n of half-wavelengths equals the round-trip length: $n \cdot (\lambda_s/2) = L$. Equivalently, the allowed acoustic frequencies are

$$f_n = \frac{n v_s}{2L}, \quad (4.2)$$

where v_s is the sound velocity in the medium and $n = 1, 2, 3, \dots$ indexes the mode order. The lowest-frequency mode ($n = 1$) has a fundamental frequency $f_1 \approx v_s/(2L)$, and higher modes are integer multiples of this fundamental (assuming a simple one-dimensional confinement). Thus, instead of a single Brillouin shift f_B , one expects a ladder of equally spaced phonon modes in the scattering spectrum, resembling a Raman vibrational progression. The spacing Δf between adjacent modes is approximately $\Delta f \approx v_s/(2L)$, set solely by the cavity length and sound speed. Figure 4.2 illustrates why this is so. For example, if $L = 10$ mm in a medium where $v_s = 5000$ m s $^{-1}$, the fundamental mode would be $f_1 \sim 250$ kHz and overtones at 500 kHz, 750 kHz, etc. In principle, a sufficiently short and high-Q acoustic cavity could produce a comb of multiple GHz-range lines (analogous to molecular vibrational Raman lines) out of what would ordinarily be a single broad Brillouin gain peak.

These Brillouin-induced modes would manifest as distinct peaks in the spectrum of the scattered light. In addition to the usual broadened Brillouin spectrum (with width given by acoustic damping), one would see a series of sharp lines at f_1, f_2, f_3, \dots around the center scattered frequency. Such a spectrum would be clear evidence that the phonon field is not only a freely propagating wave but also oscillating in discrete standing patterns (i.e., an optically driven acoustic resonator within the material). This is conceptually similar to stimulated Raman scattering in a molecule, where one can get a cascade of Stokes lines corresponding to $1\hbar\omega_{\text{vib}}, 2\hbar\omega_{\text{vib}}, 3\hbar\omega_{\text{vib}}$ energy shifts if the pump is intense. Here the “molecular vibration” is replaced by an acoustic cavity mode. If the pump power is high enough to drive the acoustic mode into the nonlinear regime, one might even observe multiple orders of Stokes (and anti-Stokes) as the phonon population builds up in those modes.

The idea of SBS-driven acoustic modes has parallels in prior work. In the cryogenic experiment of Renninger et al. mentioned earlier,⁸² a bulk acoustic mode was driven via Brillouin scattering in a cm-scale quartz crystal. At low temperatures, they observed ultra-narrow acoustic resonances (indicative of discrete modes) in place of a broad Brillouin response, confirming that acoustic coherence across the entire sample can indeed produce a modal spectrum. In our case, we seek to do this at room temperature by engineering a shorter effective acoustic cavity. We aim to accomplish this by taking advantage of our Coherently Stimulated

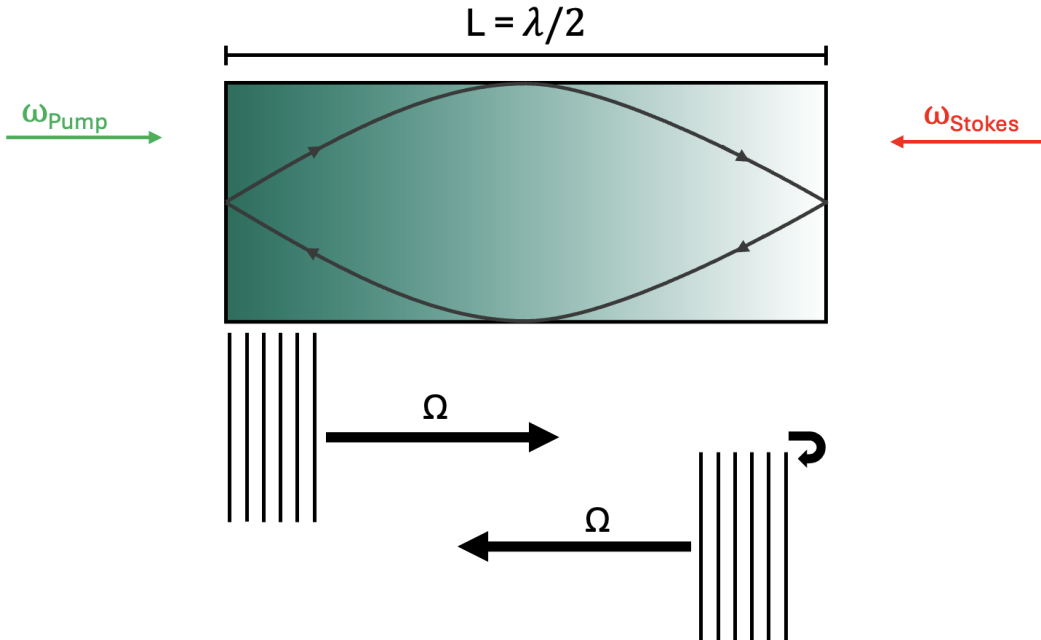


Figure 4.2: Illustration showing how geometry and sound speed of the material determine the allowed acoustic frequencies, given by Equation 4.2. Traveling-wave phonons around the material's Brillouin frequency shift f_B are transduced within the medium via the CoBS process. These phonons traverse the length to reach the boundary, where a high acoustic impedance mismatch causes them to reflect at the interface and retraverse the length of the medium in the reverse direction. The spatio-temporal overlap of counterpropagating traveling-wave phonons causes them to interfere, creating an acoustic standing-wave pattern within the material at discrete frequencies determined by the length and sound speed of the material. Shown in the illustration is the half-wavelength fundamental ($n = 1$) mode, however in general, harmonics near the material's mechanical resonance frequency f_B would be excited in the medium.

Brillouin Spectrometer (CoBS), which offers $\sim 10^6$ improvement in scattered power for $\sim \text{cm}$ lengths over traditional SBS (see Appendix B.2 for a comparison of scattered power across Brillouin techniques, and specifically Figure B.1 for a comparison by effective length L).

4.2.3 Key Parameters and Feasibility

Observing Raman-like standing-wave modes via SBS hinges on several key parameters of the system. We identify three especially critical factors: (1) the scattered power, determined by the effective material Brillouin gain and length as well as the optical powers; (2) the acoustic dissipation in the medium, which limits the mean phonon travel distance; and (3) the acoustic boundary reflectivity, determined by impedance mismatch at interfaces, which enables the phonons to reflect and form standing-waves. These parameters together determine whether the phonon will remain a distributed traveling excitation or collapse (blur) into discrete modes. Chapter 3 describes the CoBS instrument, showing that the scattered power as a result of

the CoBS process is given by Equation 3.1, stated here again as

$$P_{\text{Signal}} = \frac{1}{4}(G_B L)^2 P_{\text{Pump}} P_{\text{Stokes}} P_{\text{Probe}} \Phi, \quad (4.3)$$

where G_B is the material-dependent effective (acousto-optic overlap-adjusted) Brillouin gain factor given by Equation 3.2, L is the effective length, P_i are the optical powers of the pump, Stokes, and probe waves, respectively, and $0 < \Phi < 1$ is a phase-matching relaxation term (given by Equation 3.5) that captures the pump-probe detuning on which the instrument relies. A material's Brillouin gain coefficient g_0 (W m^{-1}), or overlap-adjusted effective gain G_B ($\text{W}^{-1} \text{m}^{-1}$), sets how strongly the phonons are driven for given pump P_P , Stokes P_S , and probe P_{Pr} optical powers over an interaction length L in the CoBS process (see Chapter 3, and specifically Equation 3.1), given here again by

$$G_B = \frac{g_0}{A_{\text{eff}}} \frac{\left(\frac{\Gamma_B}{2}\right)^2}{(\Omega - \Omega_B)^2 + \left(\frac{\Gamma_B}{2}\right)^2}. \quad (4.4)$$

Here, Γ_B is the angular Brillouin linewidth, Ω (Ω_B) is the (resonant) angular acoustic frequency, A_{eff} is the effective area (acousto-optic mode overlap), and g_0 is the Brillouin gain coefficient given by

$$g_0 = \frac{\gamma_e^2 \omega^2}{n v_s c^3 \rho_0 \Gamma_B}, \quad (4.5)$$

where γ_e is the electrostrictive constant, ω is the angular optical frequency, n is the refractive index, v_s is the speed of sound in the material, c is the speed of light, and ρ_0 is the mean density of the material. Short samples demand very high effective Brillouin gain to achieve significant scattered power in a small L . Certain tellurium-based materials, for instance, can offer gains orders of magnitude higher than silica,^{17,84} allowing measurable scattered power in sub-mm cavities. Figure 4.3 shows a graphic which summarizes key gain parameters for the materials investigated in this study.

Even if phonons are driven strongly, they must live long enough (i.e., have a low enough dissipation rate, or high enough acoustic Q) to form a standing wave. At room temperature, intrinsic damping can limit phonon Q_s to $\sim 10^3$ – 10^4 in many solids,^{95,96} implying attenuation lengths of mm to cm for GHz frequencies. Ideally, the sample length L should be comparable to or less than half the attenuation length so that phonons undergo multiple round trips. This is considerably more difficult at room temperature than at cryogenic temperatures, where Q_s can exceed 10^7 .^{82,97} Finally, the phonon must reflect rather than escape at the

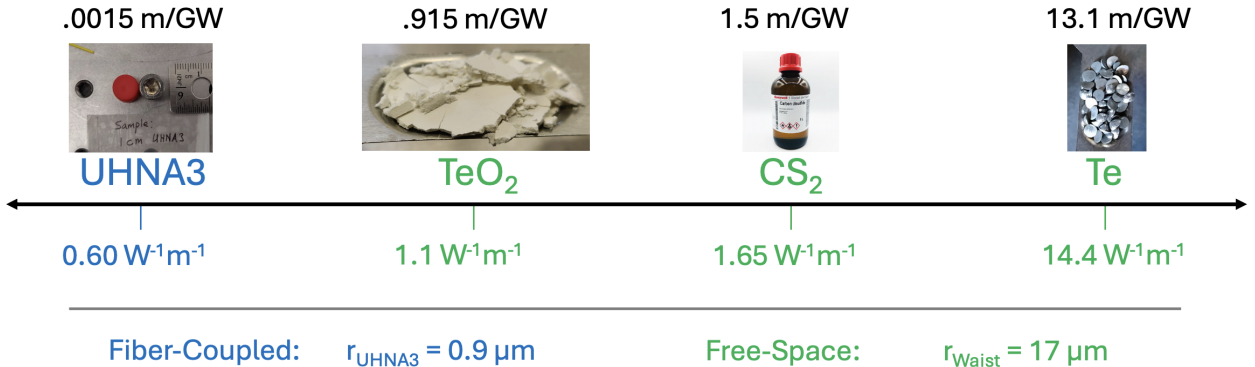


Figure 4.3: Brillouin gain (g_0 , m GW^{-1}) and acousto-optic overlap-adjusted Brillouin gain ($G_B = \frac{g_0}{A_{\text{eff}}^{\text{ao}}}$, $\text{W}^{-1}\text{m}^{-1}$) of the materials investigated in this study. While the material gain (top row text) of Ultra High Numerical Aperture 3 (UHNA3) fiber is 10^3 lower than the other materials, the effective area is confined tightly within its $0.9\text{ }\mu\text{m}$ radius core, greatly improving the acousto-optic response for given length and optical power. The lenses of our free-space optical setup offer comparatively less tight confinement of the light, with the beam waist having radius $r_{\text{Waist}} = 17\text{ }\mu\text{m}$ (bottom row text). The effective gain (middle row text) is ultimately the important gain parameter, as it accounts for both the material gain and the area over which light and sound interact (see Equations 4.4 and 4.5).^{1,13,54,82,85–94}

boundaries. A large acoustic impedance mismatch (e.g., a free surface with air on one side) can approach nearly 100% reflection.^{67,98} Designing the sample with two opposing highly acoustically reflective boundaries is essential to generating a Raman-like standing-wave mode in the medium. In practice, however, partial reflections at each (or even just one) end may suffice so long as the net round-trip reflectivity is high enough to sustain a mode.

In short, we want to create a high- Q acoustic resonator inside a Brillouin-active medium at room temperature: strong enough acousto-optic driving to excite the phonons, low enough damping to maintain them, and robust boundary reflections to confine them. Meeting all of these conditions can be challenging. However, the high ($\sim 5\text{ fW}$) sensitivity and unique short path length advantage of our CoBS instrument (described in Chapter 3 and Section B.2) sparks new motivation, as it provides a new technique tailored for observing small-scale scattering phenomenon. Feasibility estimates and initial CoBS measurements indicate that by utilizing ultra-high-gain media such as Te^{17,84} or liquid CS_2 ³, and ensuring at least one boundary is acoustically reflective, one can push toward Brillouin-induced Raman modes even under ambient conditions.

The sensitivity of our instrument, representing the minimum scattered power that may be detected, has been measured at $P_{\text{Signal}} \approx 5\text{ fW}$ (see Section 3.5.1, and specifically Table 3.1 together with Equation 3.1 and Figure 3.3 for validation of this claim). Using this sensitivity value for P_{Signal} we can rearrange Equation 4.3 to solve for the minimum length L we can expect to observe scattering within for given optical powers, material gain, and pump-probe detuning:

$$L = \frac{2}{G_B} \sqrt{\frac{P_{\text{Signal}}}{P_{\text{Pump}} P_{\text{Stokes}} P_{\text{Probe}} \Phi}}, \quad (4.6)$$

where $0 < \Phi < 1$ and increases for smaller L . For $P_{\text{Signal}} \approx 5 \text{ fW}$ sensitivity and maximum optical powers $P_{\text{Pump}} P_{\text{Stokes}} P_{\text{Probe}} = 0.25 \text{ W}^3$ under typical conditions, Equation 4.6 predicts, for example, the ability to observe scattering within $\sim 500 \text{ nm}$ of UHNA3 fiber ($G_{B, \text{UHNA3}} = 0.6 \text{ W}^{-1} \text{ m}^{-1}$). Equation 4.6 makes clear that minimizing the observable scattering length is accomplished by any of: bumping optical powers, improving instrument sensitivity, or choosing a higher gain scattering medium.

In what follows, we detail the experimental platforms and theoretical modeling that guided our attempts to observe discrete phonon modes in high-gain materials. Although a conclusive demonstration proved elusive, the conceptual framework is robust and provides a foundation for ongoing efforts. By shrinking the acoustic path length, maximizing phonon reflectivity, and exploiting strong CoBS gain, one can approach the regime where traveling-wave Brillouin scattering morphs into Raman-like standing-wave modes. This pursuit effectively unifies the traveling-wave and standing-wave paradigms of light-sound interaction, providing new opportunities in cavity-free phononics, resonant optomechanics, and coherent phonon devices at room temperature.

4.3 Results

In this section we detail results and progress toward measuring Brillouin-induced Raman modes, in chronological order of investigation. The overall approach was to start deep in the continuous Brillouin domain of longitudinally-traveling phonons in bulk material and steadily approach the discrete Raman domain by measuring incrementally shorter lengths of materials well-suited to the task. This investigative study began with user-friendly fiber-coupled lengths of UHNA3 fiber, progressed quickly to increasingly challenging free-space measurements of challenging materials such as liquid CS_2 and thin films of TeO_2 and Te , and ultimately arrived at fiber-to-chip coupling into specialized suspended waveguides. We present here both the successes along the way as well key insights gained from setbacks, with special focus on illuminating the reasoning behind critical pivots in our investigation.

4.3.1 Ge-Doped Optical Fiber

To begin with a clear measurement firmly in the Brillouin domain, we target (short) lengths of the well-understood UHNA3 fiber.⁵⁴ UHNA3 features a Brillouin frequency shift distinct from the single mode

fiber 28 (SMF-28) of the apparatus ($f_{B,\text{UHNA3}} = 9.18 \text{ GHz}$ vs $f_{B,\text{SMF28}} = 10.85 \text{ GHz}$), making it easily distinguishable from instrument background. Additionally, its small core and high Ge concentration ($\sim 44 \text{ wt.\%}$) make for tight acousto-optic overlap ($A_{\text{eff}}^{\text{ao}}$) and good guidance of both light and sound, respectively. Figure 4.3 shows the key gain figures for UHNA3. While its material gain ($g_0 = 0.0015 \text{ m GW}^{-1}$) is low, the acousto-optically adjusted effective Brillouin gain ($G_B = \frac{g_0}{A_{\text{eff}}^{\text{ao}}} = 0.60 \text{ W}^{-1} \text{ m}^{-1}$) is sufficiently high to allow a measurement in sub-mm lengths for typical optical powers (Equation 4.6).

Figure 4.5 shows pictures of measured 1 cm and 1 mm lengths of UHNA3 fiber (Figures 4.4a and 4.4b, respectively) spliced into the SMF-28 of the sample stage of the CoBS apparatus. Figure 4.5a shows the observed spectra for this 1 cm segments of UHNA3 captured at maximum available optical powers $P_P P_S P_{Pr} \sim 0.25 \text{ W}^3$. The peak spectral amplitude has been normalized to unity and spectral density is expressed in Arbitrary Units for clean presentation, a standard practice which acknowledges the arbitrary nature of the optical-to-electrical conversion unique to each photodiode detector. 1σ uncertainties are smaller than the data point markers. Figure 4.5a showcases a measurement taken more recently, after orders of magnitude sensitivity and performance improvements to the CoBS instrument, however the measurement gathered initially also represented a strong successful measurement of 1 cm UHNA3, prompting an advance to attempting a measurement of 1 mm UHNA3.

This measurement is shown in Figure 4.5b, which features slight Fano asymmetry in lineshape indicative of signal-background interference in a low-signal regime (see Section B.3 in Appendix B). Unlike Figure 4.5a, which was recaptured recently, after orders-of-magnitude sensitivity and performance improvements to the CoBS instrument, the spectra shown in Figure 4.5b dates to the time of its relevance to this investigation. The slight Fano asymmetry indicates that this measurement, while very clear and of high SNR, was captured from a signal which was near the order of the background continuum, placing the measurement not far from the sensitivity limit of the instrument at the time. Nonetheless, Figure 4.5b represents a clear successful measurement of 1 mm UHNA3 fiber, prompting a continuation on the path to shorter lengths and Brillouin-induced Raman modes.

4.3.2 Free-Space Optics with Liquid CS₂

Having successfully measured the shortest practical lengths of optical fiber reasonably fabricatable, a regime change to free-space optics in the sample stage was required to continue our investigation. To smooth this transition, we first targeted meaningful lengths of the high-gain liquid CS₂. From Figure 4.3, CS₂ has a material Brillouin gain of $\sim 1.5 \text{ m GW}^{-1}$, which is 10^3 higher than that of UHNA3 fiber, however this material advantage is offset by the much lower acousto-optic mode overlap afforded by the beam waist

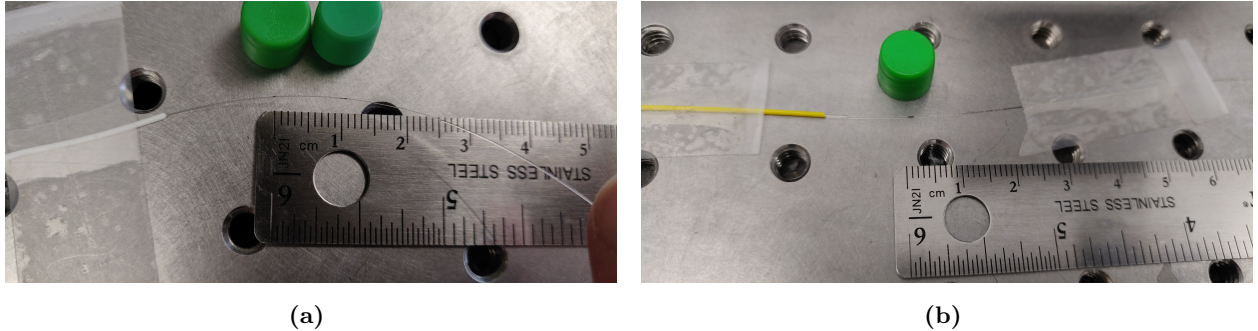


Figure 4.4: Photographs of (a) 1 cm and (b) 1 mm lengths of UHNA3 fiber, marked by black sharpie markings and spliced into the SMF-28 of the CoBS instrument. Samples were fabricated by first splicing a longer segment of UHNA3 to SMF-28 and marking the splice location such that the UHNA3 could subsequently be cleaved to the appropriate length as measured from the marking of the first splice.

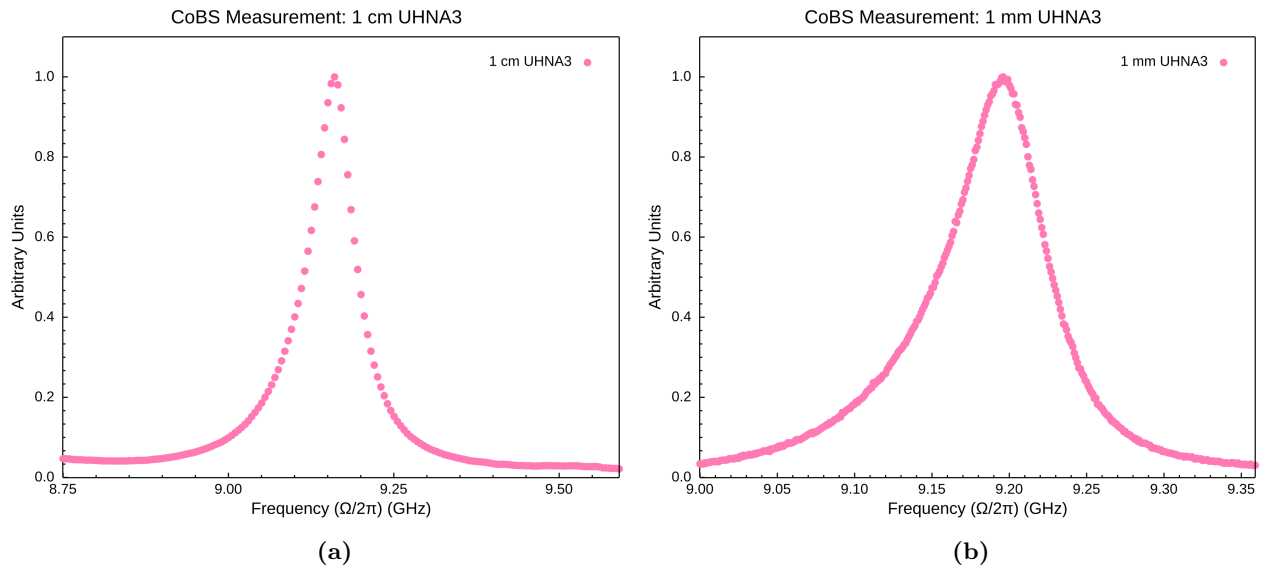
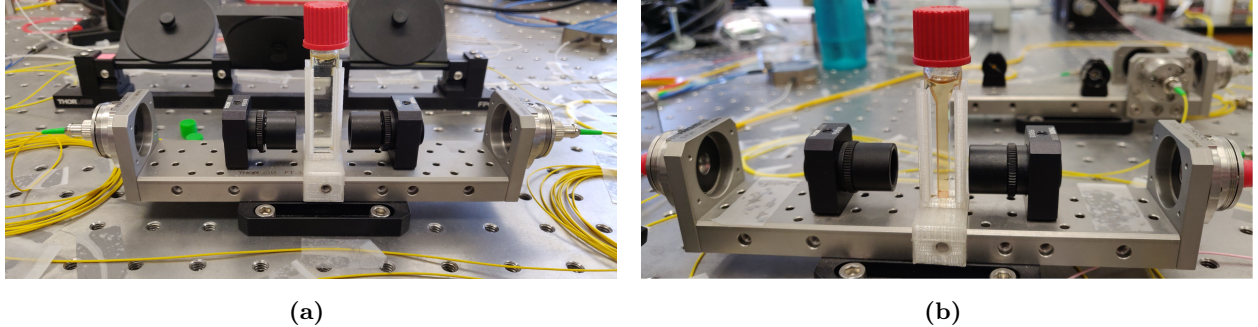


Figure 4.5: (a) Observed background-subtracted spectrum obtained through a CoBS measurement of 1 cm of UHNA3 fiber (pictured in Figure 4.4a) captured at maximum operating optical powers $P_p P_s P_{pr} \sim 0.25 \text{ W}^3$, with 1σ uncertainties smaller than the data point markers. (b) Observed background-subtracted spectrum obtained through a CoBS measurement of 1 mm of UHNA3 fiber (pictured in Figure 4.4b), with 1σ uncertainties smaller than the data point markers. The spectrum shows strong Fano asymmetry (see Section B.3 in Appendix B), indicating interference of a weak signal with the broad background continuum. This is an older measurement, taken prior to orders of magnitude sensitivity improvements, and the Fano effects seen here indicate this was near the sensitivity limit of the instrument at the time.

produced by our lenses ($A_{\text{eff, Free-Space}}^{\text{ao}} = \pi(17 \mu\text{m})^2$ vs $A_{\text{eff, UHNA3}}^{\text{ao}} = \pi(0.9 \mu\text{m})^2$). The resulting effective Brillouin gain of liquid CS_2 in the free-space optical setup of our CoBS instrument is $G_B = \sim 1.65 \text{ W}^{-1} \text{ m}^{-1}$, nearly a factor of 3 greater than that of UHNA3. This combined with an initially targeted length $L = 1 \text{ cm}$ provided a sufficiently large target to make for a gentle transition from a fiber-coupled to free-space regime.

Figure 4.6 shows photographs of a 1 cm-by-4 mm path length cuvet of liquid CS_2 mounted in the sample



(a)

(b)

Figure 4.6: Photographs of (a) 1 cm and (b) 4 mm lengths of liquid CS₂ in the beam path of the CoBS instrument. The single 1 cm-by-4 mm path length cuvet allowed for both measurements shown in Figure 4.7 via 90° rotation within its mount.

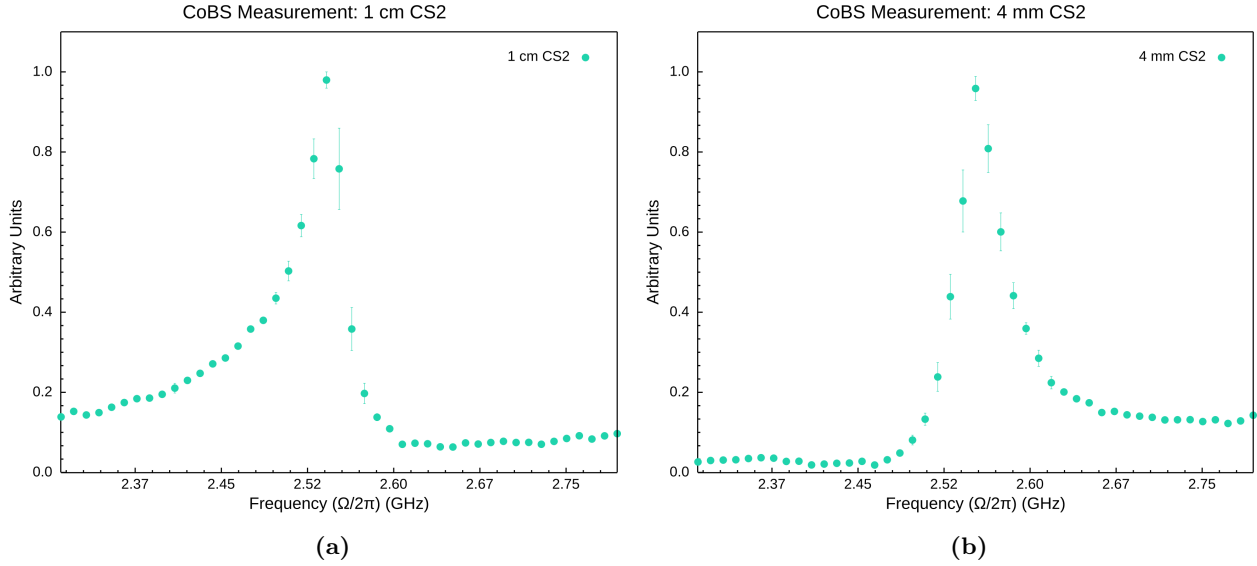


Figure 4.7: (a) Observed background-subtracted spectrum obtained through a CoBS measurement of 1 cm of liquid CS₂ (pictured in Figure 4.6a), with 1σ uncertainties smaller than the data point markers. The spectrum shows strong Fano asymmetry (see Section B.3 in Appendix B), indicating interference of a weak signal with the broad background continuum. This is an older measurement, taken prior to orders of magnitude sensitivity improvements, and the Fano effects seen here indicate this was near the sensitivity limit of the instrument at the time. (b) Observed background-subtracted spectrum obtained through a CoBS measurement of 4 mm of liquid CS₂ (pictured in Figure 4.6b), with 1σ uncertainties smaller than the data point markers. This is an older measurement, taken prior to orders of magnitude sensitivity improvements, and the Fano effects seen here indicate this was near the sensitivity limit of the instrument at the date of this measurement.

stage between two lenses. Light is guided from the fiber of the apparatus into free space, collimated and focused by the fiber ports on either side of the fiber bench, upon which the sample sits, and the diffraction-limited lenses. Figure 4.6a shows the cuvet placed in the 1 cm path length configuration while Figure 4.6b shows it rotated 90° for the 4 mm path length configuration.

Figure 4.7 shows the observed spectra from CoBS measurements of 1 cm and 4 mm liquid CS₂, pictured in Figure 4.6. Both measurements showcase significant Fano asymmetry, again indicative of signal-background interference in a low-signal regime (see Section B.3 in Appendix B). The strong Fano interference in both measurements emphasizes the proximity to the sensitivity limit of the CoBS instrument at the time these spectra were observed. Each progression to lower-signal (less scattered power P_{CoBS} , from Equation 4.3) represents iterative sensitivity and performance improvements to the CoBS instrument, ranging from insights about the importance of well-cleaned and polished pigtail ends throughout the apparatus to operating setting discoveries such as setting both the pump and probe lasers to “whisper” instead of “dither” mode, as well as component upgrades such as the detector and higher power Erbium-Doped Fiber Amplifier (EDFA)s (see Chapter 3 for more details on the CoBS instrument and its performance optimization).

With the free-space functionality demonstrated with the successful measurement of 1 cm and 4 mm bulk liquid CS₂ in a cuvet, all basic experimental infrastructure was in place to pursue Brillouin-induced Raman modes in much shorter length samples. The newly-achieved $\sim 10 \text{ fW}$ sensitivity limit of the instrument around this time, experimentally-obtained from reduced power measurements of 1 cm UHNA3 fiber, supported the feasibility of measuring scattering in far shorter interaction lengths. With this in mind, we made the ambitious leap to thin films.

4.3.3 TeO₂ Thin Film

Table 4.1 presents key values for material properties of TeO₂ (both crystalline and amorphous thin film) relevant to observing Brillouin-induced Raman modes. To observe Raman-like modes in a confined medium, we must be able to sufficiently excite traveling-wave phonons via the CoBS process in an effective length equal to at most half the mean travel distance of the phonons in that material (coherence length L_{coh}). Phonon coherence length is a function of the material’s mechanical dissipation rate, or Brillouin linewidth $\Gamma_B/2\pi$. Setting the effective length at half of the phonon coherence length ensures the phonons make at least one round-trip in the material before dissipating (decohering), representing a critical requirement in observing Brillouin-induced Raman modes. A CoBS scattered power estimate is given (via Equation 4.3) corresponding to half the phonon coherence length of the material. This figure (consistent for $L_{\text{coh}}/2$ and in pW reported units across all similar material property tables presented in this chapter) offers a reference for the minimum sensitivity performance required from the CoBS instrument if Raman modes are to be observed in the material. For example, if Raman modes are to be observed in crystalline TeO₂, the effective length of the sample used to measure them must be at most $L_{\text{eff, sample}} = L_{\text{coh}}/2 = 215 \mu\text{m}$ and CoBS must be capable of 3500 pW sensitivity (which it achieves by $\sim 10^3$). In the table, τ is the phonon lifetime

TeO₂	Γ_B^{82} (MHz)	τ (ns)	$v_{s,\text{long}}^{88-93}$ (m s ⁻¹)	n^{94}	L_{coh} (μm)	$P_{\text{CoBS}, L_{\text{coh}}/2}$ (pW)	Ω_B (GHz)	$\Omega_{R, 1 \mu\text{m}}$ (GHz)
Crystal	$2\pi \cdot 10$	100	4260	2.2	430	$\sim 3.5 \times 10^3$	$2\pi \cdot 12.1$	$2\pi \cdot 2.13$
Thin Film	$2\pi \cdot 50 \pm 10$	20	~ 4150	2.27	83	~ 137	$2\pi \cdot 12.2$	$2\pi \cdot 2.08$

Table 4.1: Material parameters for TeO₂ relevant to observing Brillouin traveling-wave modes and Raman standing-wave modes. The first row gives values for crystalline TeO₂^{82,94}, while the second row reports measured values of our 1 μm TeO₂ thin film obtained from Figures 4.9 and 4.10. Here, Γ_B is the angular Brillouin linewidth (phonon dissipation rate) and the inverse of phonon lifetime ($\tau = (2\pi \cdot \Gamma_B)^{-1}$), $v_{s,\text{long}}$ is the longitudinal sound speed, and n is the refractive index. We take the refractive index for an amorphous thin film of TeO₂ as the average of the crystalline-TeO₂ ordinary ($n(o) = 2.2$) and extraordinary ($n(e) = 2.34$) refractive indices ($n_{\text{avg}} \approx 2.27$), giving an expectedly reduced longitudinal sound speed $v_{s,\text{film}} \approx 4150 \text{ m s}^{-1}$ in the imperfect lattice of the physical vapor deposition (PVD)-deposited film. l_{coh} is the phonon coherence length (mean travel distance), scattered power for a CoBS process (P_{CoBS}), reported here for $L_{\text{coh, crystalline}}/2 = 215 \mu\text{m}$ and $L_{\text{coh, thin film}}/2 = 42.5 \mu\text{m}$ TeO₂, scales with L^2 (Equation 4.3). P_{CoBS} improves slightly in the thin film due to the higher refractive index, but worsens significantly by faster dissipation Γ_B . Finally, Ω_B is the angular Brillouin frequency shift (Equation 4.1), and $\Omega_{R, 1 \mu\text{m}}$ is the first harmonic ($n = 1$) of the fundamental L_0 Raman-like mode for $L = 1 \mu\text{m}$ (Equation 4.2).

$(\tau = (2\pi \cdot \Gamma_B)^{-1})$, $v_{s,\text{long}}$ is the longitudinal sound speed, n is the refractive index, and Ω_B and $\Omega_{R, 1 \mu\text{m}}$ are the Brillouin frequency shift (Equation 4.1) and the first harmonic ($n = 1$) of the fundamental L_0 Raman mode for $L = 1 \mu\text{m}$ (Equation 4.2), respectively. The reported first harmonic Raman mode is also consistent across all material property tables in this chapter as calculated for $L = 1 \mu\text{m}$.

Table 4.1 shows that to measure Brillouin-induced Raman modes in an amorphous thin film of TeO₂, the film may be at most $L_{\text{coh}}/2 \approx 41 \mu\text{m}$ (notably beyond the standard thickness considered to be a “thin film”) and CoBS must be capable of $P_{\text{CoBS}, L_{\text{coh}}/2} \approx 137 \text{ pW}$ sensitivity. This makes clear the viability of TeO₂ as a good material platform for observing discrete Raman modes with the well-suited CoBS instrument. For a typical thin film of 1 μm thickness the required CoBS sensitivity increases to $\sim 76 \text{ fW}$, still within the measured sensitivity limit, with excited phonons making on average ~ 80 round trips within the film before dissipating.

To fabricate TeO₂ thin film samples we collaborated with Dr. John Gibbs’ Nanotechnology Laboratory and its members to perform PVD of controlled films onto glass substrates. TeO₂ powder was initially attempted, via the recommended thermal evaporation method, however the fine TeO₂ powder was observed to ballistically repel from the thermal evaporation boat while still in solid powder form before it had the chance to melt into the liquid phase. To resolve this, we attempted a pretreatment procedure of applying high-compression forces to the TeO₂ powder with a hydraulic press. The resulting compressed plates of

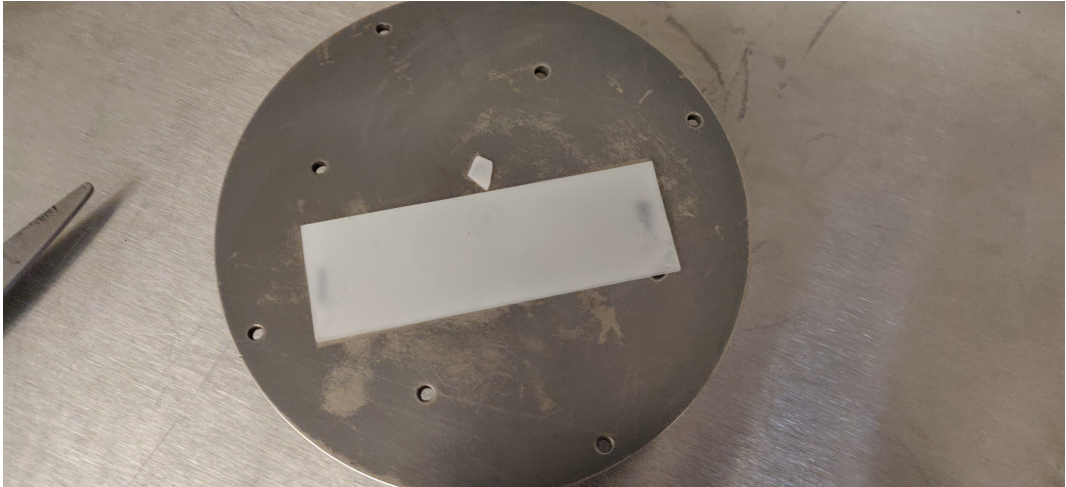


Figure 4.8: Glass slide with a thin film of TeO_2 deposited via PVD.

TeO_2 powder (pictured in Figure 4.3) maintained stability in the thermal boat under vacuum and heating conditions, indicating initial success. However, the tungsten thermal boat twice melted together with the compressed TeO_2 plates, halting the deposition and preventing the completion of the sample.

To surmount this issue, we resolved to deposit Te metal and apply a post-deposition annealing treatment to oxidize the Te into the desired TeO_2 . This fabrication procedure proved successful. Initial deposition rate stability issues were resolved by inserting custom electrical circuit logic into the deposition chamber voltage controls. The circuit logic provided added sensitivity of deposition parameters by introducing a switchable “course” and “fine” voltage control mode, with the fine setting containing the phenomenologically-found sweet-spot of resistance for thermally depositing Te metal. In our experience, thermally depositing μm films of Te metal via multiple successive deposition-annealing cycles of annealable sublayers, occurring over $\sim 20\text{ h}$, and keeping the deposition rate steady with continuous adjustment of the fine-control knob is akin to rolling a ball lengthwise down the outside of a pipe of diameter equal to the ball’s. Nevertheless, this procedure proved a reliable method of producing TeO_2 thin films deposited onto glass slides which could easily be inserted and secured in the beam path of the CoBS instrument. Figure 4.8 shows an image of a glass slide with a deposited thin film of TeO_2 which has been successfully annealed, converting the mirror-shine appearance of the deposited Te into the semi-transparent appearance seen here. This sample is shown reattached to the PVD substrate for additional layers to be deposited and subsequently annealed. The annealer was found to be capable of fully oxidizing a maximum of $\sim 300\text{ nm}$ of deposited Te. This set the step size for building up TeO_2 layers toward the total desired sample thickness.

Figure 4.9 shows a CoBS measurement of a $1\text{ }\mu\text{m}$ thin film of TeO_2 . Initial inspection of this measurement resulted in premature dismissal of a plausible measurement. From reported sound speed and refractive index

CoBS Measurement: 1 μm TeO₂

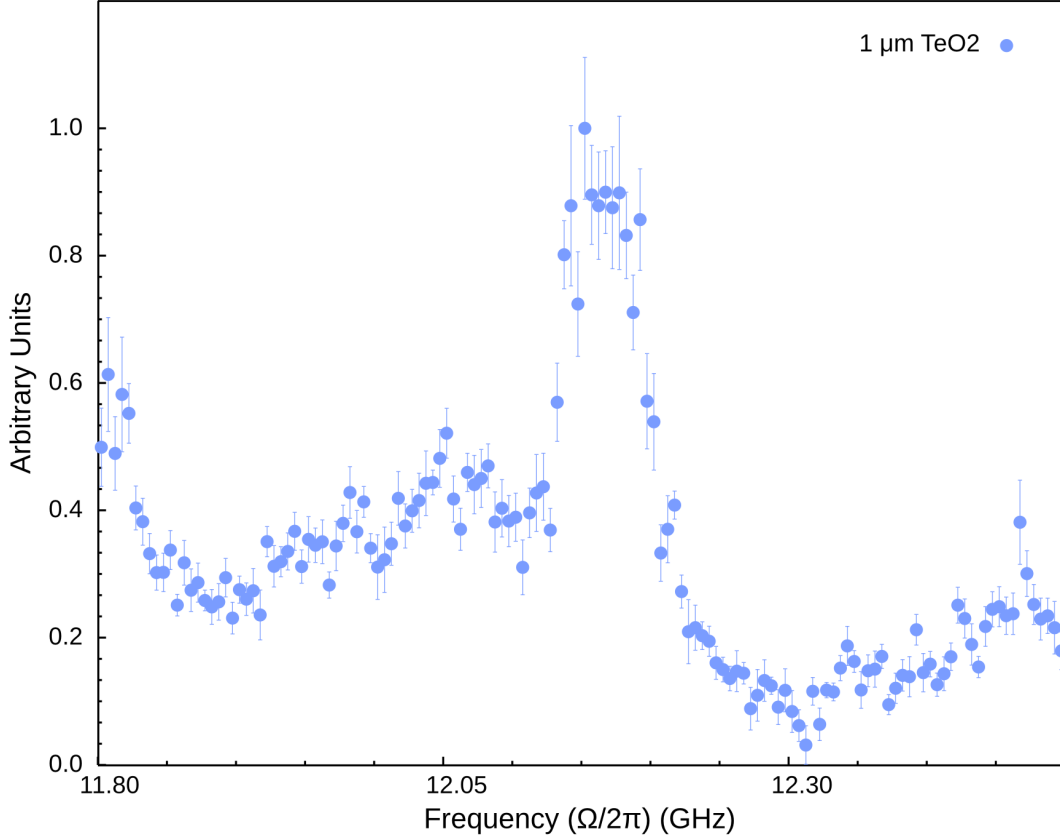
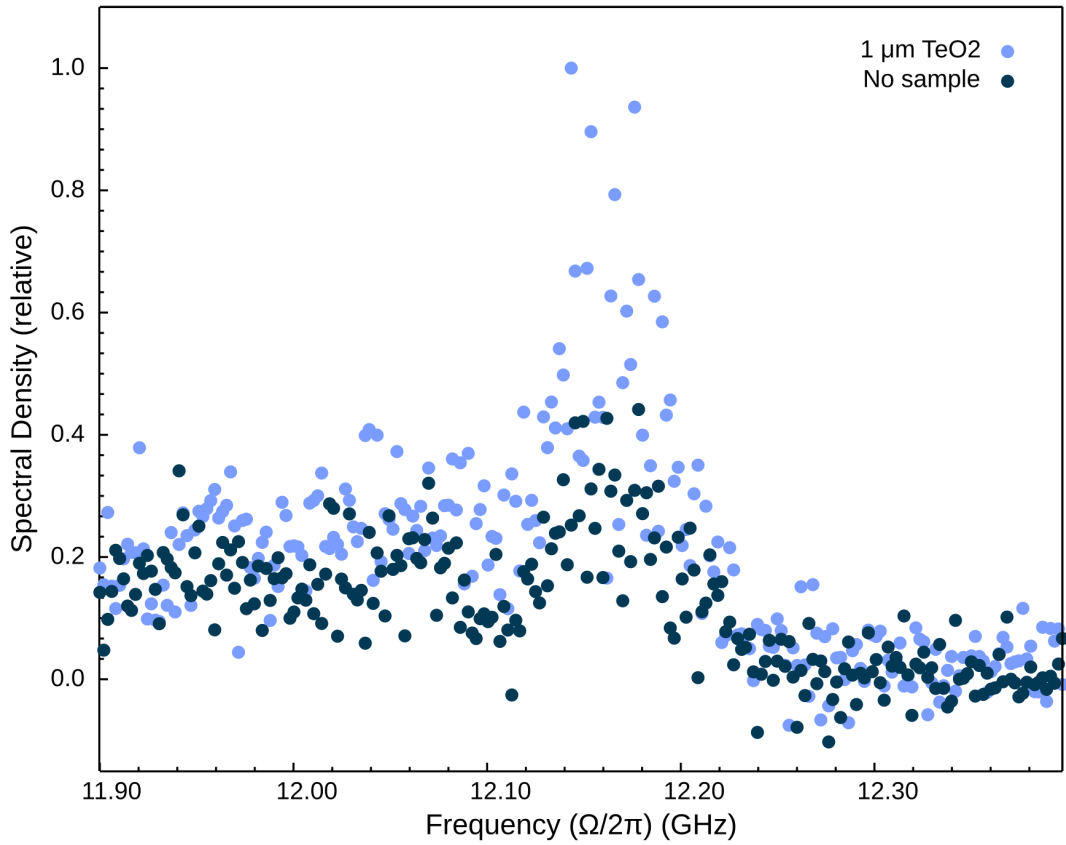


Figure 4.9: Observed background-subtracted spectrum obtained through a CoBS measurement of 1 μm of TeO₂ captured at maximum operating optical powers $P_{\text{P}} P_{\text{S}} P_{\text{Pr}} \sim 0.25 \text{ W}^3$, with 1σ uncertainties.

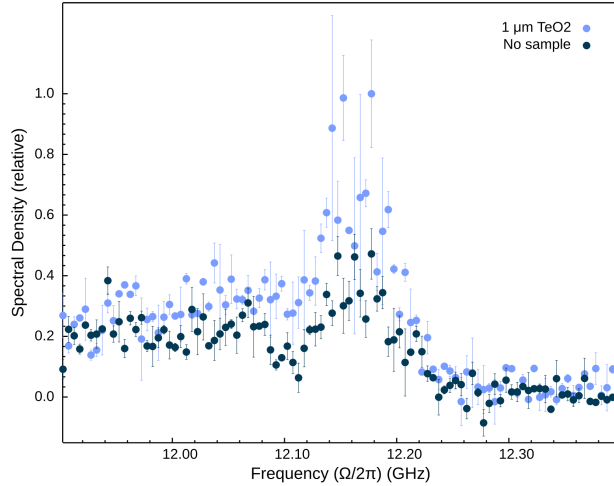
for TeO₂,^{88–94} Equation 4.1 predicts a Brillouin frequency shift for TeO₂ to be $f_{\text{B}} \approx (12.4 \pm 0.5)$ GHz, which is where we see a pronounced feature in the spectra presented in Figure 4.9. An independent measurement was performed on a second similar but independent 1 μm thin film of TeO₂. For this second measurement, after capturing the TeO₂ film spectra, a repeated measurement was immediately performed in which the TeO₂ sample was removed and a measurement was taken under identical parameters. Figure 4.10 shows the result of these two measurements in three variations in resolution via binning: unbinned raw resolution (Figure 4.10a), 5 MHz bins (Figure 4.10b), and 10 MHz bins (Figure 4.10c). In each, a notable ~ 12.16 GHz feature can be seen in the 1 μm TeO₂ spectrum, above the background “No sample” spectrum. Both 1 μm TeO₂ spectra feature a consistent full-width half-max (FWHM) linewidth of ~ 50 MHz. While perfectly crystalline TeO₂ features a smaller linewidth ~ 10 MHz,⁸² dissipation within a rough amorphous thin film of varying grain size and imperfect crystal structure would feature significantly higher dissipation (wider linewidth) than its crystalline counterpart. Additionally, these same imperfections would contribute to a slightly slower sound speed in the deposited TeO₂, explaining the Brillouin frequency shift appearing on

CoBS Measurement: 1 μm TeO₂



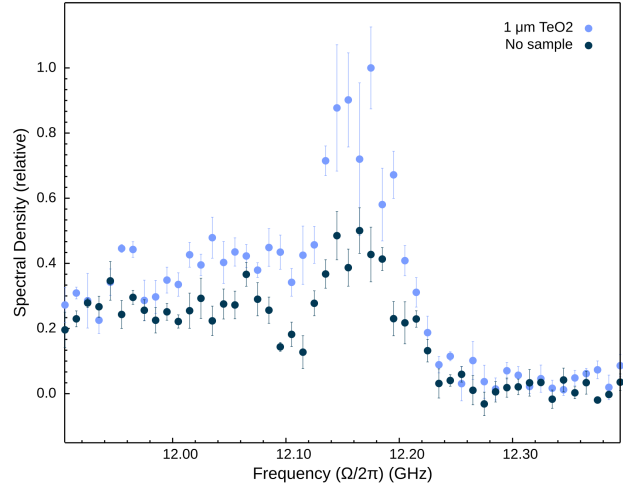
(a) Raw resolution.

CoBS Measurement: 1 μm TeO₂



(b) 5 MHz binning.

CoBS Measurement: 1 μm TeO₂



(c) 10 MHz binning.

Figure 4.10: Observed background-subtracted spectra obtained through a CoBS measurement of 1 μm of TeO₂ captured at maximum operating optical powers $P_{\text{P}}P_{\text{S}}P_{\text{Pr}} \sim 0.25 \text{ W}^3$, with 1σ uncertainties. Each panel shows the same data set under different binning resolutions.

CoBS Measurement: 500 nm TeO₂

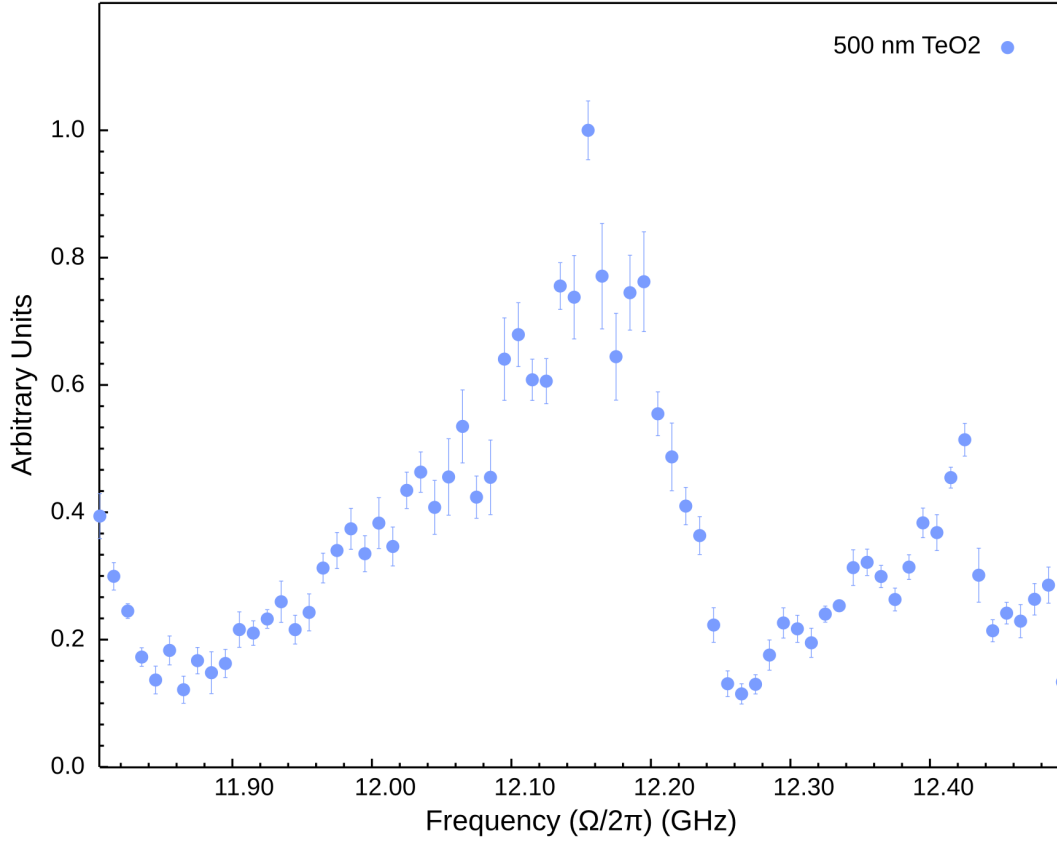


Figure 4.11: Observed background-subtracted spectrum obtained through a CoBS measurement of 500 nm of TeO₂ captured at maximum operating optical powers $P_{\text{P}} P_{\text{S}} P_{\text{Pr}} \sim 0.25 \text{ W}^3$, with 1σ uncertainties.

the lower end of the expected range (see Equation 4.1). As previously noted, a measurement of 1 μm TeO₂ would require at least as great as $\text{sim}76 \text{ fW}$, which is well inside of the capability of the demonstrated $\sim 5 \text{ fW}$ sensitivity of our CoBS instrument. For all these reasons, we conclude plausible success in measurement of a 1 μm thin film of TeO₂, awaiting further measurements to confirm.

Figure 4.11 shows a spectrum obtained for a 500 nm thin film of TeO₂. A pronounced background noise profile dominates the spectrum, with no significant spectral features indicative of a measurement of TeO₂. While the scattered power produced from 500 nm of TeO₂ ($P_{\text{CoBS}, 500 \text{ nm TeO}_2} \approx 19 \text{ fW}$) remains just within the sensitivity limit of the instrument, in practice, a host of non-ideal experimental conditions could prevent the instrument from performing at its full sensitivity limit.

As mentioned, the plausible measurements shown in Figures 4.9 and 4.10 were dismissed initially. In search of other options, and working with Te metal over so many hours of PVD depositions, we began researching the possibility of using un-annealed Te over its oxidized counterpart, mostly due to the tremendously higher material gain factor offered by Te.

4.3.4 Tellurium Thin Film

Table 4.2 gives the relevant parameters for Te metal. While Te is absorptive at $1.55\text{ }\mu\text{m}$, transmission becomes meaningful as films become thinner, with a $1\text{ }\mu\text{m}$ thin film of Te permitting 11.4% of $1.55\text{ }\mu\text{m}$ light to transmit and a 500 nm film permitting 29%.⁹⁹ The $n = 4.58$ refractive index of Te contributes to a massive material Brillouin gain of $g_0 = 13.1\text{ m GW}^{-1}$, translating to an acousto-optic overlap-adjusted effective Brillouin gain $G_B = 14.4\text{ m}^{-1}\text{ W}^{-1}$. Having concluded that no successful measurement for TeO_2 thin films were achieved, this much higher gain of Te presented an apparent opportunity.

Te	$\Gamma_B^{100-104}$ (MHz)	τ (ns)	$v_{s,\text{long}}^{100-105}$ (m s^{-1})	$n^{99,106}$	L_{coh} (μm)	$P_{\text{CoBS}, 500\text{ nm}}$ (pW)	Ω_B (GHz)	$\Omega_{R, 1\text{ }\mu\text{m}}$ (GHz)
Bulk	$\sim 2\pi \cdot 10$	100	~ 2610	4.58	261	$\sim 80 \times 10^{-3}$	$2\pi \cdot 15.4$	$2\pi \cdot 1.31$

Table 4.2: Material parameters for Te relevant to observing Brillouin traveling-wave modes and Raman standing-wave modes, obtained from published values for bulk Te. Here, Γ_B is the angular Brillouin linewidth (phonon dissipation rate) and the inverse of phonon lifetime ($\tau = (2\pi \cdot \Gamma_B)^{-1}$), $v_{s,\text{long}}$ is the longitudinal sound speed, n is the refractive index, l_{coh} is the phonon coherence length (mean travel distance), and P_{CoBS} is the scattered power for the CoBS process, reported here for 500 nm Te, and scales with L^2 (Equation 4.3). Finally, Ω_B is the angular Brillouin frequency shift (Equation 4.1), and $\Omega_{R, 1\text{ }\mu\text{m}}$ is the first harmonic ($n = 1$) of the fundamental L_0 Raman-like mode for $L = 1\text{ }\mu\text{m}$ (Equation 4.2). While CS_2 and TeO_2 are transparent at $1.55\text{ }\mu\text{m}$, Te is absorptive here. However, transmission becomes meaningful through thin films, with $1\text{ }\mu\text{m}$ of deposited Te permitting 11.4% and 500 nm permitting 29% of $1.55\text{ }\mu\text{m}$ light to transmit.⁹⁹ This extra $\sim 70\%$ loss (for each of the three optical fields) has been accounted for in the scattered power value for the CoBS process listed in the table.

Initial CoBS measurements of Te thin films resulted in evident ablation of the film from the glass substrate, with poor adhesion between the Te and glass slide the determined cause. Collaborators at Center for Integrated Nanotechnologies (CINT) lent the insight that a thin adhesion layer of Se is recommended between Te deposited onto glass, and Se-primed sapphire substrate samples were kindly sent to us ready for depositions of Te to be performed ontop of a 10 nm Se layer. The Se adhesion layer proved successful in adhering the Te. A diagram of the material layering is shown in Figure 4.12. A 500 nm thin film of Te was fabricated after estimations of feasible measurement resulted in a required sensitivity $\sim 15 \times$ the sensitivity limit of the instrument. During measurement, it was discovered that the energy of the optical powers incident on the sample (of which $\sim 70\%$ is absorbed) caused significant heating in the thin film of Te, resulting in oxidization of the Te into TeO_2 within the beam spot. Figure 4.13 shows a photograph which captures this resulting oxidized state of the Te thin film after sitting for a measurement in the beam path of the instrument.

With this unfortunate result, we began a broader reanalysis of the choice of platform for observing

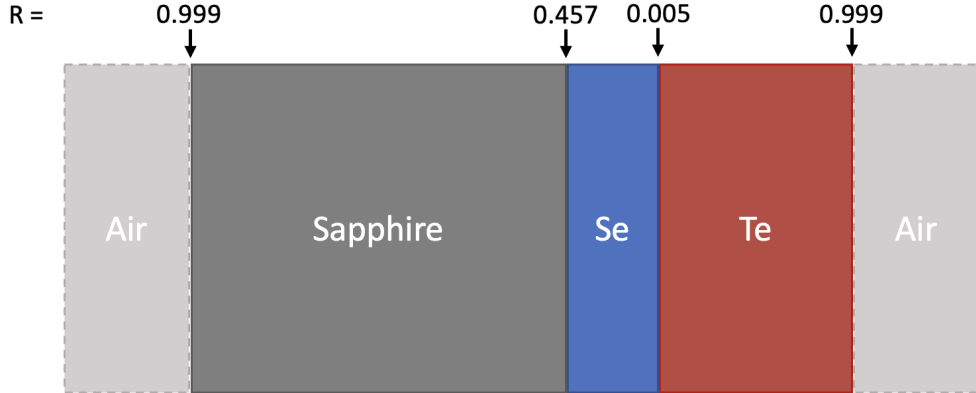


Figure 4.12: Illustration of the material layers of a Te thin film sample. 10 nm Se is deposited by collaborators at CINT to act as an adhesion layer between the sapphire and Te film. Also shown are the acoustic reflectivity values at each interface as a result of acoustic impedance mismatch between materials.



Figure 4.13: Evidence of oxidization of the 500 nm Te thin film in the circular beam spot due to $\sim 70\%$ absorption of the $1.55 \mu\text{m}$ optical fields.

Brillouin-induced Raman modes at room temperature. Figure 4.12 also shows acoustic reflectivity values R for each interface of a Te sample, calculated by the acoustic impedance Z of each material,

$$R = \frac{Z_a - Z_b}{Z_a + Z_b}, \quad (4.7)$$

where Z is the product of the material's density and sound speed. While the Te-air boundary offers near complete acoustic reflection, owing to the large acoustic impedance mismatch between Te and air, the acoustic reflectivity is near zero between Te and Se and only ~ 0.5 between the Se and the sapphire substrate. These values are similar for TeO_2 . To ultimately observe Raman modes, there must be sufficient confinement of the phonons. After some consideration of dissolvable substrates which may be engineered to expose a portion of the Te or TeO_2 to air on both sides, recovering both free bounds, we returned to the last (apparent) successful measurement: CS_2 .

4.3.5 Carbon Disulfide Micrometer Cell

Table 4.3 gives the relevant material parameters for achieving Brillouin-induced Raman modes in CS_2 . Notably, the phonon dissipation rate within CS_2 is nearly 10^1 greater than that of TeO_2 or Te , at $\Gamma_B = (90 \pm 10) \text{ MHz}$. This in combination with its slower speed of sound $V_s = 1150 \text{ m s}^{-1}$ results in a short phonon coherence length $L_{\text{coh}} = (13 \pm 2) \mu\text{m}$ and a correspondingly high sensitivity requirement of $P_{\text{CoBS}, 6.5 \mu\text{m}} \approx 7.2 \text{ pW}$. While this is smaller than the half-coherent-length sensitivity required for TeO_2 , making for a harder measurement to observe Raman modes in CS_2 than TeO_2 by this metric, the reduced complexity of the CS_2 experimental platform as compared to the amorphous thin films presented as attractive. Additionally, the air- CS_2 -air boundaries represent near total acoustic confinement at the interfaces, and the narrower Raman mode spacing (multiples of $f_{R, \text{CS}_2} = 575 \text{ MHz}$, as opposed to $f_{R, \text{TeO}_2} = 2.13 \text{ GHz}$) in combination with the wider linewidth of CS_2 together offered the possibility of more achievable length-tuning for Raman mode placement near the Brillouin frequency shift.

Small path length cells were obtained for 1 mm, 100 μm , and 10 μm path lengths. Figure 4.14 show photographs of each of these cells installed into the sample holder of the sample stage of CoBS. Progressive measurements were attempted, with each $10\times$ decrease in effective length L corresponding to a $100\times$ decrease in scattered power produced, and thereby a $100\times$ higher sensitivity required for a successful measurement (see Equation 4.3). Figure 4.15a shows the observed spectra collected from a measurement of 1 mm liquid CS_2 . This spectrum is part of a set of measurements collected on the same day and which helped reveal the Fano interference behavior common to CoBS measurements approaching the sensitivity limit. While the spectrum in Figure 4.15a shows mild to no Fano asymmetry, spectra corresponding to other pump-probe detunings display strong Fano asymmetry (see Section B.3.2 in Appendix B for a description of the experiment and Figure B.3 for the full measurement set). Figure 4.15b shows the spectrum obtained from a CoBS measurement of 100 μm liquid CS_2 . The signal-to-noise ratio (SNR) of this measurement is significantly lower than that of the 1 mm liquid CS_2 spectrum, as expected from the $100\times$ reduction in scattered power produced as a result of the $10\times$ reduction in effective length. Finally, Figure 4.15c shows the spectrum obtained from a CoBS measurement attempt of 10 μm liquid CS_2 , binned to 20 MHz bins. While the scattered power produced remains theoretically within the sensitivity limit of the instrument, a successful measurement of 10 μm liquid CS_2 could not be obtained, likely due to variations in experimental conditions. Furthermore, due to the short phonon mean travel distance $L_{\text{coh}} = (13 \pm 2) \mu\text{m}$, the 10 μm path length cell would still have been insufficiently short to exhibit Brillouin-induced Raman modes. A $\sim 5 \mu\text{m}$ path length cell would be required for this result.

CS₂	$\Gamma_B^{1,3,86,87}$ (MHz)	τ (ns)	$v_{s,\text{long}}^{1,3,21,107}$ (m s ⁻¹)	$n^{1,3}$	L_{coh} (μm)	$P_{\text{CoBS}, L_{\text{coh}}/2}$ (pW)	Ω_B (GHz)	$\Omega_R, 1 \mu\text{m}$ (GHz)
Liquid	$2\pi \cdot 90 \pm 10$	10	1150	1.59	13 ± 2	~ 7.2	$2\pi \cdot 2.54 \pm 0.03$	$2\pi \cdot 0.575$

Table 4.3: Material parameters for bulk liquid CS₂ relevant to observing Brillouin traveling-wave modes and Raman standing-wave modes, obtained from published values as well as our own observations shown in Figures 4.7a, 4.7b, 4.15a, and 4.15b. Here, Γ_B is the angular Brillouin linewidth (phonon dissipation rate) and the inverse of phonon lifetime ($\tau = (2\pi \cdot \Gamma_B)^{-1}$), $v_{s,\text{long}}$ is the longitudinal sound speed, n is the refractive index, l_{coh} is the phonon coherence length (mean travel distance), and P_{CoBS} is the scattered power for the CoBS process, reported here for $L_{\text{coh}}/2 = 6.5 \mu\text{m}$ CS₂, and scales with L^2 (Equation 4.3). Finally, Ω_B is the angular Brillouin frequency shift (Equation 4.1), and $\Omega_R, 10 \mu\text{m}$ is the first harmonic ($n = 1$) of the fundamental L_0 Raman-like mode for $L = 1 \mu\text{m}$ (Equation 4.2).

4.3.6 Suspended Silica Rib Waveguide

A collaborative connection was made with Dr. Aaron Hawkins' Semiconductor Devices and Microfabrication group at Brigham Young University (BYU) which opened up new possibilities for photonic-phononic interactions and control of phonons at room temperature. The Hawkins group specializes in advanced chip-waveguide and device design and fabrication, introducing the possibility for a collaboration with a widened sandbox of available materials and platform designs. We received suspended silica rib waveguides for initial investigation and proof of principle. The goal was to measure backward Brillouin scattering in the silica rib of these suspended waveguides with the CoBS instrument. The main challenge of this task became evident immediately: getting light into the chip. The method available was via careful fiber-to-chip alignment to align the cone of light output from the fiber end to be injected into the silica rib waveguide. Initial attempts were unsuccessful due to imprecise XYZ control and lack of experience. After many weeks of unsuccessful attempts and several video consultations with the Hawkins group for guidance, the opportunity was presented to visit the Hawkins group at BYU in Provo, UT. This friendly and illuminating trip immediately shored up the lacking knowledge and experience, allowing for immediate success getting light into the chip upon return home. However, the silica rib waveguide closely shares many properties with the silica SMF-28 which comprises much of the CoBS apparatus and the entirety of the sample stage where all interacting light and sound waves overlap.

Initial measurements of the waveguide captured a spectral feature which seemed to match the known spectral response of the SMF-28 at $\sim (10.8 \pm 0.5)$ GHz. However, with perseverance and improved alignment of light into and out of the chip waveguide, distinct spectral features were observed which differentiated the response of the chip waveguide from the background measurement performed with chip waveguide re-

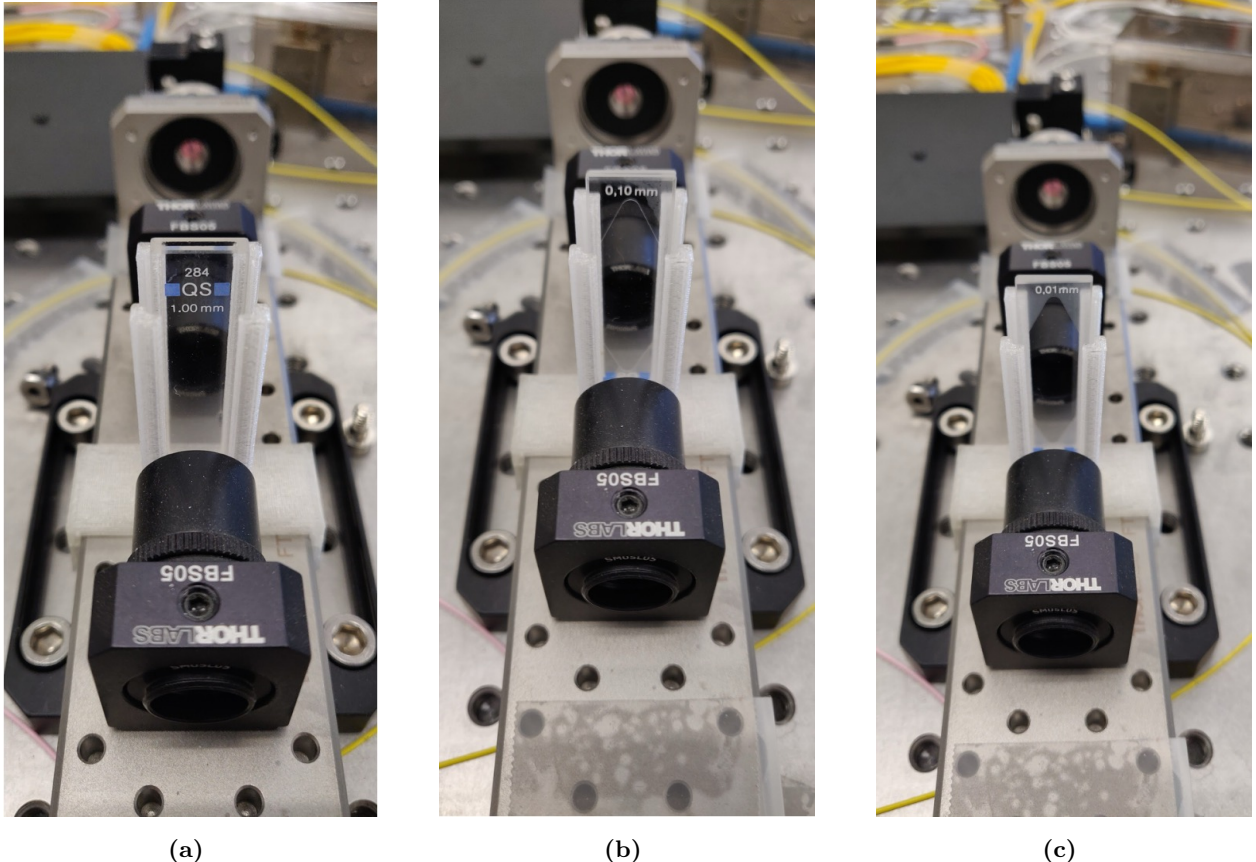


Figure 4.14: Three CS_2 cells of different path lengths (1 mm, 100 μm , and 10 μm) secured in the beam path of the Coherently stimulated Brillouin Spectrometer.

moved. Figure 4.16 shows spectra gathered subsequently with and without the chip waveguide present in the instrument. A clear feature of the chip at $\sim 10.84 \text{ GHz}$ rises above the background SMF-28 response, centered at $\sim 10.82 \text{ GHz}$. This plausible measurement represented a significant step towards harnessing the opportunity of specialized chip-waveguide design to control phonons at room temperature and potentially observe Brillouin-induced Raman modes.

4.3.7 Elastically-Suspended Photonic-Phononic Waveguide

In this section we provide analysis of expected optomechanical behavior from a specialized photonic–phononic waveguide suspended on a thin memberane of elastic SU-8 polymer, primarily used as a negative photoresist which acts as a sacrificial layer in forming complex layered designs. Instead, through collaborative discussions sharing ideas and specific domain knowledge, Dr. Hawkiins proposed we may see a big mechanical response from the elastic nature of the SU-8. It was also suggested to design notches or similar feature to support acoustic guidance down the length of the waveguides. Improved acoustic guidance would produce

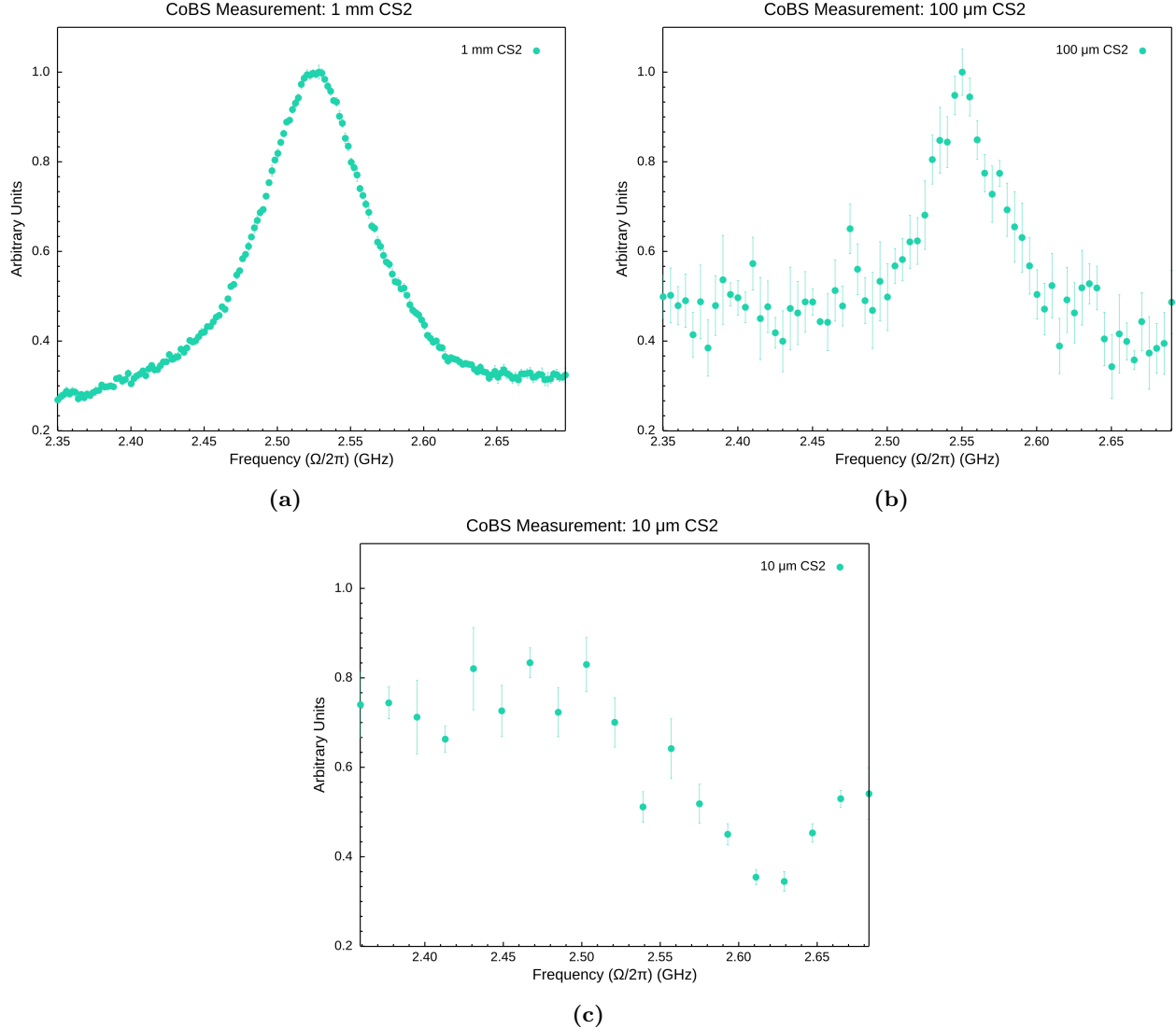


Figure 4.15: Observed background-subtracted spectra obtained through CoBS measurements of (a) 1 mm, (b) 100 μ m, and (c) 10 μ m liquid CS₂ (pictured in Figure 4.15c), captured at maximum operating optical powers $P_P P_S P_{Pr} \sim 0.25 \text{ W}^3$. All measurements have 1σ uncertainties smaller than the data point markers.

stronger opto-mechanical interactions between light and sound along the length of the waveguide due to more tightly confined mode overlap (A_{eff}^{ao}). Lengthwise notches or other similar feature might also be designed as lengthwise acoustic resonators to trap traveling-wave phonons stimulated in the silica rib, thus effectively producing a controllable n-multiple of short path length samples within one chip waveguide by fabricating the side rails along the rib to feature n number of lengthwise acoustic resonators of desired spacing. These design features were indeed implemented, and successful proof of principle elastically-suspended photonic-phononic waveguides were created and sent to us for testing.

Figure 4.17 plots the spectra collected from an initial test CoBS measurement of backward Brillouin

CoBS Measurement: 1 cm Suspended Silica Rib Waveguide

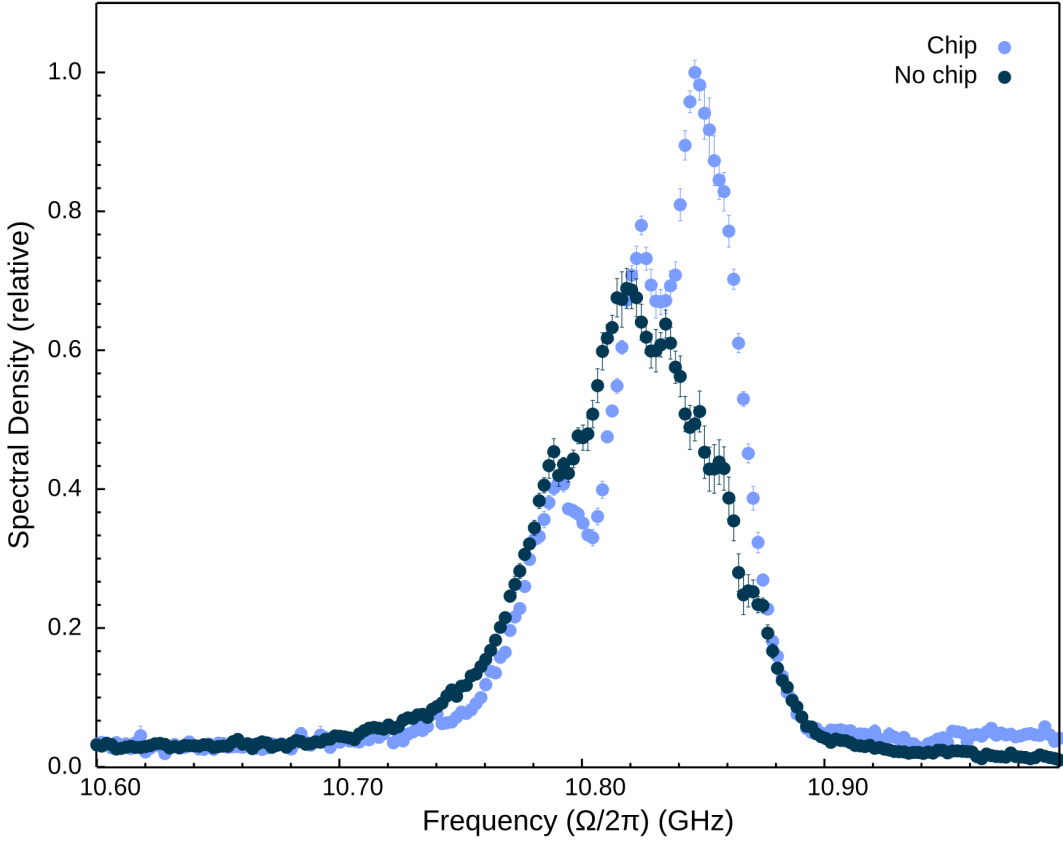


Figure 4.16: CoBS measurement of a suspended silica rib waveguide for a backward scattering process. A subsequent measurement with the chip waveguide removed is also plotted. The spectral response of the SMF-28 which comprises much of the sample stage of the instrument is visible without the chip, however a notable signal from the waveguide can be seen above the background. In obtaining the spectra, five repeated measurements of both the signal and background (probe off) were collected at a 100 Hz resolution bandwidth (RBW), dwelling for 1 s at each 5 MHz frequency step. Plotted is the resulting background-subtracted spectrum. Uncertainties represent 1σ standard error of the mean.

scattering in the elastically-suspended silica rib of the photonic-phononic waveguide. While some spectral features differ between the chip and No chip measurements, additional measurements and testing are required to confirm or deny the significance of these apparent features. In what follows, we present preliminary theoretical estimates of the key mechanical modes and optomechanical couplings predicted for the elastically-suspended photonic-phononic waveguide under development. The structure under consideration consists of a polymeric (SU-8) membrane that is tensioned during high-temperature curing and supports a rib waveguide above it. This combined membrane-and-rib geometry gives rise to multiple distinct mechanical resonances that can be excited and probed optically via the CoBS instrument operating in the forwards scattering configuration. We summarize below the principal modes, referred to as “drumhead” modes for the membrane and “breathing” modes for the rib, and estimate rough frequency ranges in which they are expected to appear.

CoBS: 1 cm Elastically-Suspended Photonic-Phononic Waveguide

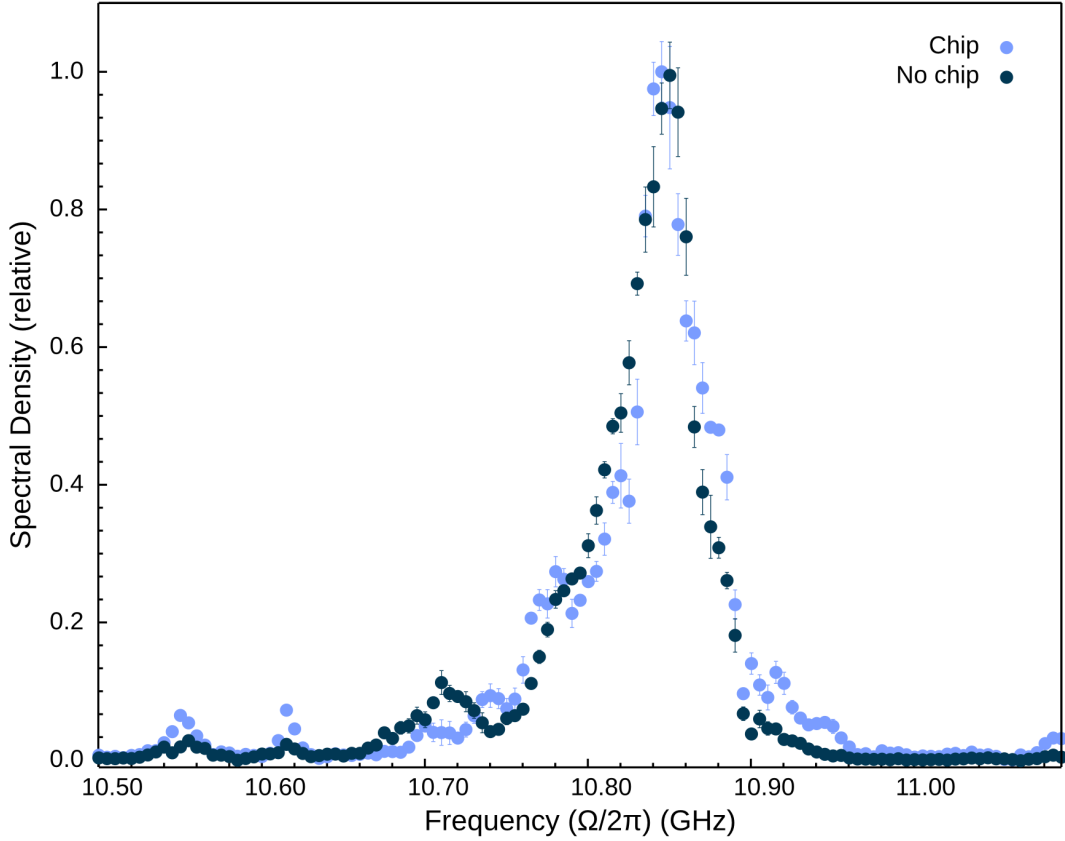


Figure 4.17: CoBS measurement of the elastically-suspended photonic-phononic waveguide for a backward scattering process. A subsequent measurement with the chip waveguide removed reveals a similar spectral profile, as expected from the identical resonant frequency response of the SMF-28 which comprises much of the apparatus, especially in the sample region of the instrument where all three optical powers overlap. In obtaining the spectra, five repeated measurements of both the signal and background (probe off) were collected at a 100 Hz RBW, dwelling for 1 s at each 5 MHz frequency step. Plotted is the resulting background-subtracted spectrum. Uncertainties represent 1σ standard error of the mean.

We first consider the rib portion of the waveguide, having characteristic lateral width and thickness of 4 cm and 6 cm, respectively. One can treat the smallest cross-sectional dimension, denoted d , as setting the approximate half-wavelength condition for its fundamental breathing mode. The simplest estimate for such a half-wavelength mechanical resonance is given by

$$f_{\text{rib,breathe}} \approx \frac{v_s}{2d}, \quad (4.8)$$

where v_s is the speed of sound in the silica rib and d is the lateral width. Taking the rib to be 6 μm wide and assuming a speed of sound in the range 5 km s^{-1} to 6 km s^{-1} , this places the fundamental rib breathing

mode near several hundred MHz (estimates range from 400 MHz to 500 MHz). Higher-order modes can arise (integer multiples of the half-wavelength condition), and so in practice one expects a series of possible breathing modes in the 100s of MHz to low-GHz range.

In principle, when optically excited via the CoBS process, the rib breathing mode can couple to and drive displacement of the underlying membrane. Conversely, membrane motion at or near the rib's breathing-frequency range can stimulate the rib's motion. Indeed, the waveguide design permits either the drumhead mode of the membrane or the rib breathing mode to be excited off-resonance and potentially induce mechanical vibration in the other. Beneath the rib, the polymer membrane is suspended over an open region which has been etched away, and is anchored on either side. We thus expect a classical drumhead family of modes in which the membrane oscillates out-of-plane. The tension provided by the fabrication curing process indicates that the membrane is tension-dominated. For a square membrane of length and width L , under tension T and with mass density ρ and thickness h , the fundamental frequency (1,1) can be approximated by

$$f_{\text{membrane, drumhead (1,1)}} \approx \frac{v_s}{\sqrt{2L}}, \quad (4.9)$$

where v_s is the *transverse* sound speed of the membrane, given by

$$v_s = \sqrt{\frac{T}{\rho h}} = \sqrt{\frac{\sigma h}{\rho h}} = \sqrt{\frac{\sigma}{\rho}}, \quad (4.10)$$

where σ is the stress (Pa) corresponding to the tension per membrane thickness ($\sigma = T/h$).

Modeling the polymer membrane as a square membrane, we can estimate the fundamental membrane drumhead mode using a mean density of SU8 ($\rho = 1190 \text{ kg m}^{-3}$)¹⁰⁸ and needle profilometer tension measurements performed on the membrane. Figure 4.18 plots deflection for various stylus force values applied to the membrane. The inverse of the slope of these data (taken to be linear, $m \sim 300 \text{ N m}^{-1}$) allows for the membrane's approximate tension to be found via $T = \frac{L}{4}m \sim 2 \text{ mN m}^{-1}$. For a 2 μm -thickness with Equation 4.10, this gives an approximate transverse sound speed of a very low $v_s \sim 1 \text{ m s}^{-1}$. Inserting this into Equation 4.9 with length $L \approx 25 \mu\text{m}$, we anticipate the fundamental drumhead mode resonant frequency of the SU8 membrane to lie around 30 kHz. Meanwhile, the rib breathing mode are predicted to lie around the mid-100s of MHz. Given this 4-order-of-magnitude discrepancy in resonant frequencies, the two mechanical modes are not expected to exhibit mechanical coupling, even when accounting for the possibility of off-resonant driving. To have the two resonances approach each other, one might alter the fabrication parameters to

try significantly increasing the resulting tension of the membrane, perhaps by experimenting with different bake times or temperatures and membrane thicknesses. Alternatively, or additionally, shortening the length L across which the membrane spans from clamp-to-clamp would minimally nudge its resonant frequency higher.

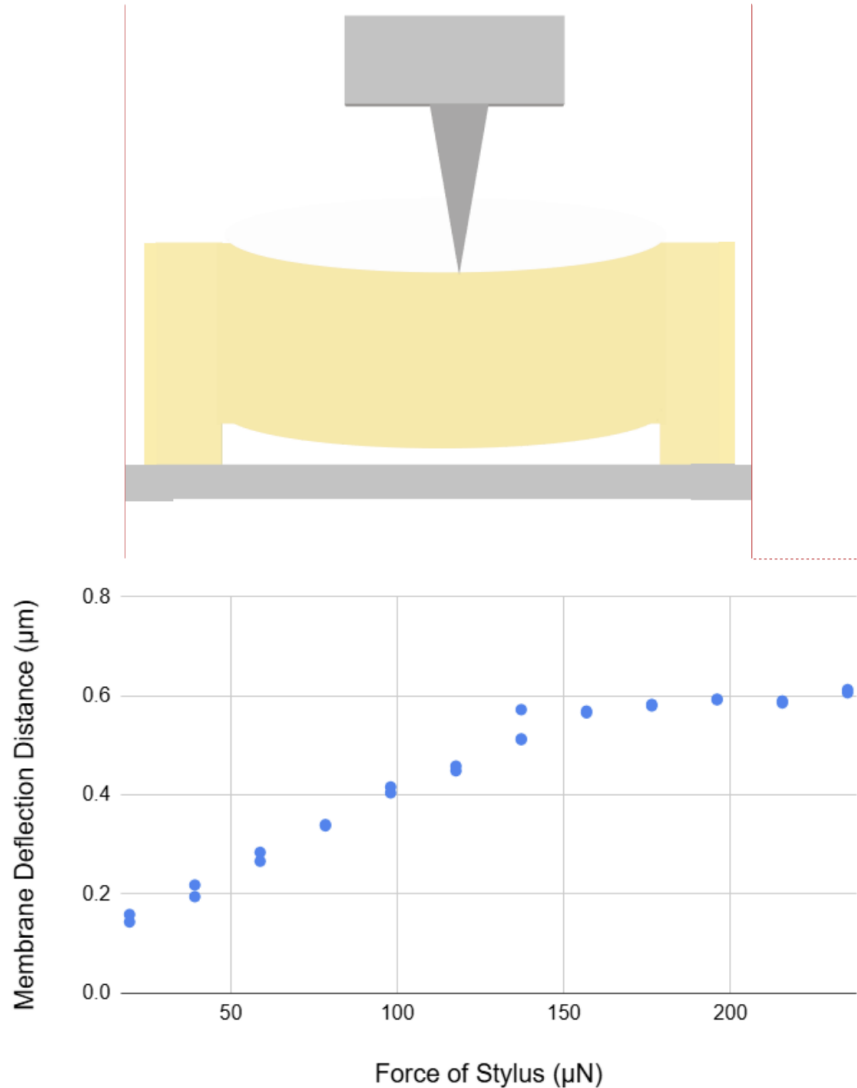


Figure 4.18: Needle profilometer force-deflection measurements (illustrated above) performed on the suspended polymer membrane of the photonic-phononic waveguide. The inverse slope of the data (taken to be linear) is proportional to the tension of the membrane ($m \propto T$). Using $m \sim 300 \text{ N m}^{-1}$, we estimate the tension of the membrane to be $T \sim 2 \text{ mN m}^{-1}$, giving a transverse sound speed $v_s \sim 1 \text{ m s}^{-1}$ via Equation 4.10. Figure courtesy of Adams et al., *manuscript in prep.*

4.4 Discussion

In this chapter, we have investigated the potential for creating Raman-like vibrational modes via Brillouin interactions in a variety of photonic and phononic structures. By examining how traveling-wave phonons can be transformed into standing-wave resonances, we bridge the gap between conventional Brillouin physics (characterized by traveling acoustic phonons) and a regime reminiscent of Raman scattering (where standing-wave vibrations couple strongly to light). Our experimental and theoretical efforts illustrate both the challenges and the promising pathways for realizing stable, high-quality, Brillouin-induced Raman modes in waveguides, crystals, and fibers. Below, we synthesize the key findings and discuss future directions.

4.4.1 Pathways to Brillouin-Induced Raman Modes

A central goal has been to identify platforms capable of generating high- Q standing-wave vibrational modes, analogous to conventional Raman-active modes, by leveraging Brillouin coupling in materials where both the optical and the acoustic (or elastic) degrees of freedom can be engineered. These results highlight how geometry, acoustic impedance contrasts, and overall device configuration govern the competition between traveling- and standing-wave phonons. Here, we group the ideal platforms by three broad categories: waveguides, TeO₂ crystals, and fiber-based approaches. A promising strategy for forming Raman-like resonances emerges from waveguide geometries that confine both light and sound. Notably, thin-film rib waveguides of TeO₂ are attractive due to the high photoelastic coefficients of tellurite glasses and the possibility of incorporating evenly spaced square holes to pin acoustic modes. The fabrication of a long rib waveguide on the order of centimeters can allow an extended optical interaction length while introducing a phononic band structure via an engineered hole pattern. This pattern can create a 1D phononic bandgap, effectively reflecting phonons to form standing waves at selected frequencies. Tellurite-based waveguides combine strong Brillouin gain with a sufficiently low acoustic damping rate to enable coherent standing-wave formation at room temperature (Section 4.3.3). Moreover, the large refractive index contrast of TeO₂ relative to silica cladding supports robust optical confinement. As in earlier suspended photonic-phononic waveguides (Section 4.3.7), the tension in the membrane can significantly alter the acoustic mode spectrum. Proper design of periodic corrugations and sidewalls ensures that back-reflection of phonons gives rise to well-defined modes at the relevant Brillouin frequency. By tuning geometric parameters such as hole spacing, it is possible to achieve a strong overlap of optical and acoustic fields for selective mode conversion.

Although many of our demonstrations focused on thin-film TeO₂, a bulk or thick-crystal platform is also a compelling route for Brillouin-induced Raman effects. TeO₂ boasts among the largest photoelastic coefficients for chalcogenide or oxide glasses, making it an exemplary host for strong acousto-optic coupling.

In a bulk crystal with polished facets or embedded reflectors, backward Brillouin scattering may transition into a standing-wave configuration, mimicking a Raman-like resonance. Relative to many polymeric or silica systems, crystalline TeO₂ can exhibit reduced phonon damping, particularly for carefully oriented crystal axes. This intrinsic advantage can facilitate a higher mechanical Q and a narrower linewidth, key ingredients for stable Brillouin-induced Raman modes. Realizing a clear set of discrete “Raman-like” lines in a bulk crystal requires controlling reflections at each interface. Spurious acoustic reflections or partial mode mismatch can excite multiple unwanted phonon branches, broadening the spectrum. Future work could integrate an acoustic Bragg grating within the crystal or deposit patterned reflectors on crystal faces to support more robust mode confinement.

Finally, optical fibers remain one of the most convenient photonic platforms for combining long interaction lengths with precise control over acoustic guidance. Introducing a series of periodic notches or refractive index modulations forms an acoustic mirror inside the fiber, providing a route to localized standing-wave phonons. Unlike conventional uniform-core fibers where traveling acoustic waves dominate, these fiber Bragg structures can reflect phonons at targeted frequencies. Once the phonon reflectivity is sufficiently high, coherent standing waves arise, facilitating strong coupling to the Stokes and anti-Stokes sidebands. Implementing an acoustic fiber Bragg grating must balance strong reflection of phonons (to produce standing-wave modes) with minimal introduction of optical loss. While doping or microstructuring the fiber is feasible, the potential for scattering or wavefront distortion may impact optical guidance.

Collectively, these three categories (TeO₂ waveguides, TeO₂ crystals, and notched acoustic fibers) demonstrate overlapping yet distinct methods for accessing Brillouin-induced Raman modes. Each system can be fine-tuned for specific applications: TeO₂ waveguides for integrated photonics where footprint is critical; bulk crystals for high- Q acoustic experiments; and fiber-based geometries for long-distance coupling and simpler device integration.

4.4.2 Conclusion

By mapping the transition from traveling-wave Brillouin phonons to standing-wave Raman-like modes across these diverse platforms, we underscore the broad adaptability of optomechanical coupling at room temperature. The demonstrations in this chapter affirm that controlling acoustic boundary conditions, whether via physical reflectors, periodic perturbations, or intrinsic interface mismatches, lies at the center of generating stable, high- Q vibrational modes. The overarching theme of the work presented in this document is control of phonons at room temperature. The progress reported here highlights that we do not need to confine ourselves exclusively to classical Raman systems or purely Brillouin-based traveling-wave scenarios. Instead,

it is possible to strategically blend the strengths of each to realize new types of hybrid resonances with unique spectral signatures. Ultimately, these Brillouin-induced Raman modes broaden the scope of optomechanical interactions. They show that even modest structural modifications, whether in waveguides, bulk crystals, or specialized fibers, can tip the balance away from purely traveling acoustic waves toward fully resonant, discrete modes. This tunability promises new device functionalities at telecom and near-infrared wavelengths, where controlling phonons in tandem with photons stands to accelerate advances in sensing, signal processing, and quantum photonics.

Chapter 5

Conclusion

Throughout this dissertation, we have explored how Brillouin-based optomechanics can be harnessed for both practical device applications and fundamental studies of light–matter interactions. Specifically, we demonstrated that traveling-wave phonons in an extended medium, such as a liquid-core optical fiber, can be cooled significantly through the anti-Stokes Brillouin scattering process. This result marks an important step in transitioning from the established model of discrete cavity modes toward the more general case of continuous-waveguide phonons, showing that key regimes of laser cooling can be accessed without relying on highly engineered photonic microstructures.

In tandem, this dissertation introduced the concept of a coherently stimulated Brillouin spectrometer (CoBS), which relaxes traditional phase-matching constraints and dramatically increases measurement sensitivity for short-length or low-gain samples. By incorporating a four-wave mixing scheme—pump, probe, driven Stokes, and backscattered signal—the spectrometer opens new avenues for measuring the mechanical modes of thin films, microscale liquid volumes, and emerging photonic–phononic waveguides. This flexibility is crucial for advancing applications ranging from precision material characterization to integrated acousto-optic devices.

Beyond traveling-wave phonons, we also proposed how Brillouin-induced Raman-like modes might be generated and observed, potentially bridging the gap between conventional Raman spectroscopy and Brillouin acoustics. Although direct experimental realizations of these hybrid modes remain at an early stage, the theoretical groundwork and device prototypes described here highlight the promise of such approaches for both fundamental and applied research. Ultimately, these efforts underscore the rich variety of phononic phenomena accessible when one leverages strong acousto-optic interactions in engineered media.

Looking ahead, an important direction will be to pursue net phonon cooling in waveguides by minimizing or routing away the unwanted Stokes contributions. Achieving such deep cooling could open pathways to ground-state phonon occupancy, enabling quantum acoustic memory and photon–phonon entanglement protocols. In tandem, refining the CoBS method to push detection limits and spatial resolution even further

may help unlock additional device architectures across the fields of quantum information, ultralow-noise photonics, and advanced sensing. In this way, the work presented herein lays the foundation for continued innovation at the intersection of photonics, phononics, and materials science.

Appendix A

Supplementary Information for Chapter 2

A.1 Fabrication of CS_2 -Filled Liquid-Core Optical Fiber

Fabrication of the liquid-core optical fiber (LCOF) followed the methods described by Kieu et al. (2012)²⁰. The fabrication process involved several key steps for each of the two ends: splicing single mode fiber 28 (SMF-28) to Ultra High Numerical Aperture 7 (UHNA7) fiber, preparing and angle-cleaving fibers, cutting and preparing a protective glass vial, and finally securing the assembly on a microscope slide. Figure 2.2 in the main text illustrates the overall schematic of the fiber fusion strategy, showing how SMF-28 and UHNA7 fibers flank the hollow core. The following sections detail each step in the splicing, assembly, and filling processes in fabricating the CS_2 -filled LCOF.

A.1.1 Splicing

Before integrating the hollow-core segment, a segment of Corning SMF-28 was spliced to Thorlabs UHNA7 fiber. This transition was necessary to gradually match the mode fields and reduce losses at the interface with the hollow-core region.

To begin, a short length (0.5 m) of SMF-28 was stripped, cleaved flat, and arc-spliced to 5–10 cm of similarly prepared UHNA7 fiber. The UHNA7 fiber was fully stripped of its coating prior to arc-splicing. This was done to prevent up-and-down bending of the fiber end in subsequent horizontal alignment with the Vytran fusion splicer. The initial splice was performed with standard parameters, but the arc was then repeated four to five times in order to produce a “tapering” effect which helped narrow the SMF-28 core (9.2 μm diameter) where it contacted the smaller UHNA7 core (2.4 μm diameter), improving coupling efficiency. Prior to and following the splice, optical transmission measurements were taken to assess the splice quality and ensure maximum transmission was preserved.

After the preliminary SMF-28–UHNA7 splice, the UHNA7 fiber needed to be angle-cleaved to ensure a gap remained for CS_2 to be able to enter the hollow-core fiber after fusion-splicing the two fiber segments. An

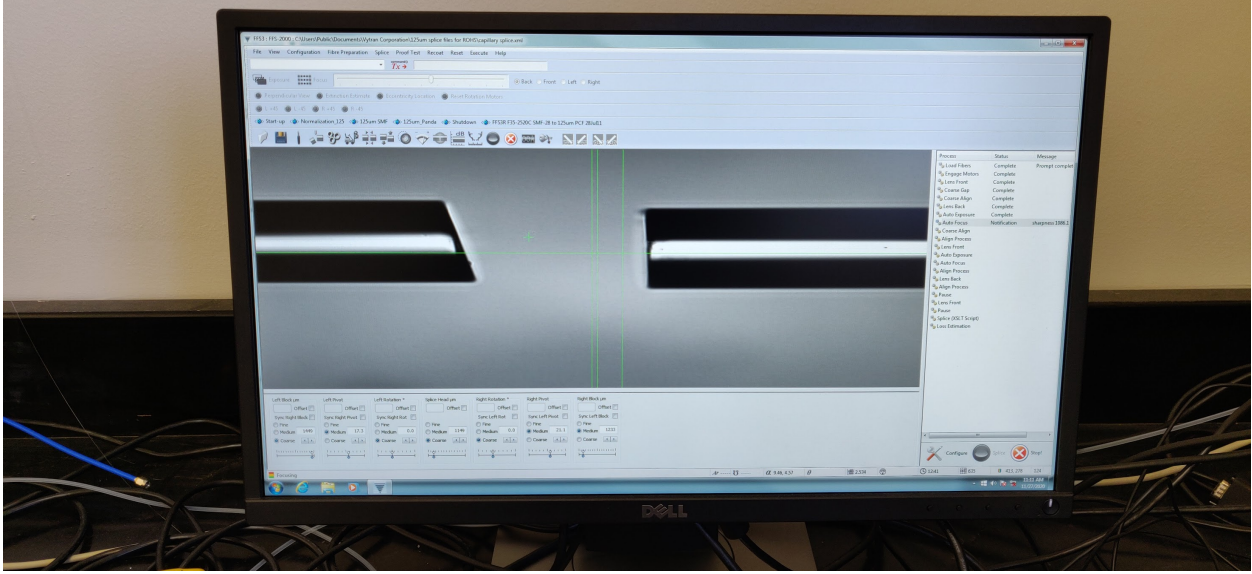


Figure A.1: Picture of Vytran software interface camera imaging system showing a microscope view of the two fiber ends pre-splice (Section A.1.1). The left angle-cleaved fiber is the UHNA7 fiber. The right flat-cleaved fiber is the hollow-core fiber. Subsequent alignment processes, first automatic then manual fine-tuning, align the fibers in xy space for optimal fusion-splicing and optical transmission once filled.

angle-cleaver with an adjustable torque and tension mechanism was used for this process. The angle-cleaved SMF-28-UHNA7 segment was then loaded into the Vytran fusion splicing system:

1. Equipment Setup: The Vytran fusion splicing station and its vacuum pump were turned on, and the system's dedicated software interface was opened. Approximately two minutes was allowed for the vacuum level to stabilize.
2. Fiber Positioning: The left fiber clamp block was pivoted fully to the left, and the UHNA7 fiber was placed so that its freshly cleaved tip was centered over the reference circle at the splice head.
3. Alignment: While the vacuum held the fiber in place, the system's camera view was used to rotate the fiber such that the sharpest angle of the UHNA7's end face was in the camera's view. A small "flag"—a piece of unstripped fiber with a small tape handle on one end—was used as needed to help the clamp grip the bare UHNA7 fiber securely.
4. Pivot and Support: The left block was pivoted back and forth until the UHNA7 tip was near the correct horizontal position. A folded piece of support paper and two boxes of Kimtech Kimwipes on the benchtop were used to prevent the fiber from drooping and to minimize the risk of breakage during handling.

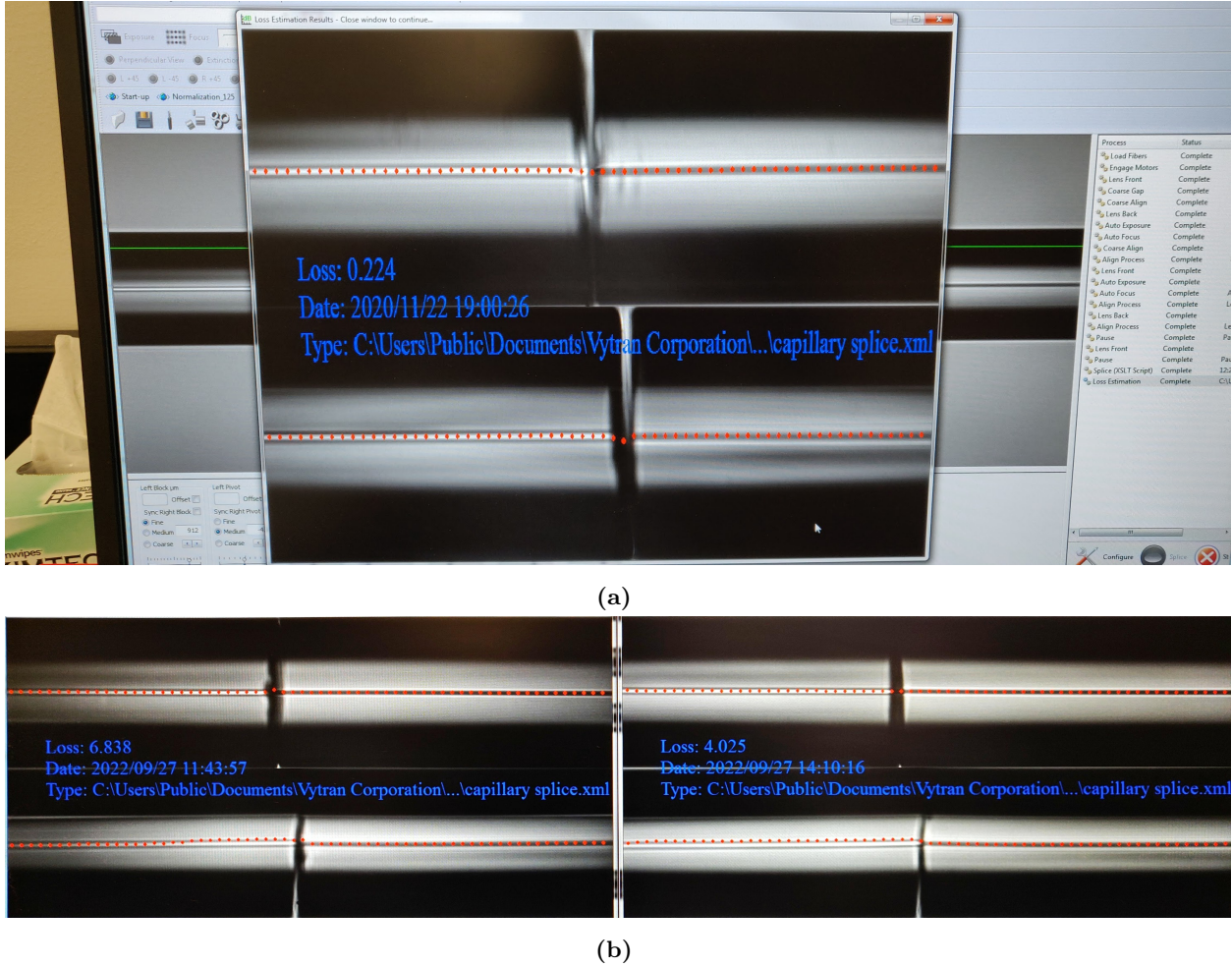


Figure A.2: Example images of LCOF splices (Section A.1.1). Figure (a) shows an earlier example of a splice which featured a large visible wedge-shaped gap for liquid to enter the hollow-core fiber. While gaps of this size were sometimes successfully transferred onto a slide, further investigation showed gaps of this scale to reduce optical transmission through the splice. This fact became critical later for collecting the data for the pump-probe experiment. Figure (b) shows images of the two splices featured on the ultimate sample which was used to gather final data for publication.

Once the UHNA7 fiber was properly angle-cleaved, the hollow-core fiber segment was prepared for splicing:

1. Stripping and Cleaving: The hollow-core fiber coating was gently dissolved in acetone and wiped away to expose the bare glass. It was then cleaved flat rather than at an angle.
2. Positioning on the Vytran fusion splicer: The right clamp block was pivoted to its stop position, and the hollow-core fiber was placed so its end was centered over the splice head's circle, ensuring no physical contact with the UHNA7 fiber.

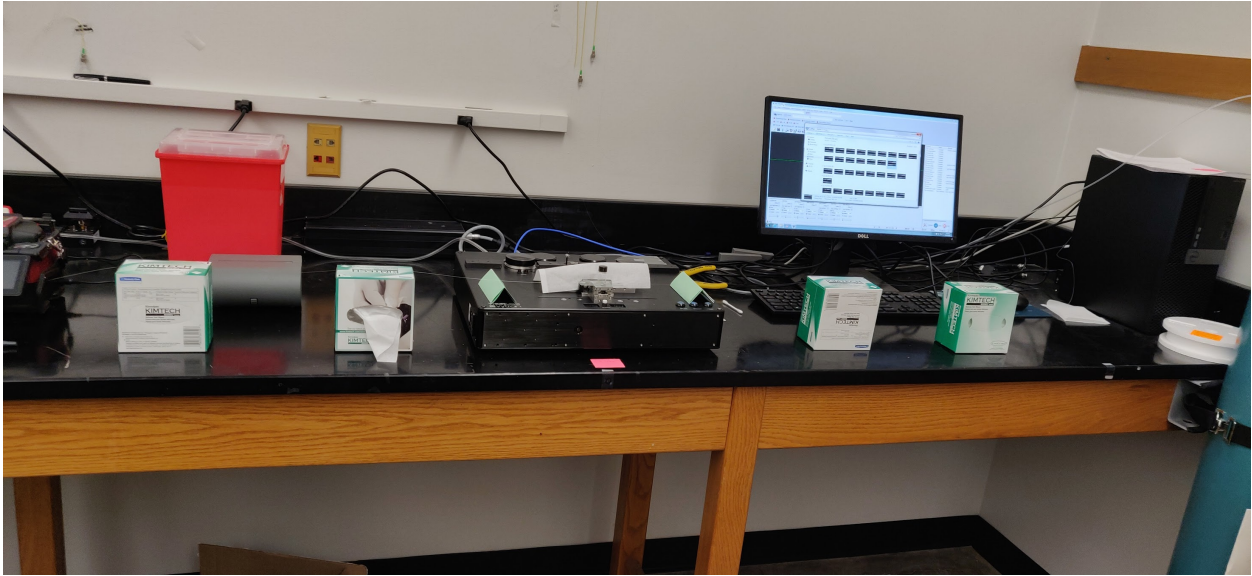


Figure A.3: Picture of both lengths of fiber braced by folded paper and two Kimwipe boxes on either side to prevent bending and flexing while transferring the delicate splice onto a glass slide (Section A.1.1).

3. Flag and Alignment: As with the UHNA7, a flag of unstripped fiber was placed above the hollow-core fiber to facilitate stable clamping. The right clamp block was slowly pivoted toward the center until the fiber tips were close but still not touching. Like before, the fiber was supported with folded paper and Kimwipe boxes to prevent bending.

The next step was to form the final fusion splice between the UHNA7 fiber and the hollow-core segment within the fusion splicer:

1. Positioning and Auto-Alignment: With both fibers supported and extending naturally from opposite blocks, the splicer's auto-alignment was initiated. The system brought the fibers within viewing distance so the operator could adjust vertical and horizontal positioning.
2. Core Alignment: Using the splicer's camera interface, the UHNA7 core was lined up with the hollow-core's central region. Small vertical and horizontal translations ensured good overlap.
3. Fiber Touch-Off: The left fiber (UHNA7 side) was carefully advanced until the tips touched, then retracted two clicks for optimal separation during splicing. Precise final positioning of the fiber ends ensured that a small gap remained in the hollow core to accommodate liquid infiltration during the filling process. Simultaneously, this same fiber end positioning ensured the cladding regions were fused sufficiently to preserve splice integrity under the delicate handling steps that followed.
4. Argon Gas Flow and Fusion: An argon flow was introduced to shield the fusion region from contaminants, and the fusion filament heating was applied. Images were taken at each step to verify the splice

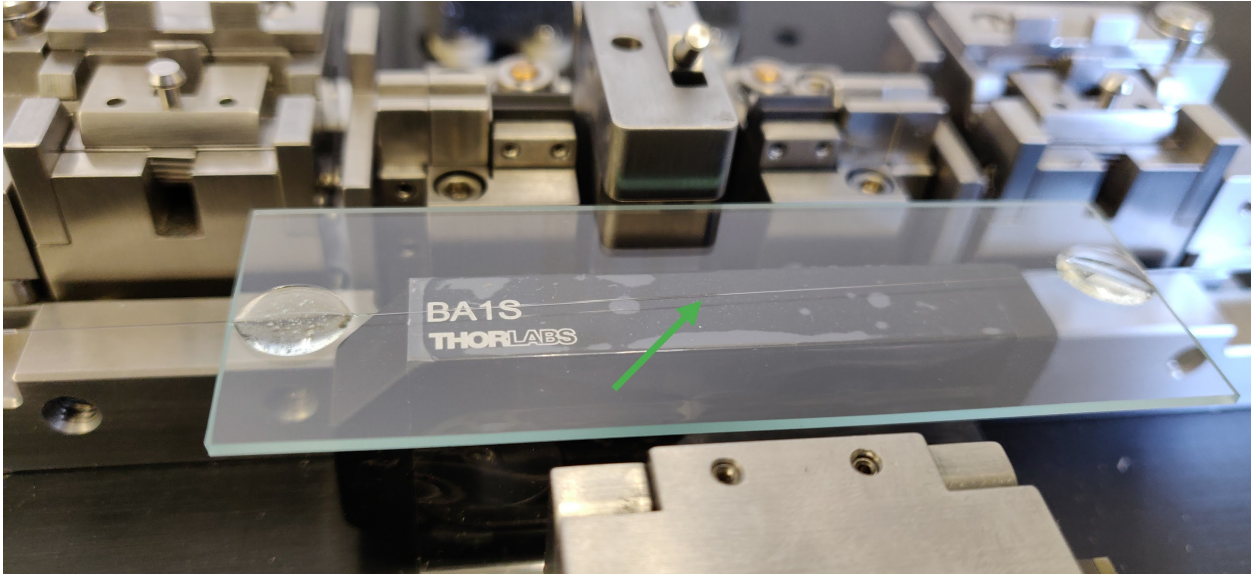


Figure A.4: Picture of splice successfully transferred onto a glass slide and tacked on either side with drops of epoxy (Section A.1.1). An arrow points to the location of the critical splice between the angle-cleaved UHNA7 fiber and the flat-cleaved hollow-core fiber.

quality. If alignment or splicing was inadequate, the fibers were separated, re-cleaved if necessary, and the procedure repeated. After confirming a good splice, the argon was turned off and the splicer was shut down.

A.1.2 Reservoir Assembly

Because the final splice assembly must be encapsulated for protection, it was mounted on a clean microscope slide. The slide was scrubbed with soap and a soft toothbrush under running hot water, then thoroughly rinsed and dried with an air gun. Clean handling was crucial, so the slide was placed inside a folded Kimwipe for safekeeping until needed.

A small glass vial was used to form a protective enclosure over the splice region and allow liquid to fill the hollow core.

1. Cutting the Vial: Wearing gloves and safety glasses, a new glass vial was secured carefully by hand and cut at low rotational speed on a saw. The cut removed only the bottom portion of the vial so that the main body of the vial remained relatively long.
2. Flattening and Notching: The cut edge was smoothed and flattened with a file block, and two shallow, wide straddle-gaps were added on opposite sides of the new opening. These gaps would later accommodate the fiber on the slide.

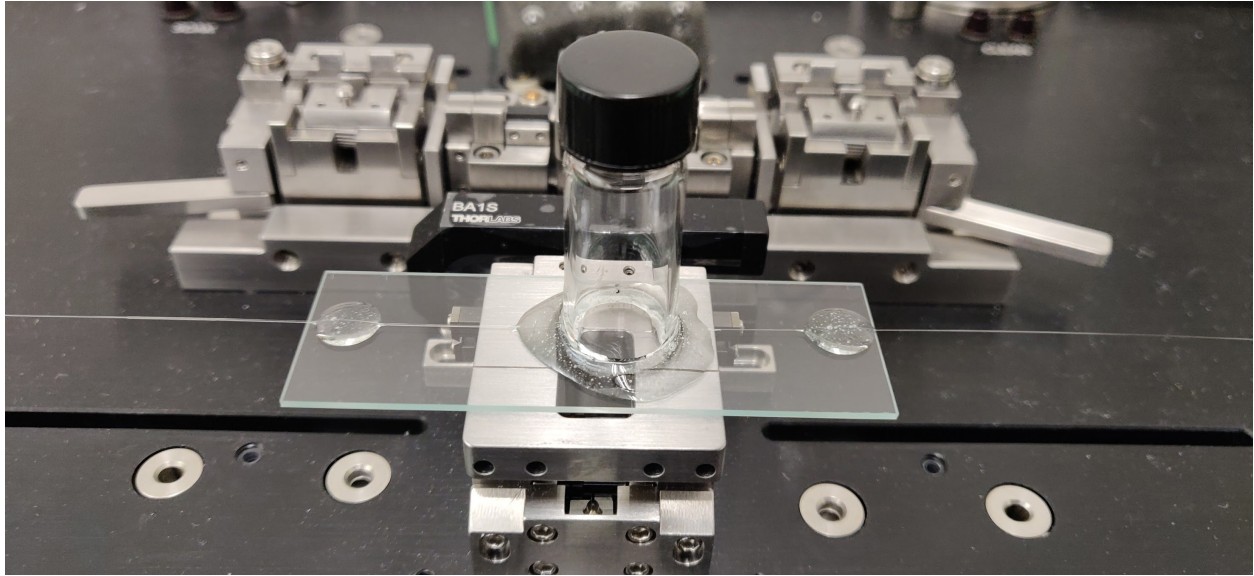


Figure A.5: Picture of a complete splice assembly (Section A.1.2). The hardened epoxy around the base of the vial securely holds the cut and notched vial onto the slide, forming a sealed reservoir around the critical splice. The reservoir is later filled with liquid CS₂ by easy removal of the screw-off cap in order to submerge the critical splice and begin the filling process of the hollow-core fiber via capillary action.

3. Cleaning: Finally, the vial was scrubbed with dish soap and a pipe cleaner, rinsed, dried with compressed air, and recapped until needed.

Upon completing the angle splice, the fiber assembly needed to be moved gently off the splicer onto the prepared microscope slide:

1. Release and Stabilization: With the splicer's vacuum pump still on to hold the splice securely, the magnetic latches clamping the fiber on either side of the splice to the translation/rotation stages were carefully lifted. Tweezers were used to remove any fiber "flags," and wooden craft sticks helped lift the fibers from the block grooves to free the fiber from any stuck position within the grooves.
2. Vacuum Shut-Off: The splicer's vacuum pump was switched off and the vacuum seal securing the fibers on either end of the splice was allowed to gradually release as air slowly equilibrated the pressure differential. The splice head and camera assembly remained overtop the splice for monitoring the camera feed on the computer screen. After approximately five minutes the camera feed would show the splice quickly move out of focus, indicating that the entire length of fiber was free and ready to be handled.
3. Placement on the Slide: With the splice head lifted, the slide was positioned directly in front of the splice and the fiber was transferred carefully in a smooth motion. Two small drops of epoxy were

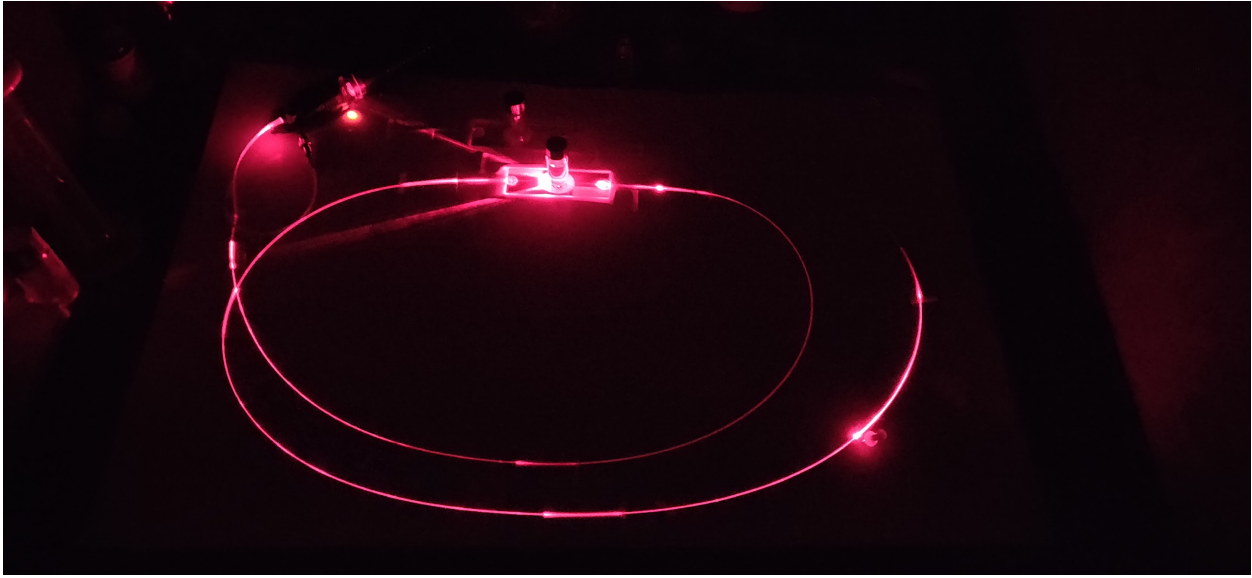


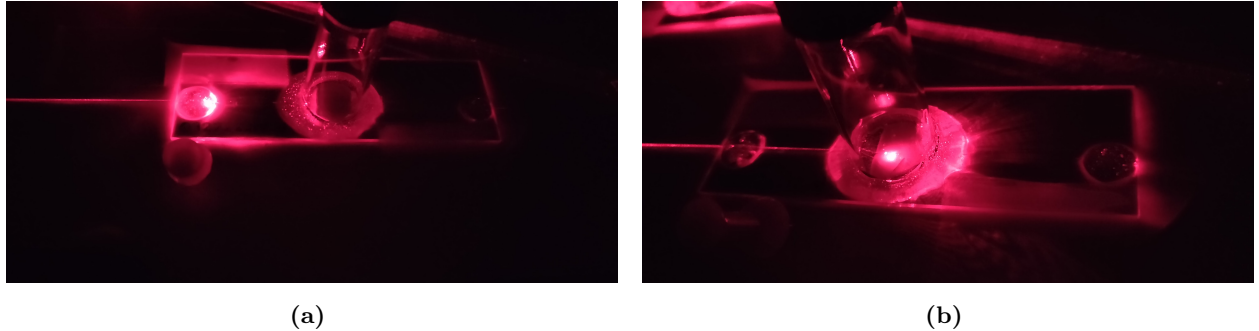
Figure A.6: Picture of a complete sample under the fume hood with lights dimmed and red laser light injected into the end of the sample for monitoring (Section A.1.3). The red light is partially guided along the length of fiber which has filled with liquid CS₂ and a thumb tack marks the progress of the CS₂-air interface.

placed on each side of the splice region to tack the fiber down. This was allowed to cure for at least five minutes.

The splice region was enclosed in a glass vial to protect the hollow-core's interior and to facilitate later filling with liquid:

1. Positioning the Vial: The prepared vial was placed over the splice region by sliding one straddle-gap around the fiber first, then tilting it so the second gap aligned. Gloves were worn to prevent transferring skin oils onto the vial.
2. Epoxy Sealing: A fresh mixture of two-part epoxy was prepared in roughly equal proportions and thoroughly mixed for 10–15 seconds to ensure a uniform bond. Generous epoxy was applied around the vial's perimeter where it contacted the slide. Care was taken to avoid epoxy wicking into the splice itself. The assembly was then left undisturbed for at least five minutes to cure.

Once the epoxy had set, the slide was labeled with the date, splice reference, and relevant notes using a marker. For long-term handling, the slide and its fibers were taped to a poster board to facilitate transport and prevent accidental breakage from jostling. This procedure ensured a robust, low-loss transition from SMF-28 to UHNA7 to the hollow-core fiber. The careful cleaning steps, controlled splicing environment with argon shielding, and meticulous handling minimized the risk of fiber breakage and guaranteed a clean optical interface. Encapsulating the splice with a modified glass vial on a microscope slide allowed easy



(a)

(b)

Figure A.7: Images of an LCOF sample in the filling process (Section A.1.3). Figure (a) shows the CS_2 -air interface a few centimeters from the end of the length hollow-core fiber, indicated by the red dot of scattered light just underneath the epoxy tack. From this position, the meniscus will typically reach the exit splice in approximately 4 hours. Figure (b) shows evidence of a fully-filled LCOF sample, indicated by the red dot of scattered light having reached the exit splice. If the pictured reservoir were to be filled prematurely, an air bubble would be locked in, reducing full transmission through the sample to nearly 0%.

manipulation of the hollow core's environment, which was crucial for subsequent liquid filling and optical characterization experiments.

Finally, this entire procedure was repeated on the opposite side of the hollow-core fiber to complete the LCOF assembly. Each splice was carefully optimized to be robust enough to guide light but also unfused enough to allow CS_2 to enter the hollow core via capillary action.

A.1.3 Filling with Carbon Disulfide

Once both ends of the hollow-core fiber were successfully spliced to their respective fiber pigtails, the next critical step involved filling the hollow core with carbon disulfide. Because CS_2 is highly volatile and poses health risks if inhaled, all operations were carried out in a fume hood with proper protective equipment.

The prepared LCOF sample, securely taped to a poster board, was transferred to the fume hood. A small red laser source was connected to the input pigtail; this red beam served as an in situ indicator of the fluid-filling front. The vial on the input side was uncapped, and the vial on the opposite side was loosened to prevent pressure buildup within the fiber. This arrangement ensured that as CS_2 entered the hollow core, displaced air could escape through the opposite vial, allowing continuous capillary flow.

To deliver the CS_2 , a syringe was first used to extract an adequate volume from a sealed supply bottle. The needle tip was then removed and replaced with a micron-level particulate filter, thereby minimizing the introduction of debris that could obstruct the hollow core. By gently angling the syringe, CS_2 was dispensed along the interior wall of the vial rather than dripping directly onto the delicate splice region. This careful approach reduced mechanical shocks, which could otherwise fracture or misalign the newly formed splice. Once the vial was filled, it was recapped promptly to prevent evaporation.

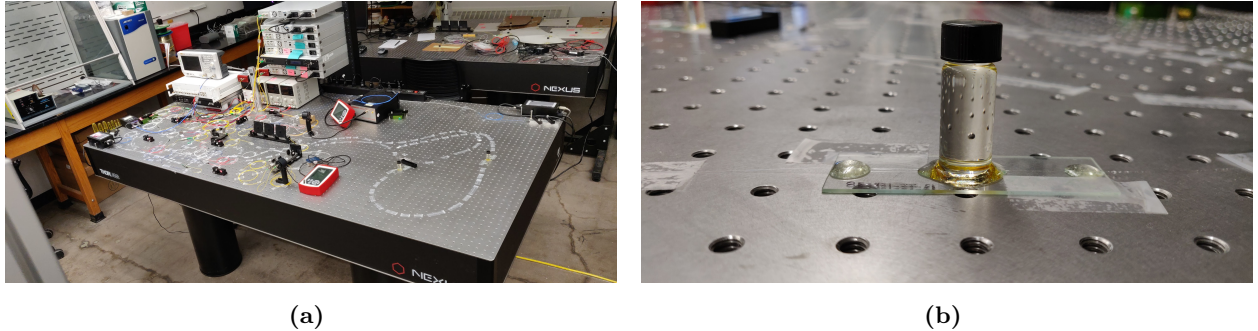


Figure A.8: Images of a fully finished CS₂-LCOF sample (Section A.1.4). Figure (a) shows a sample secured with tape to an optical table and integrated into an optical setup. Liberal use of tape ensured the safety of the sample as well as reduced vibrations and minimized changes in the polarization of light travelling through the sample. Figure (b) shows one splice assembly secured directly to the optical table via tape. Transfer of all parts of the sample from the poster board directly onto the optical table proved critical for eliminating noise and polarization drift issues with the pump-probe experiment.

If a given splice was imperfect—fully sealed at the fiber core rather than partially open—it prevented CS₂ from flowing in. Under these circumstances, no visible progression of the fluid meniscus would appear in the red laser beam path, confirming an unsuccessful splice. In contrast, if the splice was partially open, capillary action would begin immediately, typically drawing CS₂ several centimeters into the hollow core within seconds. The interface between the CS₂ and the air still occupying the rest of the fiber showed up as a faintly scattering “dot” in the path of the red beam. By darkening the room, this dot could be easily observed and tracked. Once the fiber was fully filled, the second vial was also filled with filtered CS₂, then capped. If the second reservoir was filled prematurely, an air bubble would be trapped in the final short length of hollow-core fiber and the resulting transmission through the full length of the LCOF would be reduced to nearly 0%.

Figure A.6 shows a picture of a sample in the process of filling with CS₂. Progress is marked by a thumbtack next to the CS₂-air interface. With the lights turned off, the dot of scattered light at this interface was a reliable visible indicator. Figures A.7a and A.7b show images of a sample that has nearly finished and fully finished filling, respectively. The filling state captured by Figure A.7a indicates a likely time to finish filling of approximately 4 hours.

A.1.4 Typical Optical Performance

Optical transmission at each splice typically ranged from 5–25%. The final LCOF used to gather the experimental results published in the paper associated with this chapter achieved full throughput transmission of about 17%. This suggests each splice individually offered an average of approximately 41% transmission of the incident light, assuming each splice provided equal transmission. In the demonstration of optome-

chanical cooling of traveling-wave phonons in this LCOF, the light collected at the detector is backscattered within the sample and thus passes back through the same splice that the incident pump light enters through. This round-trip backscattered LCOF transmission was treated as approximately equal to the full throughput transmission monitored to be exiting the sample, as light passes through two splices of assumed equal transmission in each case.

Figure A.8 shows two images of a complete LCOF secured to an optical table with Scotch tape and integrated into an optical setup. In later stages of experimentation it was discovered that a large amount of noise and changes in polarization of the light passing through the sample would be incurred if the LCOF were left attached to the poster board used in fabrication and transport. Despite taping all edges of the poster board securely down onto the optical table, minor flexing of the board from small temperature and humidity changes or air drafts in the room caused sufficient instability in the signal to delay successful data collection for the pump-probe experiment (Section 2.4.2).

Over periods of days, some evaporation was inevitable; replenishing the vials every two to three days extended the operational lifetime of the sample. Despite occasional epoxy degradation at the splice site, which might reduce forward transmission, the backscattering experiments remained unaffected except for a loss of forward transmission monitoring. In most cases, weeks-long sample preservation and continued experimentation was feasible with proper maintenance.

A.2 Improvements in Yield and Efficiency of LCOF Samples

A key refinement that greatly improved sample fabrication success rates was the adoption of extremely careful post-splice handling. Previously, standard procedure was to lift the newly spliced fiber assembly without ensuring that each side was completely free of the splicer's grooves. This led to abrupt bending or sudden "snapping" out of the clamp grooves, which almost invariably broke delicate splices that were only partially fused. The implementation of several measures helped to avoid this failure mode. First, folded-paper "sawhorses" and two small Kimwipe boxes on each side of the splice were placed to support the fibers and reduce vibration or flexing. Before switching off the vacuum seal, the clamp latches were gently lifted and small wooden sticks were used to ease the fibers out of the translation/rotation block grooves, ensuring there was no latent twisting or bending. Throughout these steps, the fibers were kept as close as possible to their natural resting position, minimizing stress that would be transferred to the just-completed splice. This careful approach not only reduced the chance of breakage but also allowed for the feasibility of splices that remained sufficiently "open" for CS_2 to enter the hollow core, substantially increasing the proportion of successfully filled samples.

In using the slow-rotation saw to cut and form notches in the glass vial, simple improvements in notch geometry greatly reduced breakage of splices while placing the vial on the slide overtop the delicate splice, and straddling the fibers on either side. Cutting notches to be \sim 1 cm (10-20 times the width of the fiber) reduced the risk of inadvertently contacting the fibers and breaking the delicate splice during vial placement. Additionally, cutting the notches to be shallow (approximately 5 times the width of the fiber) prevented epoxy from running through the notch and sealing the splice. Previous standard procedure were opposite to this geometry as a natural result of the narrow width of the saw blade and the depth to which it could easily be allowed to cut.

A key innovation in the filling procedure was performing a long observation of the filling process for one sample. Previous standard procedure was to stop monitoring after 8 or 12 hours, assuming the fill process had ceased or completed but subsequently reversed if the fluid had not reached the far end by that time. Through extended trials, it was discovered that in successful splices, the fill front progresses at a nonlinear, steadily decreasing rate, and that a one-meter fiber segment might take more than 24 hours to completely fill. In one particularly instructive case, continuous monitoring for 27 hours without leaving the room as a sample filled confirmed that the CS₂ front never reversed; it merely advanced extremely slowly in the final length to reach the other end. Alarms were set for inspection every 90 minutes throughout the night in the final hours of monitoring the sample under the fume hood. Having observed and documented this behavior, the standard practice became allowing the sample to sit undisturbed for at least a full day or more, ensuring the fiber was completely saturated before concluding success or failure. This observation effort and resulting insight halted the regular production of significant waste of both material and time in the fabrication process of LCOF samples.

A final insight that improved the yield of successfully filled samples and mitigation of wasted materials was selecting the “less certain” end of a prepared sample for filling with CS₂. If that splice was sealed, only that end would need to be re-fabricated. Collectively, these simple method improvements in sample fabrication led to significantly shorter fabrication times and dramatically reduced material waste. Hollow-core fibers, which cost on the order of ten dollar per meter, were previously scrapped in large quantities when deemed “dead.” By implementing patient monitoring, careful handling, and mindful filling procedures each length of fiber was used more efficiently, saving significant time and expense while producing more effective samples.

A.3 Tabulated Fit and Uncertainty Values Derived from the Observed Data

A.3.1 Cooling Experiment A Tabulated Values

Table A.1: Measured anti-Stokes parameters for Experiment A. Here P_P is the nominal pump power, measured via a 1% tap just prior to launching into the LCOF, and P_{Intra} is the power actually guided within the fiber. Amplitude, Linewidth, Center, and Offset are the peak spectral density, FWHM linewidth, center frequency, and vertical baseline offset, respectively, obtained from a Lorentzian fit of the data. Uncertainties are 1σ .

P_P (mW)	P_{Intra} (mW)	Amplitude (μV)	Linewidth (MHz)	Center (GHz)	Offset (μV)
10.00	4.12	3.015 ± 0.004	97.3 ± 0.1	2.2690 ± 0.0001	-0.006 ± 0.002
30.00	12.37	8.747 ± 0.006	99.10 ± 0.05	2.2690	0.015 ± 0.002
50.00	20.62	14.22 ± 0.01	99.79 ± 0.04	2.2690	0.032 ± 0.002
70.00	28.86	19.12 ± 0.02	101.15 ± 0.05	2.2690	0.015 ± 0.003
90.00	37.11	24.92 ± 0.01	100.91 ± 0.03	2.2680	0.039 ± 0.003
110.00	45.35	31.27 ± 0.02	102.33 ± 0.03	2.2690	0.029 ± 0.003
130.00	53.60	36.06 ± 0.02	102.45 ± 0.03	2.2690	0.016 ± 0.003
150.00	61.85	41.59 ± 0.02	102.55 ± 0.03	2.2690	0.118 ± 0.003
170.00	70.09	46.78 ± 0.02	103.27 ± 0.03	2.2690	0.086 ± 0.003
190.00	78.34	51.86 ± 0.03	105.02 ± 0.03	2.2690	-0.071 ± 0.004
210.00	86.59	57.04 ± 0.02	105.13 ± 0.03	2.2690	0.058 ± 0.004
230.00	94.83	61.42 ± 0.03	105.63 ± 0.03	2.2690	0.093 ± 0.004
250.00	103.08	66.64 ± 0.04	105.83 ± 0.03	2.2690	0.148 ± 0.005
270.00	111.32	70.63 ± 0.04	106.42 ± 0.04	2.2690	0.205 ± 0.006
290.00	119.57	74.68 ± 0.04	106.32 ± 0.03	2.2690	0.314 ± 0.006

Table A.2: Measured Stokes parameters for Experiment A, in the same format as Table A.1.

P_P (mW)	P_{Intra} (mW)	Amplitude (μV)	Linewidth (MHz)	Center (GHz)	Offset (μV)
10.00	4.12	3.203 ± 0.005	97.3 ± 0.1	2.2690 ± 0.0001	0.020 ± 0.002
30.00	12.37	9.686 ± 0.006	96.82 ± 0.05	2.2680	0.046 ± 0.002
50.00	20.62	15.874 ± 0.009	96.84 ± 0.04	2.2680	0.073 ± 0.002
70.00	28.86	21.87 ± 0.01	96.94 ± 0.04	2.2680	0.066 ± 0.002
90.00	37.11	28.47 ± 0.01	96.40 ± 0.03	2.2680	0.102 ± 0.002
110.00	45.35	37.46 ± 0.02	96.20 ± 0.03	2.2680	0.084 ± 0.003
130.00	53.60	43.36 ± 0.03	96.37 ± 0.03	2.2680	0.023 ± 0.003
150.00	61.85	50.96 ± 0.02	95.04 ± 0.02	2.2680	0.174 ± 0.003
170.00	70.09	57.94 ± 0.03	95.61 ± 0.02	2.2680	0.058 ± 0.003
190.00	78.34	65.46 ± 0.04	95.43 ± 0.03	2.2680	0.029 ± 0.004
210.00	86.59	73.49 ± 0.04	94.59 ± 0.02	2.2680	0.166 ± 0.003
230.00	94.83	81.56 ± 0.04	94.10 ± 0.02	2.2680	0.170 ± 0.004
250.00	103.08	90.64 ± 0.06	92.98 ± 0.03	2.2680	0.272 ± 0.005
270.00	111.32	98.22 ± 0.04	92.67 ± 0.02	2.2680	0.316 ± 0.004
290.00	119.57	107.04 ± 0.05	91.04 ± 0.02	2.2680	0.557 ± 0.006

A.3.2 Cooling Experiment B Tabulated Values

Table A.3: Measured anti-Stokes parameters for Experiment B. Here P_P is the nominal pump power, measured via a 1% tap just prior to launching into the LCOF, P_{Intra} is the power actually guided within the fiber, and P_{Pr} is the probe power, also measured just prior to launching into the LCOF. Amplitude, Linewidth, Center, and Offset are the peak spectral density, FWHM linewidth, center frequency, and vertical baseline offset, respectively, obtained from a Lorentzian fit of the data. Uncertainties are 1σ .

P_P (mW)	P_{Intra} (mW)	P_{Pr} (mW)	Amplitude (μV)	Linewidth (MHz)	Center (GHz)	Offset (μV)
0.00	0.00	10.00	1.849 ± 0.002	96.6 ± 0.2	2.2700	0.0230 ± 0.0009
55.00	22.68	10.00	1.640 ± 0.007	104.0 ± 0.5	2.2710 ± 0.0001	0.019 ± 0.001
110.00	45.35	10.00	1.53 ± 0.01	106.9 ± 0.8	2.2710 ± 0.0002	0.020 ± 0.002
165.00	68.03	10.00	1.43 ± 0.01	110 ± 1	2.2700 ± 0.0003	0.028 ± 0.002

Appendix B

Supplementary Information for Chapter 3

B.1 Coupled-Wave Equations

Here we derive the coupled wave equations that describe coherent stimulated Brillouin scattering involving a pump, Stokes, probe, and backscattered optical field given respectively by

$$\tilde{E}_P(z, t) = A_P e^{i(k_P z - \omega_P t)} + c.c., \quad (\text{B.1})$$

$$\tilde{E}_S(z, t) = A_S e^{i(-k_S z - \omega_S t)} + c.c., \quad (\text{B.2})$$

$$\tilde{E}_{Pr}(z, t) = A_{Pr} e^{i(k_{Pr} z - \omega_{Pr} t)} + c.c., \quad (\text{B.3})$$

$$\tilde{E}_{Sig}(z, t) = A_{Sig} e^{i(-k_{Sig} z - \omega_{Sig} t)} + c.c., \quad (\text{B.4})$$

and a common acoustic field given by

$$\tilde{\rho}(z, t) = \rho_0 + \rho(z, t) e^{i(qz - \Omega t)} + c.c., \quad (\text{B.5})$$

where $\Omega = \omega_P - \omega_S$ and $q = k_P - k_S \approx 2k_P$.

B.1.1 Acoustic Field

As in the case of SBS³, we start by assuming that the material obeys the acoustic wave equation,

$$\frac{\partial^2 \tilde{\rho}}{\partial t^2} - \Gamma' \nabla^2 \frac{\partial \tilde{\rho}}{\partial t} - v_s^2 \nabla^2 \tilde{\rho} = \nabla \cdot \vec{f}, \quad (\text{B.6})$$

where v_s is the sound speed in the material and Γ' is a damping parameter given by

$$\Gamma' = \frac{1}{\rho} \left[\frac{4}{3} \eta_s + \eta_b + \frac{\kappa}{C_p} (\gamma - 1) \right], \quad (\text{B.7})$$

where η_s and η_b are the shear and bulk viscosity coefficients of the material, respectively. The source term on the right side of Equation B.6 is the divergence of the electrostrictive force:

$$\vec{f} = \nabla p_{st} = \nabla \cdot \left[-\frac{1}{2} \epsilon_0 \gamma_e \left(\langle \tilde{E}_P \cdot \tilde{E}_S \rangle + \langle \tilde{E}_{Pr} \cdot \tilde{E}_{Sig} \rangle \right) \right], \quad (\text{B.8})$$

which yields, assuming the acoustic wave varies slowly in time,

$$\nabla \cdot \vec{f} = \epsilon_0 \gamma_e q^2 (A_P A_S^* + A_{Pr} A_{Sig}^*) e^{i \Delta k z}, \quad (\text{B.9})$$

where $\Delta k = (k_{Pr} - k_{Sig}) - (k_P - k_S)$ is the phase mismatch between the four optical fields. Only two electrostrictive terms survive after accounting for the orthogonal polarization of the pump and Stokes fields with respect to that of the probe and backscattered signal. Inserting this electrostrictive force term (Equation B.9) and the acoustic field (Equation B.5) into the acoustic wave equation (Equation B.6), we find

$$-2i\Omega \frac{\partial \rho}{\partial t} - \Gamma' 2iq^2 \Omega \rho - 2iqv_s^2 \frac{\partial \rho}{\partial z} = \epsilon_0 \gamma_e q^2 (A_P A_S^* + A_{Pr} A_{Sig}^*) e^{i \Delta k z}, \quad (\text{B.10})$$

which can be restated in terms of the Brillouin linewidth, $\Gamma_B = q^2 \Gamma'$, as

$$-2i\Omega \frac{\partial \rho}{\partial t} - 2i\Omega \Gamma_B \rho - 2iqv_s^2 \frac{\partial \rho}{\partial z} = \epsilon_0 \gamma_e q^2 (A_P A_S^* + A_{Pr} A_{Sig}^*) e^{i \Delta k z}. \quad (\text{B.11})$$

Given the phonon dispersion relations $\Omega_B = |q_B|v_s$ and $\Omega^2 = q^2(v_s^2 - i\Omega\Gamma')$, Equation B.11 can be rewritten as

$$-2i\Omega \frac{\partial \rho}{\partial t} + (\Omega_B^2 - \Omega^2 - i\Omega\Gamma_B) \rho - 2iqv_s^2 \frac{\partial \rho}{\partial z} = \epsilon_0 \gamma_e q^2 (A_P A_S^* + A_{Pr} A_{Sig}^*) e^{i\Delta kz}. \quad (\text{B.12})$$

We take the common assumption that the phonon propagation distance is small compared to the distance over which the source term varies significantly, which allows the spatial derivative term in Equation B.12 to be dropped. We further assume steady-state conditions such that the time derivative term also vanishes, leaving

$$(\Omega_B^2 - \Omega^2 - i\Omega\Gamma_B) \rho = \epsilon_0 \gamma_e q^2 (A_P A_S^* + A_{Pr} A_{Sig}^*) e^{i\Delta kz}. \quad (\text{B.13})$$

We thus find the acoustic field amplitude to be

$$\rho(z, t) = \epsilon_0 \gamma_e q^2 \frac{(A_P A_S^* + A_{Pr} A_{Sig}^*) e^{i\Delta kz}}{\Omega_B^2 - \Omega^2 - i\Omega\Gamma_B}. \quad (\text{B.14})$$

B.1.2 Optical Fields

We now turn to the spatial evolution of the optical fields, described by the wave equation,

$$\frac{\partial^2 \tilde{E}_i}{\partial z^2} - \frac{n^2}{c^2} \frac{\partial^2 \tilde{E}_i}{\partial t^2} = \frac{1}{\epsilon_0 c^2} \frac{\partial^2 \tilde{P}_i}{\partial t^2}, \quad (\text{B.15})$$

where i denotes the four optical fields, namely: pump, Stokes, probe, and the backscattered signal. The total nonlinear polarization that gives rise to the source term in the wave Equation is given by

$$\tilde{P} = \epsilon_0 \Delta \chi \tilde{E} = \epsilon_0 \Delta \epsilon \tilde{E} = \epsilon_0 \rho^{-1} \gamma_e \tilde{\rho} \tilde{E}. \quad (\text{B.16})$$

The parts of \tilde{P} that can act as phase-matched source terms for the optical fields are

$$\tilde{P}_P = p_P e^{i(k_P z - \omega_P t)} + c.c. = \frac{1}{2} \epsilon_0 \rho_0^{-1} \gamma_e \rho A_S e^{i(k_P z - \omega_P t)}, \quad (\text{B.17})$$

$$\tilde{P}_S = p_S e^{i(-k_S z - \omega_S t)} + c.c. = \frac{1}{2} \epsilon_0 \rho_0^{-1} \gamma_e \rho^* A_P e^{i(-k_S z - \omega_S t)}, \quad (\text{B.18})$$

$$\tilde{P}_{Pr} = p_{Pr} e^{i(k_{Pr} z - \omega_{Pr} t)} + c.c. = \frac{1}{2} \epsilon_0 \rho_0^{-1} \gamma_e \rho A_{Sig} e^{i(k_{Pr} z - \omega_{Pr} t)} e^{i\Delta kz}, \quad (\text{B.19})$$

$$\tilde{P}_{Sig} = p_{Sig} e^{i(-k_{Sig} z - \omega_{Sig} t)} + c.c. = \frac{1}{2} \epsilon_0 \rho_0^{-1} \gamma_e \rho^* A_{Pr} e^{i(-k_{Sig} z - \omega_{Sig} t)} e^{-i\Delta kz}. \quad (\text{B.20})$$

Inserting the optical fields (Equations B.1-B.4) and phase-matched source terms (Equations B.17-B.20) into Equation B.15, we obtain

$$\frac{\partial A_P}{\partial z} + \frac{n}{c} \frac{\partial A_P}{\partial t} = \frac{i\omega_P \gamma_e}{2nc\rho_0} \rho A_2, \quad (\text{B.21})$$

$$-\frac{\partial A_S}{\partial z} + \frac{n}{c} \frac{\partial A_S}{\partial t} = \frac{i\omega_S \gamma_e}{2nc\rho_0} \rho^* A_P, \quad (\text{B.22})$$

$$\frac{\partial A_{Pr}}{\partial z} + \frac{n}{c} \frac{\partial A_{Pr}}{\partial t} = \frac{i\omega_{Pr} \gamma_e}{2nc\rho_0} \rho A_{Sig}, \quad (\text{B.23})$$

$$-\frac{\partial A_{Sig}}{\partial z} + \frac{n}{c} \frac{\partial A_{Sig}}{\partial t} = \frac{i\omega_{Sig} \gamma_e}{2nc\rho_0} \rho^* A_{Pr}, \quad (\text{B.24})$$

We again assume steady-state conditions, allowing the time derivative term to be dropped. Plugging in the acoustic field amplitude (Equation B.14), we arrive at the coupled-amplitude wave equations for the optical fields,

$$\frac{\partial A_P}{\partial z} = \frac{i\epsilon_0 \omega_P q^2 \gamma_e^2}{2nc\rho_0} \frac{(A_P |A_S|^2 + A_{Pr} A_{Sig}^* A_S) e^{i\Delta kz}}{\Omega_B^2 - \Omega^2 - i\Omega\Gamma_B}, \quad (\text{B.25})$$

$$\frac{\partial A_S}{\partial z} = -\frac{i\epsilon_0\omega_S q^2 \gamma_e^2}{2nc\rho_0} \frac{(|A_P|^2 A_S^* + A_{Pr} A_{Sig}^* A_P) e^{-i\Delta kz}}{\Omega_B^2 - \Omega^2 + i\Omega\Gamma_B}, \quad (\text{B.26})$$

$$\frac{\partial A_{Pr}}{\partial z} = \frac{i\epsilon_0\omega_{Pr} q^2 \gamma_e^2}{2nc\rho_0} \frac{(A_P A_S^* A_{Sig} + A_{Pr} |A_{Sig}|^2) e^{i\Delta kz}}{\Omega_B^2 - \Omega^2 - i\Omega\Gamma_B}, \quad (\text{B.27})$$

$$\frac{\partial A_{Sig}}{\partial z} = -\frac{i\epsilon_0\omega_{Sig} q^2 \gamma_e^2}{2nc\rho_0} \frac{(A_P A_S^* A_{Pr} + |A_{Pr}|^2 A_{Sig}^*) e^{-i\Delta kz}}{\Omega_B^2 - \Omega^2 + i\Omega\Gamma_B}. \quad (\text{B.28})$$

We drop the very small signal amplitude terms on the right side of Equations B.25-B.28 and integrate each along the effective length to get the amplitudes,

$$A_P = \frac{i\epsilon_0\omega_P q^2 \gamma_e^2}{2nc\rho_0} \frac{|A_P|^2}{\Omega_B^2 - \Omega^2 - i\Omega\Gamma_B} \frac{e^{i\Delta k L} - 1}{i\Delta k}, \quad (\text{B.29})$$

$$A_S = -\frac{i\epsilon_0\omega_S q^2 \gamma_e^2}{2nc\rho_0} \frac{|A_P|^2 A_S^*}{\Omega_B^2 - \Omega^2 + i\Omega\Gamma_B} \frac{e^{-i\Delta k L} - 1}{-i\Delta k}, \quad (\text{B.30})$$

$$A_{Pr} = \frac{i\epsilon_0\omega_{Pr} q^2 \gamma_e^2}{2nc\rho_0} \frac{A_P A_S^* A_{Sig}}{\Omega_B^2 - \Omega^2 - i\Omega\Gamma_B} \frac{e^{i\Delta k L} - 1}{i\Delta k}, \quad (\text{B.31})$$

$$A_{Sig} = -\frac{i\epsilon_0\omega_{Sig} q^2 \gamma_e^2}{2nc\rho_0} \frac{A_P A_S^* A_{Pr}}{\Omega_B^2 - \Omega^2 + i\Omega\Gamma_B} \frac{e^{-i\Delta k L} - 1}{-i\Delta k}. \quad (\text{B.32})$$

We focus on the signal amplitude given by Equation B.32, noting that close to resonance, the denominator of the middle term containing Ω can be approximated as,

$$\Omega_B^2 - \Omega^2 + i\Omega\Gamma_B \approx \Omega_B(\Omega - \Omega_B + i\Gamma_B), \quad (\text{B.33})$$

giving

$$A_{Sig} = -\frac{i\epsilon_0\omega_{Sig}q^2\gamma_e^2}{2nc\rho_0} \frac{A_PA_S^*A_{Pr}}{\Omega_B(\Omega - \Omega_B + i\Gamma_B)} \frac{e^{-i\Delta k L} - 1}{-i\Delta k}, \quad (\text{B.34})$$

and in fact on resonance the expression reduces to

$$A_{Sig} = -\frac{i\epsilon_0\omega_{Sig}q^2\gamma_e^2}{2nc\rho_0} \frac{A_PA_S^*A_{Pr}}{\Omega_B i\Gamma_B} \frac{e^{-i\Delta k L} - 1}{-i\Delta k}. \quad (\text{B.35})$$

Using $q = 2k_P = 2\omega n/c$ and $q = \Omega_B/v_s$, we can express the leading terms as

$$A_{Sig} = -\frac{\epsilon_0\omega^2\gamma_e^2}{c^2v_s\rho_0\Gamma_B} A_PA_S^*A_{Pr} \frac{e^{-i\Delta k L} - 1}{-i\Delta k}, \quad (\text{B.36})$$

where we have dropped the signal designator on ω . Defining the Brillouin gain factor, g_0 , as Boyd does,

$$g_0 = \frac{\gamma_e^2\omega^2}{nv_s c^3 \rho_0 \Gamma_B}, \quad (\text{B.37})$$

reduces this expression to

$$A_{Sig} = -\epsilon_0 nc g_0 A_PA_S^*A_{Pr} \frac{e^{-i\Delta k L} - 1}{-i\Delta k}. \quad (\text{B.38})$$

The intensity of the backscattered signal is given by the magnitude of the time-averaged Poynting vector, given by

$$I_i = 2n\epsilon_0 c |A_i|^2, \quad i = 1, 2, 3, \dots \quad (\text{B.39})$$

which produces for the signal intensity

$$I_{Sig} = 2\epsilon_0 nc (\epsilon_0 nc g_0)^2 |A_P|^2 |A_S^*|^2 |A_{Pr}|^2 \left| \frac{e^{-e\Delta k L} - 1}{-i\Delta k} \right|^2 = 2\epsilon_0^3 \epsilon_0 n^3 c^3 g_0^2 \frac{I_P}{2\epsilon_0 nc} \frac{I_S}{2\epsilon_0 nc} \frac{I_{Pr}}{2\epsilon_0 nc} \left| \frac{e^{-e\Delta k L} - 1}{-i\Delta k} \right|^2. \quad (\text{B.40})$$

The squared modulus term containing Δk can be reduced as

$$\begin{aligned} \left| \frac{e^{-i\Delta k L} - 1}{-i\Delta k} \right|^2 &= \frac{(e^{-i\Delta k L} - 1)(e^{i\Delta k L} - 1)}{(\Delta k)^2} = \frac{L^2}{(\Delta k L)^2} \left[2 - 2 \left(\frac{e^{i\Delta k L} + e^{-i\Delta k L}}{2} \right) \right] \\ &= \frac{2L^2(1 - \cos \Delta k L)}{(\Delta k L)^2} = \frac{4L^2 \sin^2 \left(\frac{\Delta k L}{2} \right)}{(\Delta k L)^2} = \frac{L^2 \sin^2 \left(\frac{\Delta k L}{2} \right)}{\left(\frac{\Delta k L}{2} \right)^2} = L^2 \operatorname{sinc}^2 \left(\frac{\Delta k L}{2} \right), \end{aligned} \quad (\text{B.41})$$

giving as a final expression for backscattered signal intensity,

$$I_{Sig} = \frac{1}{4}(g_0 L)^2 I_P I_S I_{Pr} \operatorname{sinc}^2 \left(\frac{\Delta k L}{2} \right). \quad (\text{B.42})$$

To find the power of the backscattered signal, we would integrate this intensity over the effective area. For a uniform area A_{eff} , this gives

$$P_{Sig} = I_{Sig} A_{eff} = \frac{1}{4}(g_0 L)^2 \frac{A_{eff}}{A_{eff}} I_P \frac{A_{eff}}{A_{eff}} I_S \frac{A_{eff}}{A_{eff}} I_{Pr} \operatorname{sinc}^2 \left(\frac{\Delta k L}{2} \right) A_{eff}, \quad (\text{B.43})$$

or,

$$P_{Sig} = \frac{1}{4}(G_B L)^2 P_P P_S P_{Pr} \operatorname{sinc}^2 \left(\frac{\Delta k L}{2} \right), \quad (\text{B.44})$$

where,

$$G_B = \frac{g_0}{A_{eff}}. \quad (\text{B.45})$$

It can be seen that off resonance, the Ω term from Equation B.34 goes to a lorentzian form after taking the squared modulus for intensity.

B.2 Scattered Power Comparison to Traditional Brillouin Scattering Processes

This appendix provides a comparative analysis of the scattered power produced by our instrument to that of standard Brillouin scattering processes—that is, spontaneous and stimulated Brillouin scattering. The difference in behavior of our instrument from the traditional techniques arises due to the coherent stimulation of the acoustic mode by the pump and Stokes fields, producing a 4-wave-coupled-amplitude interaction that yields much higher scattered powers in smaller lengths. While our instrument is particularly well suited to small interaction lengths due to enhanced phase-matching relaxation, it maintains production of a significant amount of scattered power at greater lengths as well (greater than 1 m). This is because the reduction in scattered power from the breakdown of phase-matching relaxation at greater lengths is perfectly counterbalanced by the quadratic dependence on length in the overall scattered power, as seen in Equation 3.1. At very large lengths (greater than 1 km), the instrument is ultimately limited by the coherence length of the lasers employed, as the process relies on the coherent stimulation of the phonon mode and thus the mutual coherence of the pump and Stokes fields over the interaction length. Here we offer an exploration into the respective performance of each technique across the entire meaningful length scale, from nanometers to kilometers.

Despite shared dependence on basic Brillouin scattering principles, the three techniques compared here (spontaneous-, stimulated-, and coherently stimulated Brillouin scattering) yield significantly different scattered power for identical experimental parameters. At small lengths, the high-gain threshold for optical stimulation of the material fluctuations is often not achievable without the use of extremely large optical powers. This prevents the system from entering a process of exponential growth of the scattered Stokes light indicative of stimulated Brillouin scattering.³ In this low-gain regime, any scattered Stokes light is spontaneously scattered from thermal fluctuations of the material, or from quantum-mechanical fluctuations of materials at the ground state. The low-gain regime is defined by an overall process gain factor, denoted by $G = G_P P_P L$, which is much less than unity ($G \ll 1$). Here, G_B is the effective Brillouin gain in $\text{W}^{-1} \text{m}^{-1}$ ($G_B = \frac{g}{A_{\text{eff}}}$), P_P is the pump power, and L is the effective length. This spontaneous scattering process follows a linear growth trend described by Boyd et al in 1990¹⁰⁹ as

$$R = \frac{\langle |E_S|^2 \rangle}{\langle |E_P|^2 \rangle} = (\bar{n} + 1)g\hbar\omega_S\Gamma_B \frac{L}{4A_{\text{eff}}}, \quad (\text{B.46})$$

where R is the reflectivity, or the ratio of scattered Stokes intensity to incident pump intensity, and $\bar{n} = (e^{\frac{\hbar\Omega_B}{k_B T}} - 1)^{-1}$ is the mean number of phonons occupying the mode due to thermal fluctuations of the material. Rearranging this Equation and converting to effective Brillouin gain, G_B , and power by applying the effective area, we arrive at the scattered power of the Stokes spontaneous Brillouin scattering process,

$$P_S = \frac{1}{4} G_B P_P L \hbar \omega_S \Gamma_B (\bar{n} + 1). \quad (\text{B.47})$$

At room temperature and typical Brillouin frequencies in the GHz range, the quantity $k_B T \gg \hbar \Omega_B$, allowing

$$e^{\frac{\hbar \Omega_B}{k_B T}} \approx 1 + \frac{\hbar \Omega_B}{k_B T} \quad (\text{B.48})$$

to be a good approximation. We thus find that

$$(\bar{n} + 1) \approx \bar{n} \approx \frac{k_B T}{\hbar \Omega_B}. \quad (\text{B.49})$$

Inserting this reduced quantity into Equation B.47, we arrive at a convenient expression for the scattered power of the Stokes spontaneous Brillouin scattering process,

$$P_{S, SpontBS} = \frac{G_B P_P L \omega_S \Gamma_B k_B T}{4 \Omega_B}. \quad (\text{B.50})$$

It may be noted that the derived expression for the low-gain spontaneous regime here matches the form reported by Kharel et al. in 2016¹¹⁰ for the complementary forward scattering process. While our backward scattering geometry differs from the forward scattering geometry discussed by Kharel et al., the underlying physics of light coupling to thermally excited acoustic modes is the same..

Next we turn to the high-gain regime leading to a stimulated Brillouin scattering process. This regime is defined by an overall process gain factor, $G = G_P P_P L$, that is much greater than unity ($G \gg 1$). For organic liquids, this crossover threshold from spontaneous to stimulated regimes occurs in the range of $20 < G < 25$,¹⁰⁹ whereas for typical lengths of single mode fiber it can be lower³⁴ owing to the small effective area compared to longer effective lengths of fiber typically used.

The reflectivity of a stimulated Brillouin scattering process in the high-gain regime is given by¹⁰⁹

$$R = \frac{\langle |E_S|^2 \rangle}{\langle |E_P|^2 \rangle} = \frac{Y}{\sqrt{\pi}} \frac{e^G}{G^{\frac{3}{2}}}, \quad (\text{B.51})$$

where Y is the reflectivity of the low-gain (spontaneous) regime given above and G is the overall process gain factor, $G = G_P P_P L$. Again, converting to the effective Brillouin gain, G_B , and power by applying the effective area, we solve for the scattered power of the Stokes field,

$$P_{S, StimBS} = \frac{G_B P_P L \omega_S \Gamma_B k_B T}{4 \sqrt{\pi} \Omega_B} \frac{e^G}{G^{\frac{3}{2}}} \quad (\text{B.52})$$

This expression captures the exponential growth in scattered power as any parameter within the overall process gain factor, $G = G_B P_P L$, increases. However, this exponential growth can only continue while the pump is not significantly undepleted. Once the scattered power described by Equation B.52 grows to a significant fraction of the driving pump power, the exponential increase in scattered Stokes power asymptotically approaches the pump power. For very large G , virtually all of the pump energy is converted to scattered Stokes energy in a complete transfer process.³ To account for pump depletion, we numerically solve the transcendental Equation derived in Boyd's Nonlinear Optics which describes the effects of pump depletion, given here in terms of power as

$$P_S(L) = \frac{P_S(0)x(1-x)}{e^{G_B P_P(0)L(1-x)} - x}, \quad (\text{B.53})$$

where $x = P_S(0)/P_P(0)$, or the ratio of the unknown Stokes power at the end of its journey through the medium ($z = 0$) to the known pump power at the beginning (also $z = 0$). This solution for x , specific to system parameters such as length, offers via its definition the solution to the unknown power of the scattered Stokes light at the end of its traversal through the effective length, given as

$$P_S(0) = xP_P(0). \quad (\text{B.54})$$

The solution to this numeric approach to scattered power in the high-gain (stimulated) Brillouin scattering regime with pump depletion effects at large G is plotted for varying effective lengths in Figure B.1, along with the analytical solutions derived previously for the low-gain (spontaneous) regime and our coherently stimulated Brillouin spectrometer given by Equation 3.1. System parameters used to generate the plot for each of the three processes are provided in Tables B.1 and B.2. Wherever possible, the parameters shared by all three Brillouin scattering processes were kept consistent, while quantities unique to each process were assigned their respective values.

Table B.1: Parameters relevant to the coherently stimulated backward Brillouin scattering process for the example Ultra High Numerical Aperture 3 (UHNA3) fiber. G_B is the effective Brillouin gain, P_P is the pump power, P_S is the Stokes power, P_{Pr} is the probe power, and $\Delta\lambda$ is the wavelength detuning of the probe from the pump.

<u>Coherently Stimulated Brillouin Scattering Process Model System Parameters</u>				
G_B (W $^{-1}$ m $^{-1}$)	P_P (W)	P_S (W)	P_{Pr} (W)	$\Delta\lambda$ (pm)
0.6	1	1	1	20

At lengths beyond a centimeter, the phase-matching relaxation of the coherently stimulated process begins

Table B.2: Parameters relevant to the spontaneous and/or stimulated backward Brillouin scattering processes for the example UHNA3 fiber. G_B is the Brillouin gain coefficient, P_P is the pump power, ω is the optical angular frequency, Γ_B is the acoustic damping rate, k_B is Boltzmann's constant, T is the temperature, and Ω_B is the acoustic angular frequency.

Spontaneous and Stimulated Scattering Process Model System Parameters								
G_B (W $^{-1}$ m $^{-1}$)	P_P (W)	$P_{S,seed}$ (pW)	n	λ_P (MHz)	Γ_B (J K $^{-1}$)	k_B (K)	T (GHz)	Ω_B
0.6	1	1	1.48	1549	$2\pi \cdot 80$	1.38×10^{-23}	295	$2\pi \cdot 9.18$

to break down, and the specific choice in pump and probe detuning becomes critical. This corresponds to a narrowing of the sinc^2 function given in Equation 3.5. The scattered power beyond this length rises and falls according to the oscillations of the sinc^2 function far from the origin. As length increases continuously beyond 1 m, the scattered power oscillates with increasing frequency and ceases to offer practical significance. To better visualize the scattered power offered by the instrument in this region, we have computed the envelope of scattered power. In a laboratory setting, the appropriate pump and probe detuning would be selected for the specific sample length being measured such that the scattered power function lies on a local peak of the sinc^2 function.

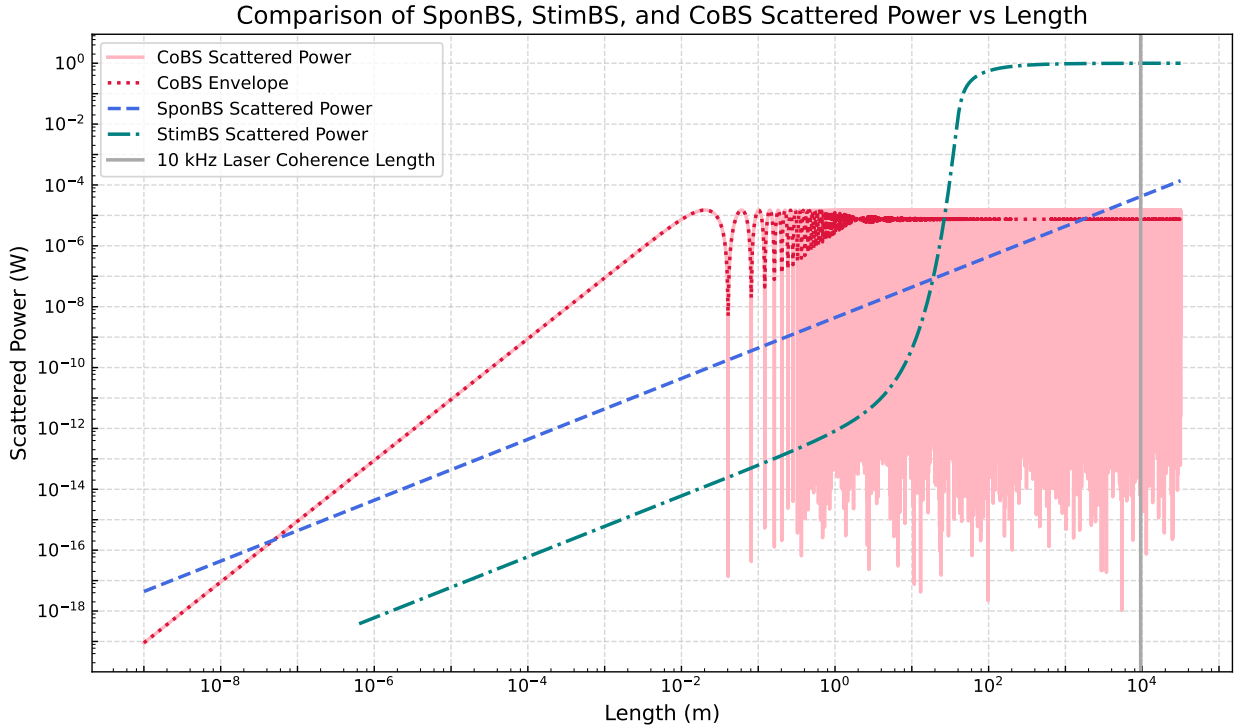


Figure B.1: Comparison of scattered power from a spontaneous Brillouin scattering process and our coherently stimulated Brillouin spectrometer.

Figure B.1 shows the advantage that our coherently stimulated Brillouin spectrometer offers compared to the traditional Brillouin processes for the example medium of UHNA3 fiber. For lengths up to about 50 m and down to as low as 100 nm, the coherently stimulated process employed by our instrument offers superior scattered power, with the relative advantage peaking for a length just under 1 cm. At this length, the gain factor G places the traditional process within the low-gain (spontaneous) regime, and thus the scattered power generated is only on the order of 10s of pW. In contrast, the scattered power for the same system offered by our instrument is on the order of 10s of μ W, exceeding that of the spontaneous process by a factor of a million. This is, of course, the most ideal case for this system, however it can be seen from Figure B.1 that the coherently stimulated process offers orders of magnitude more scattered power than either traditional process through a wide range of lengths.

B.3 Observance of Fano-Resonant Asymmetries at Small Signals

In *Fano-Resonant Asymmetries at Small Signals* (Section 3.5.4 in the main text), we discussed how Fano-type interference can distort Brillouin line shapes in situations where the resonant Brillouin amplitude becomes comparable to the background continuum. We focus here on two experiments (A and B) that reveal these Fano asymmetries especially clearly. Experiment A is a measurement series using the same 1 cm UHNA3 fiber referenced in the main discussion, for which the main text showed only the fitted amplitudes (Figure 3.6). Here we show the full spectra, illustrating the emergence of asymmetries at lower amplitude conditions. Experiment B is a distinct measurement involving a short (~ 1 mm) bulk liquid sample of carbon disulfide (CS_2) that we briefly mentioned in Section 3.5.4 but did not detail. This experiment was performed specifically to further probe the unexpected Fano-like distortions observed in Experiment A. In each case, we outline the experimental setup, present the spectra, and highlight the appearance of Fano resonances. These observations corroborate the theoretical discussion of Fano line shapes (Section 3.5.4) and provide insight into when and why they are most prominent.

B.3.1 Fano Experiment A: Extended 1 cm UHNA3 Fiber Spectra

In Section 3.5 of the main text, we introduced a phase-matching experiment on 1 cm of UHNA3 fiber in which the pump-probe detuning was varied from 5 GHz to 42 GHz in 0.5 GHz increments. There, we reported only the resulting peak amplitudes, showing how they follow a sinc^2 dependence on detuning (Figure 3.6 in the main text). However, each measurement in that scan also yields a full Brillouin spectrum—75 in total. Here, we present all 75 spectra to illustrate how the line shape transitions from nearly Lorentzian (when the Brillouin peak amplitude greatly exceeds the background continuum) to distinctly Fano-like (when the two amplitudes are comparable). We used the same setup and procedure described in *Phase Matching Characterization* in Section 3.5 of the main text. As the pump-probe detuning increases, the phase-matching term $\text{sinc}^2(\Delta kL/2)$ oscillates through peaks and troughs, causing the Brillouin peak amplitude to rise and fall. When the amplitude is sufficiently large, the Brillouin mode dominates the continuum and the spectrum appears nearly Lorentzian; when it drops to the order of the background amplitude, strong interference skews the line shape into a Fano-like profile.

Figure B.2 highlights the progressive shift from Lorentzian to asymmetric line shapes. Near 5 GHz detuning (top spectra), the resonant amplitude is large relative to the background, giving a classic Lorentzian peak ($|q| \rightarrow \infty$) at the resonance frequency (~ 9.17 GHz). By contrast, at detunings between ~ 15 - 20 GHz, where the sinc^2 factor is near a local minimum, the peak amplitude falls to roughly the same level as the continuum, and Fano interference is observed. Interestingly, as the detuning is increased further, and the

amplitude rises again on a subsequent “lobe” of the sinc^2 function, the spectra partly recover a Lorentzian shape. This cyclical behavior persists, with each local maximum yielding a near-Lorentzian profile and each local minimum reintroducing a strong Fano distortion. These observations confirm the relationship between Brillouin peak amplitude and continuum interference described in *Fano-Resonant Asymmetries at Small Signals* in Section 3.5. When the Brillouin amplitude significantly exceeds the background, the discrete phonon resonance dominates, resulting in little or no asymmetry ($|q| \rightarrow \infty$). Once the two amplitudes become comparable, Fano interference skews the line shape, shifting the apparent peak frequency slightly and altering the slope on either side of the resonance. Analyzing selected spectra with both Lorentzian and Fano fits indicates that ignoring these distortions can lead to up to a 5–10% misestimation of peak amplitude in the “trough” (low-amplitude) sets. This underscores the importance of employing a Fano model in small-signal measurements where the Brillouin peak may not tower over the background. A comparative analysis of a Lorentzian vs. Fano fit function applied to highly assymetric spectra is explored in the following section, for data gathered from Experiment B.

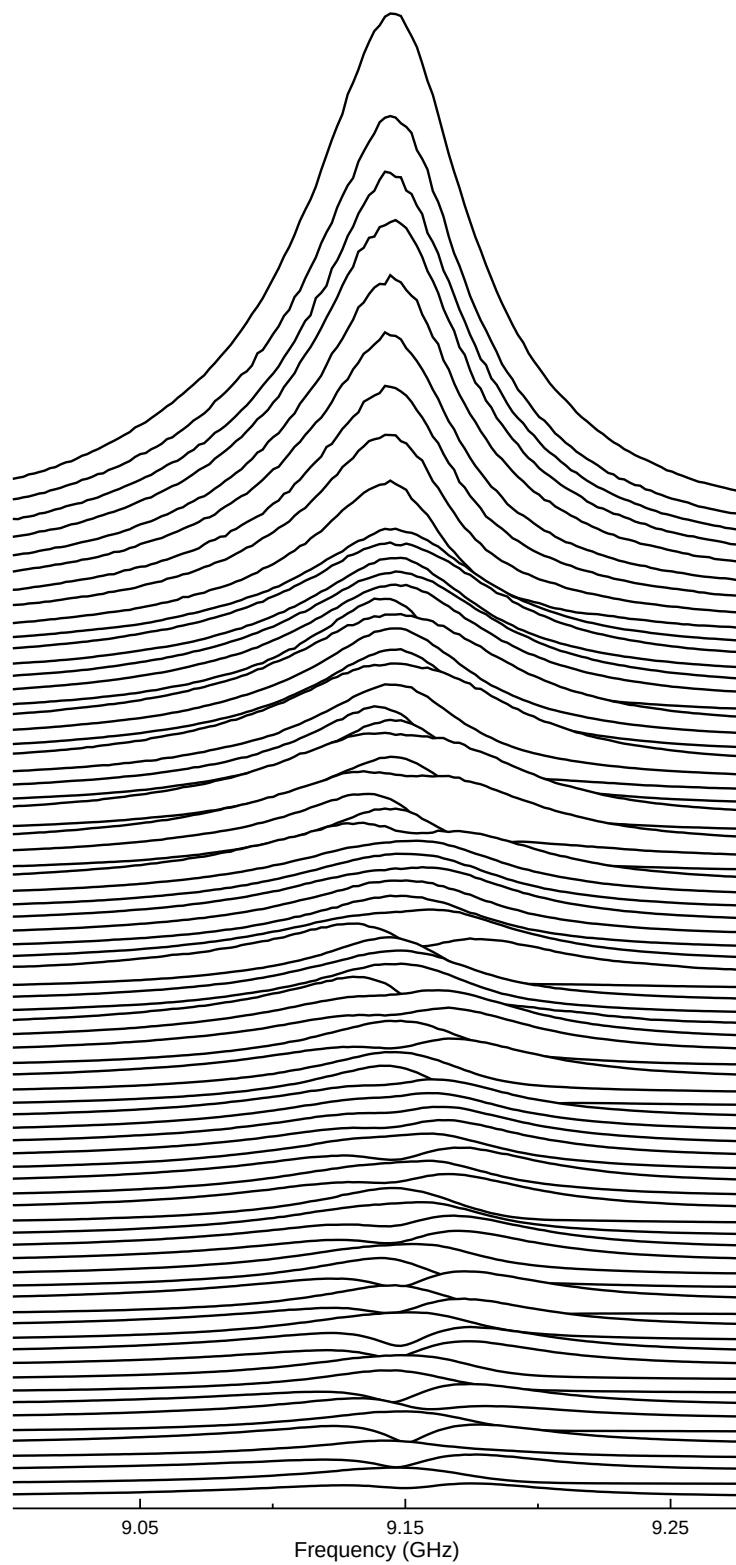


Figure B.2: All measured Brillouin spectra for 1 cm UHNA3 at detuning steps of 0.5 GHz from 5 GHz (top spectrum) to 42 GHz (bottom spectrum). Each trace is offset for clarity. The resulting asymmetries highlight the characteristic Fano-resonant behavior under low signal conditions.

B.3.2 Fano Experiment B: 1 mm CS₂ Spectra and Fano Distortions

We now turn to measurements on a 1 mm-thick cell of CS₂ in a free-space geometry, complementing the 1 cm UHNA3 fiber results (Experiment A). Both experiments used comparable sub-Watt optical powers (on the order of \sim 60–70 mW pump, \sim 25–30 mW Stokes, and \sim 40–50 mW probe). However, unlike Experiment A, which probed a 1 cm fiber with 0.5 GHz detuning increments from 5 GHz to 42 GHz, here the detuning is stepped in 0.25 GHz increments between 10 GHz and 14 GHz. Because the CS₂ sample is an order of magnitude shorter (1 mm vs. 1 cm), its phase-matching bandwidth (sinc² profile) is roughly ten times wider, making these 0.25 GHz steps effectively twenty times finer than the 0.5 GHz steps used in the fiber experiment. This reduced range of detunings within a broader sinc² profile produce measured peaks all of similar amplitude to one another, as opposed to the dynamic evolution of peaks in the 1 cm UHNA3 fiber data.

Figure B.3 shows all 17 spectra obtained at detuning increments of 0.25 GHz, presented in order of increasing detuning from top spectrum to bottom spectrum. Each trace is offset vertically for clarity, with the topmost spectrum corresponding to 10 GHz and the bottom spectrum corresponding to 14 GHz detuning of the pump and the probe. A change in the detuning of the pump and probe via adjustment of the probe laser wavelength produces a change in phase of the resonant Brillouin signal. This changing resonant Brillouin phase relative to the background continuum produces spectra with different Fano-resonant distortions corresponding to specific values of the Fano parameter, q , as discussed in *Fano-Resonant Asymmetries at Small Signals* in the main text (Section 3.5.4). Fano-resonant asymmetries are seen in nearly every spectrum of this liquid experiment, indicating that the background continuum is competing strongly with the Brillouin amplitude in all measurements.

The Brillouin amplitudes featured in this experiment are an order of magnitude lower compared to the highest amplitudes seen in Experiment A. This is caused by the order of magnitude shorter sample length of CS₂ (1 mm) as compared to the 1 cm length of UHNA3 fiber used in Experiment A. The \sim 1000 times higher Brillouin gain offered by the CS₂ (1.5 m GW^{-1}) is discounted significantly by the \sim 350 times larger effective area offered by the beam waist in the free-space optical setup compared to the core of UHNA3 fiber used in Experiment A ($\sim 17 \mu\text{m}$ radius beam waist vs. $\sim 0.9 \mu\text{m}$ radius core of UHNA3). The effective Brillouin gain of the CS₂ used in Experiment B is thus a net ~ 3 times greater than that of the UHNA3 fiber. From Equations 3.1 and 3.2 in the main text, scattered power scales with the square of both the length and the effective Brillouin gain of the sample ($P_{S\text{ig}} \propto L^2 G_B^2$). Cumulatively, this makes for an approximate order-of-magnitude signal reduction for similar optical powers and pump-probe detuning.

However, both experiments (A and B) feature a sweep through a range of pump-probe detunings, with Experiment B featuring a step size effectively 25 times finer than that of Experiment A. This further cor-

robicates these two data sets, as the signal reduction from near-center peak to a side trough of the sinc^2 profile is also on the order of a 10 times reduction (Figure 3.6). This places the signal amplitudes of the CS_2 spectra from Experiment B (all near *peak-center* of its sinc^2 profile) on the same order as the signal amplitudes near the *troughs* of the UHNA3 fiber spectra from Experiment A. These spectra all share strong Fano asymmetries, indicating as they should that they all sit in a similar signal amplitude range: small enough that the background continuum competes but does not dominate over the signal.

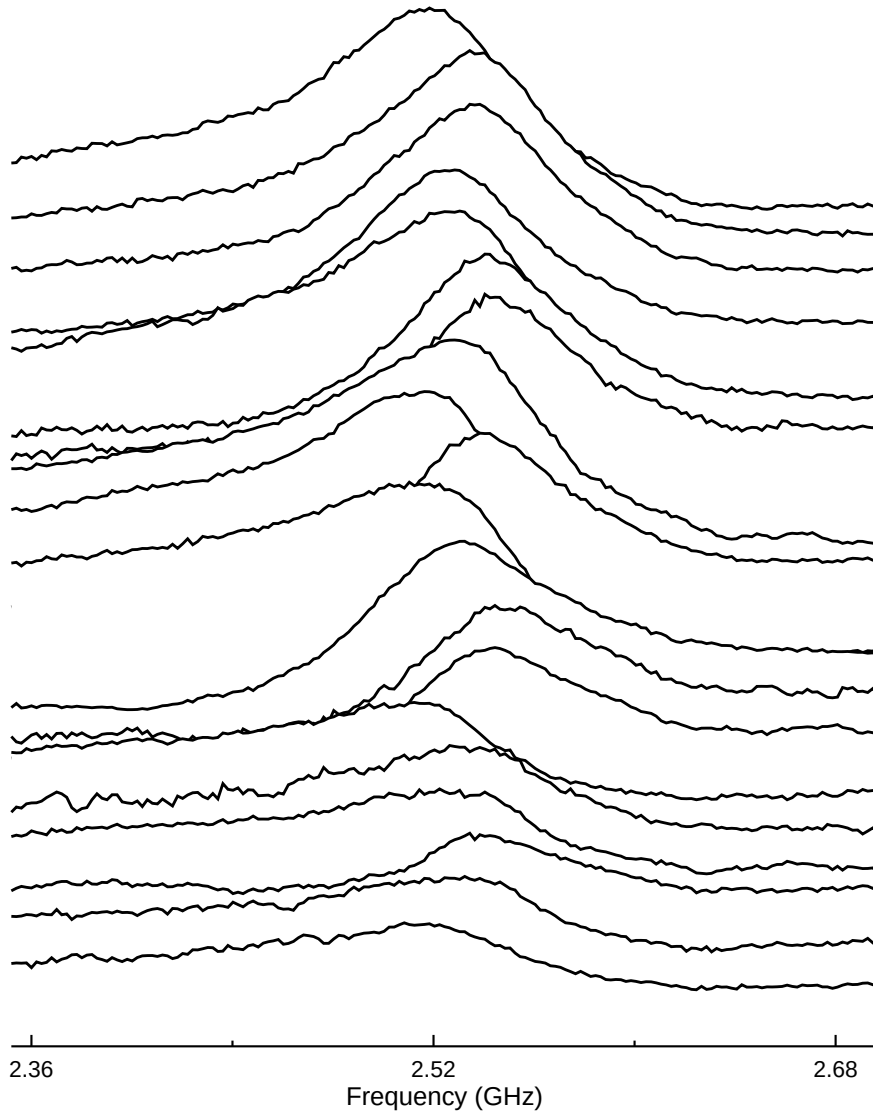


Figure B.3: All measured Brillouin spectra for 1 mm CS_2 at detuning steps of 0.25 GHz from 10 GHz (top spectrum) to 14 GHz (bottom spectrum). Each trace is offset for clarity.

To illustrate the strong distinction in line-shape of a spectra resulting from a positive vs. negative q value, we focus on two particular detunings that yielded notably skewed line shapes: 11 GHz and 13 GHz. Figures B.4 and B.5 compare the spectra for these two detunings normalized relative to the slightly larger

peak amplitude of the 11 GHz spectra. The line-shape of the 11 GHz spectrum exhibits a sharper rise on the higher-frequency side and a gentler roll-off on the lower-frequency side, indicative of $q < 0$, whereas that of the 13 GHz spectrum is skewed oppositely, featuring a sharper low-frequency side and a softer high-frequency roll-off, suggesting $q > 0$. Figure B.4 shows these two spectra with uncertainty-weighted Fano function fits applied, with the corresponding reduced χ^2 values reported in the legend. The Fano fits yield reduced χ^2 values of 2.45 and 8.41 for the 11 GHz and 13 GHz spectra, respectively (reduced χ^2 values near unity indicate a good fit to the data). Figure B.5 shows these same spectra with naïve Lorentz function fits applied and their corresponding reduced χ^2 evaluations of goodness-of-fit. These Lorentzian fits yield reduced χ^2 values of 39.45 and 146.5 for the 11 GHz and 13 GHz spectra, respectively, indicating that the Lorentzian function is a very poor fit to the data.. The poor fit of the Lorentzian function is due to its inherent symmetry, whereas the underlying data exhibit strongly asymmetric lineshapes. These results clearly demonstrate the superiority of the Fano model in capturing the asymmetry of small signals produced by the instrument due to Fano interference with the background continuum. This, in turn, emphasizes the importance of applying a Fano fit function when asymmetries arise to accurately extract valuable spectra parameters such as peak amplitude, center frequency, and linewidth from the data.

Notably, in the 11 GHz case, our Fano fit reveals a local amplitude slightly higher than what the Lorentzian fit suggests, sometimes referred to as a “peak boost.” In essence, partial *constructive* interference between the discrete Brillouin response and the broad continuum locally raises the amplitude, although it does not imply any net energy gain. As mentioned in *Fano-Resonant Asymmetries at Small Signals* (Section 3.5), this effect can aid in detecting weak resonances if the background is not too noisy. One could, in principle, tune the phase relationship to maximize this interference near the resonance, possibly producing a sharper or taller peak for certain values of q than would be achieved without interference with the background. This Fano interference-tuning of the discrete mode relative to the background can be done dynamically via adjustment of the probe laser wavelength and, critically, can be adjusted independently from the phase-matching bandwidth tuning (pump-probe detuning). This ability to dynamically adjust the discrete-continuum interference is an elegant and notable feature, as in typical systems this is adjusted via changes in physical geometry or material doping of the sample.^{61,62,111}

1 mm CS₂ CABS

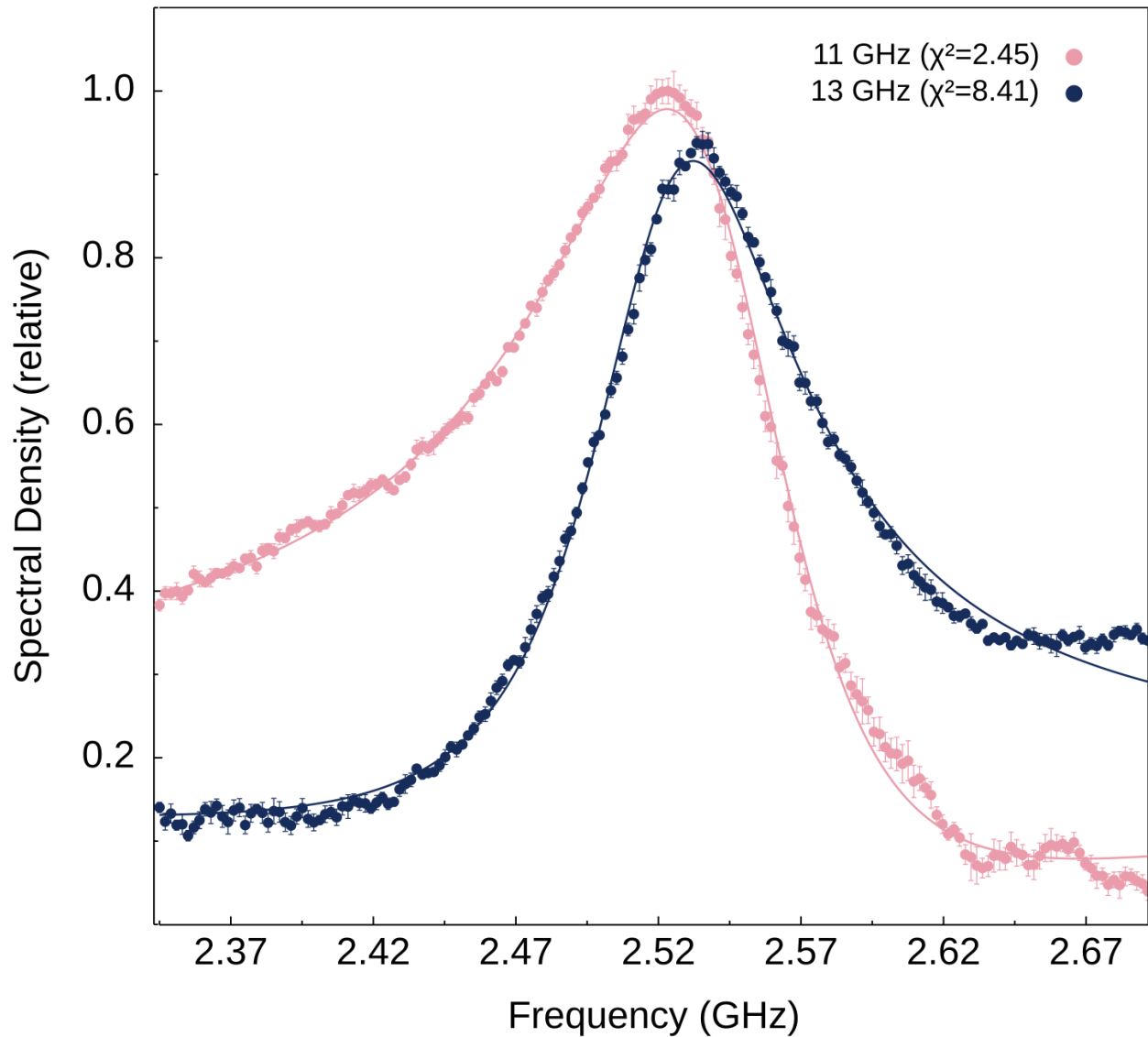


Figure B.4: Comparison of representative spectra at 11 GHz and 13 GHz, showing the positive vs. negative q asymmetry in 1 mm CS₂. A Fano function fit has been applied to each spectra, with χ^2 value for each fit listed in the plot legend.

1 mm CS₂ CABS

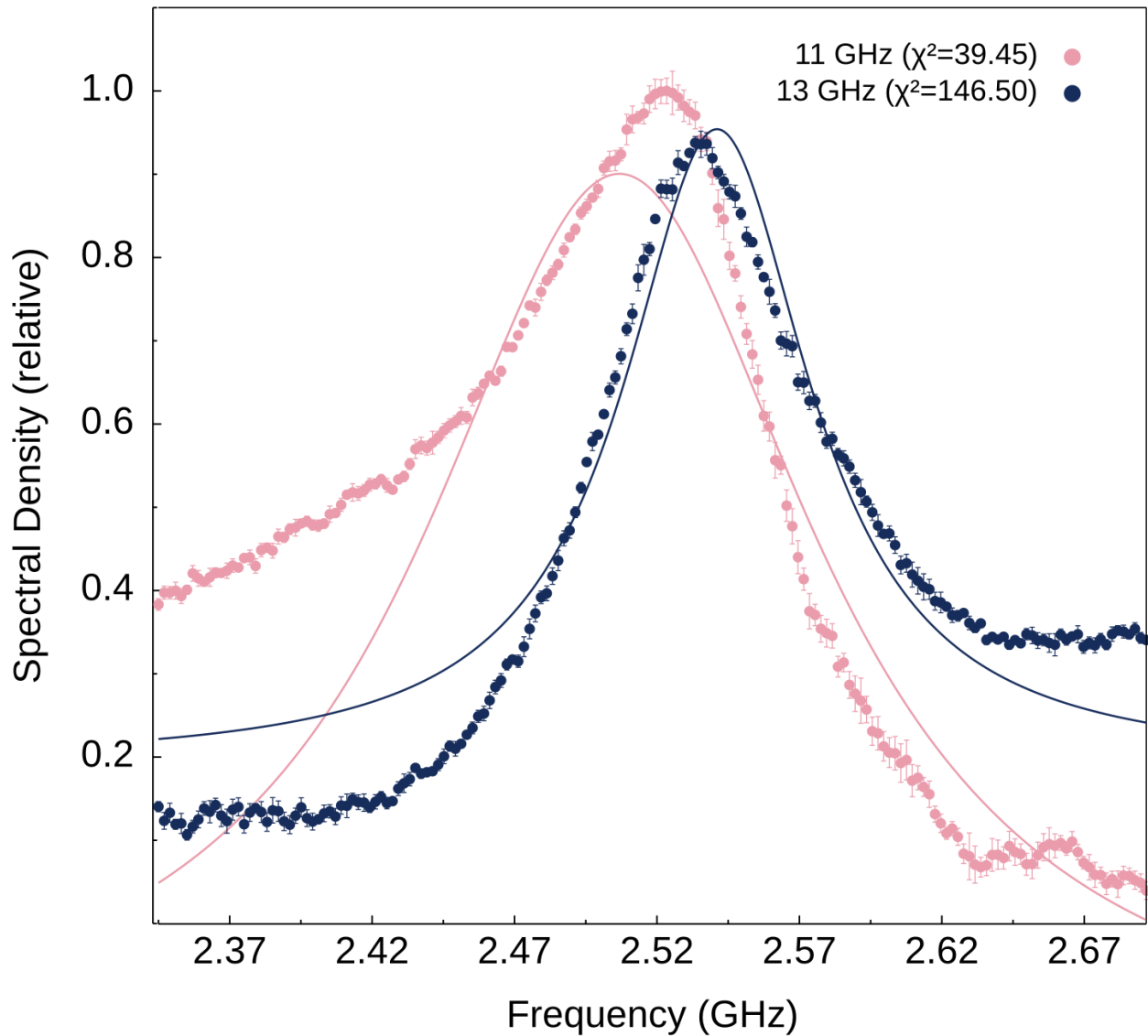


Figure B.5: Comparison of representative spectra at 11 GHz and 13 GHz, showing the positive vs. negative q asymmetry in 1 mm CS₂. Here, a naïve Lorentz function fit has been applied to each spectra, with χ^2 value for each fit listed in the plot legend. These spectra show strong Fano-resonant asymmetry and thus the standard Lorentz function offers a poor fit for these spectra, quantified by the χ^2 evaluation metric for goodness of fit as compared to the same evaluation of the Fano function fit.

To better convey the cyclical evolution of the 75 measured UHNA3 spectra from Experiment A, several animated GIFs have been generated. The following is a link to the GitHub repository which hosts these files, along with all raw data, measurement logs, and plots generated in support of this work (see See Appendix C):

<https://github.com/HamletTheHamster/Plotting-Data-in-Go>

The reader will find several GIFs which step through each spectrum in ascending pump–probe detuning at various frame rates. Readers are encouraged to view them for an animated perspective on how the spectra evolve with increasing pump–probe detuning, with special attention to transitions between Lorentzian and Fano-distorted line shapes.

B.4 CoBS Mini Experiment: Equal Contribution of Pump, Stokes, and Probe

Equation 3.1 gives the somewhat unintuitive result that the powers of the Pump, Stokes, and Probe waves contribute equally to the resulting scattered power of the Signal and invites verification with a miniexperiment. Initially, this experiment was motivated by a practical consideration: determination of whether the placement of a high power amplifier on any specific line of the setup (Pump, Stokes, or Probe) would offer any advantage over another.

To test this, we conducted a controlled experiment with a 1 mm CS₂ sample. For each measurement, one of the three source powers (Pump, Stokes, or Probe) was systematically reduced by 75% while holding the others constant and ensuring consistent experimental conditions across trials. Table B.3 shows the respective powers for each source during the three measurements, along with the multiplicative total contribution of the three powers for each measurement towards the generation of scattered power of the Signal.

Measurement	Pump Power (mW)	Stokes Power (mW)	Probe Power (mW)	Total (mW ³)
Pump Lower	19.190	32.210	54.560	3.372×10^4
Stokes Lower	76.600	8.020	54.650	3.359×10^4
Probe Lower	76.600	32.530	13.480	3.359×10^4

Table B.3: Power values for each source (Pump, Stokes, Probe) across the three measurements, with the multiplicative total power for each setup.

Figure B.6 displays the average results from these three measurements, plotted with error bars representing one standard deviation of the mean. For increased certainty, Figure B.7 presents the same data with error bars extended to two standard deviations, providing additional confidence in the reproducibility of the results. This experiment confirms that the scattered Signal power indeed depends equally on each of the three contributing wave powers, as expected from the theoretical framework. Consequently, boosting the power of any of the three sources affects the Signal power equally, allowing flexibility in pragmatic design across any of the three lines. Ultimately, this result reinforces the reliability of Equation 3.1 for predicting Signal power across a range of power distributions within practical settings.

1 mm CS2 CABS

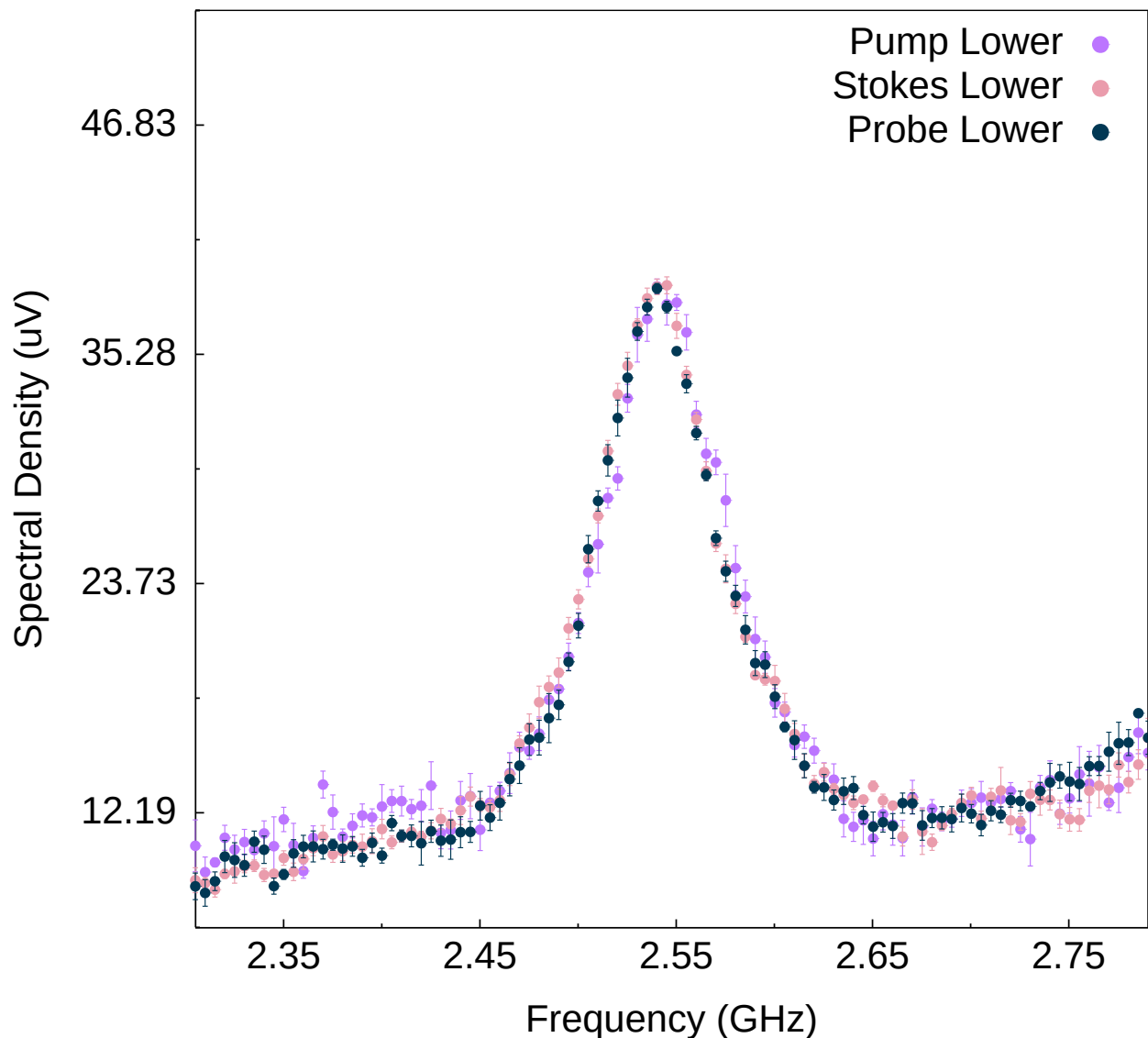


Figure B.6: Signal power contributions with error bars representing one standard deviation of the mean for each measurement.

1 mm CS2 CABS

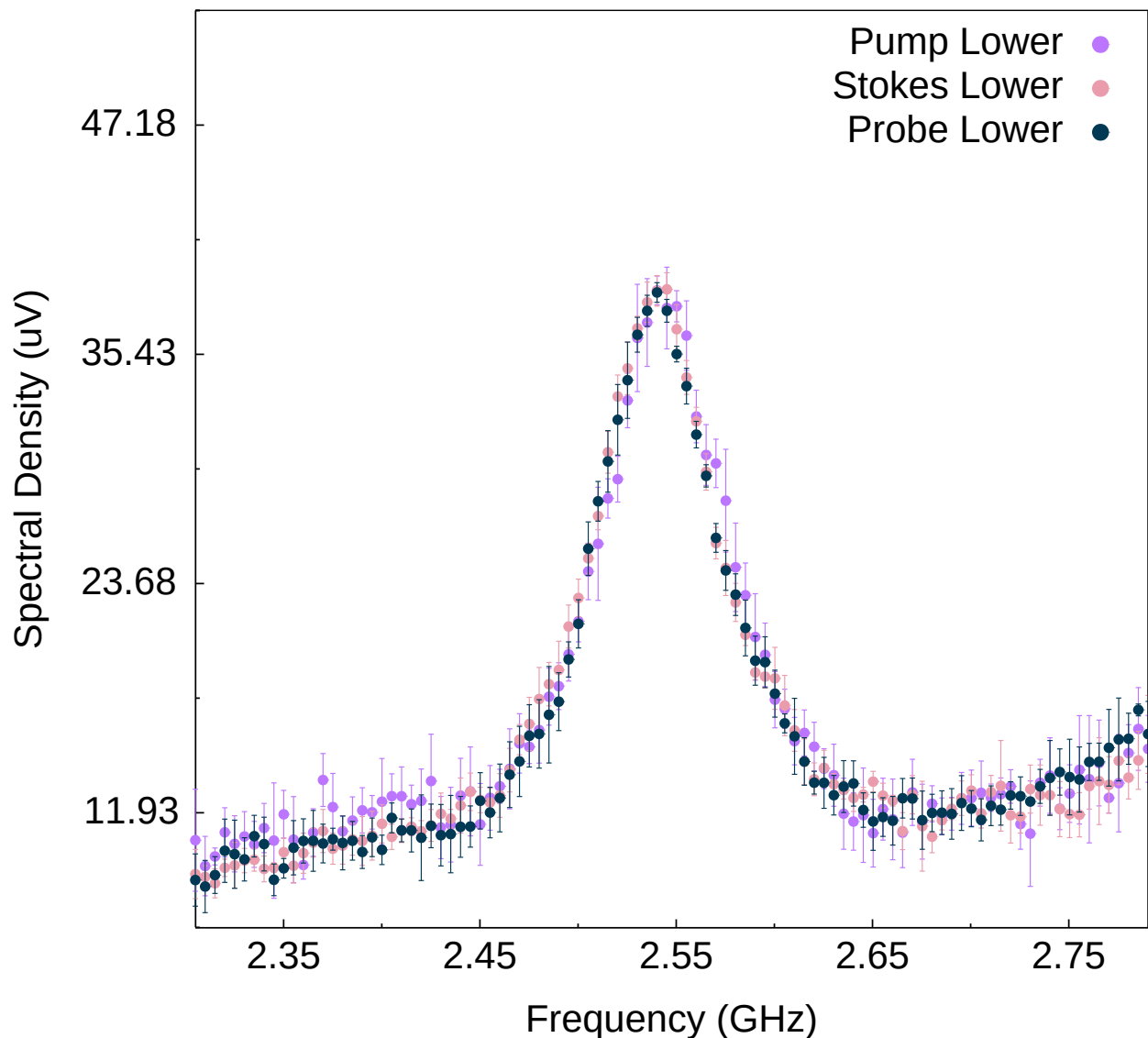


Figure B.7: Signal power contributions with error bars extended to two standard deviations of the mean for each measurement.

B.5 Measurement Protocol

Appendix C

Code and Data Availability

C.1 Plotting Data In Go

Data plots presented in this dissertation were generated using custom programs written by the author in Golang or Python. The source code for these program, as well as all data collected and plots generated in support of the work presented in this dissertation, are publicly available on GitHub via the following link:

<https://github.com/HamletTheHamster/Plotting-Data-in-Go>

A video visualizing the evolution of data collection and development of functionality of the plotting program is available on YouTube:

<https://www.youtube.com/watch?v=PdoWVoJx2Vg>

References

- [1] Joel N Johnson, Danielle R Haverkamp, Yi-Hsin Ou, Khanh Kieu, Nils T Otterstrom, Peter T Rakich, and Ryan O Behunin. Laser cooling of traveling-wave phonons in an optical fiber. *Physical Review Applied*, 20(3):034047, 2023.
- [2] Lord Rayleigh. On the light from the sky, its polarization and colour. *Phil Mag*, 41:274, 1871.
- [3] Robert W Boyd. *Nonlinear Optics*. Academic Press, 2020.
- [4] eg PA Franken, Alan E Hill, CW el Peters, and Gabriel Weinreich. Generation of optical harmonics. *Physical review letters*, 7(4):118, 1961.
- [5] Theodore H Maiman. Stimulated optical radiation in ruby. *nature*, 187(4736):493–494, 1960.
- [6] Theodor W Hänsch and Arthur L Schawlow. Cooling of gases by laser radiation. *Optics Communications*, 13(1):68–69, 1975.
- [7] Mike H Anderson, Jason R Ensher, Michael R Matthews, Carl E Wieman, and Eric A Cornell. Observation of bose-einstein condensation in a dilute atomic vapor. *science*, 269(5221):198–201, 1995.
- [8] Andrew D Ludlow, Martin M Boyd, Jun Ye, Ekkehard Peik, and Piet O Schmidt. Optical atomic clocks. *Reviews of Modern Physics*, 87(2):637, 2015.
- [9] Junwei Meng, Alexander R Albrecht, Aram Gragossian, Eric Lee, Azzurra Volpi, Mohammadreza Ghasemkhani, Markus P Hehlen, Richard I Epstein, and Mansoor Sheik-Bahae. Realization of an all-solid-state cryocooler using optical refrigeration. In *Tri-Technology Device Refrigeration (TTDR) III*, volume 10626, pages 64–72. SPIE, 2018.
- [10] Richard I Epstein, Melvin I Buchwald, Bradley C Edwards, Timothy R Gosnell, and Carl E Mungan. Observation of laser-induced fluorescent cooling of a solid. *Nature*, 377(6549):500–503, 1995.
- [11] Jasper Chan, TP Alegre, Amir H Safavi-Naeini, Jeff T Hill, Alex Krause, Simon Gröblacher, Markus Aspelmeyer, and Oskar Painter. Laser cooling of a nanomechanical oscillator into its quantum ground state. *Nature*, 478(7367):89–92, 2011.
- [12] Markus Aspelmeyer, Tobias J Kippenberg, and Florian Marquardt. Cavity optomechanics. *Reviews of Modern Physics*, 86(4):1391, 2014.
- [13] Gaurav Bahl, Matthew Tomes, Florian Marquardt, and Tal Carmon. Observation of spontaneous brillouin cooling. *Nature Physics*, 8(3):203–207, 2012.
- [14] Nils T Otterstrom, Ryan O Behunin, Eric A Kittlaus, and Peter T Rakich. Optomechanical cooling in a continuous system. *Physical Review X*, 8(4):041034, 2018.
- [15] Changlong Zhu and Birgit Stiller. Dynamic brillouin cooling for continuous optomechanical systems. *Materials for Quantum Technology*, 3(1):015003, 2023.
- [16] Heedeuk Shin, Jonathan A Cox, Robert Jarecki, Andrew Starbuck, Zheng Wang, and Peter T Rakich. Control of coherent information via on-chip photonic–phononic emitter–receivers. *Nature communications*, 6(1):6427, 2015.

- [17] Kazi S Abedin. Observation of strong stimulated brillouin scattering in single-mode as 2 se 3 chalcogenide fiber. *Optics Express*, 13(25):10266–10271, 2005.
- [18] Victor A Vysloukh et al. Nonlinear fiber optics. *Phys. Usp.*, 33:400–400, 1990.
- [19] Mamoru Endo, Shota Kimura, Shuntaro Tani, and Yohei Kobayashi. Coherent control of acoustic phonons in a silica fiber using a multi-ghz optical frequency comb. *Communications Physics*, 4(1):73, 2021.
- [20] K Kieu, L Schneebeli, RA Norwood, and N Peyghambarian. Integrated liquid-core optical fibers for ultra-efficient nonlinear liquid photonics. *Optics express*, 20(7):8148–8154, 2012.
- [21] Ryan O Behunin, Yi-Hsin Ou, and Khanh Kieu. Spontaneous forward brillouin scattering in carbon disulfide. *Physical Review A*, 99(6):063826, 2019.
- [22] Zhuoming Zhang, Yang Ding, Peter J Pauzauskie, Mansoor Sheik-Bahae, Denis V Seletskiy, and Masaru Kuno. Experimental minimum of condensed-phase optical refrigeration. *arXiv preprint arXiv:2408.02977*, 2024.
- [23] Laura Blázquez Martínez, Philipp Wiedemann, Changlong Zhu, Andreas Geilen, and Birgit Stiller. Optoacoustic cooling of traveling hypersound waves. *Physical Review Letters*, 132(2):023603, 2024.
- [24] Seunghwi Kim and Gaurav Bahl. Role of optical density of states in brillouin optomechanical cooling. *Optics Express*, 25(2):776–784, 2017.
- [25] Moritz Merklein, Birgit Stiller, Khu Vu, Stephen J Madden, and Benjamin J Eggleton. A chip-integrated coherent photonic-phononic memory. *nature Communications*, 8(1):574, 2017.
- [26] Changlong Zhu, Claudiu Genes, and Birgit Stiller. Optoacoustic entanglement in a continuous brillouin-active solid state system. *Physical Review Letters*, 133(20):203602, 2024.
- [27] Xuedong Hu and Franco Nori. Squeezed phonon states: modulating quantum fluctuations of atomic displacements. *Physical review letters*, 76(13):2294, 1996.
- [28] Riccardo Manenti, Anton F Kockum, Andrew Patterson, Tanja Behrle, Joseph Rahamim, Giovanna Tancredi, Franco Nori, and Peter J Leek. Circuit quantum acoustodynamics with surface acoustic waves. *Nature communications*, 8(1):975, 2017.
- [29] Hugo Michiel Doeleman, Tom Schatteburg, R Benevides, S Vollenweider, Dorotea Macri, and Yiwen Chu. Brillouin optomechanics in the quantum ground state. *Physical Review Research*, 5(4):043140, 2023.
- [30] RY Chiao, Ch H Townes, and BP Stoicheff. Stimulated brillouin scattering and coherent generation of intense hypersonic waves. *Physical review letters*, 12(21):592, 1964.
- [31] Benjamin J Eggleton, Christopher G Poulton, and Ravi Pant. Inducing and harnessing stimulated brillouin scattering in photonic integrated circuits. *Advances in Optics and Photonics*, 5(4):536–587, 2013.
- [32] AA Fotiadi, DA Korobko, and IO Zolotovskii. Brillouin lasers and sensors: Trends and possibilities. *Optoelectronics, Instrumentation and Data Processing*, 59(1):66–76, 2023.
- [33] Andrey Kobyakov, Michael Sauer, and Dipak Chowdhury. Stimulated brillouin scattering in optical fibers. *Advances in optics and photonics*, 2(1):1–59, 2009.
- [34] EP Ippen and RH Stolen. Stimulated brillouin scattering in optical fibers. *Applied Physics Letters*, 21(11):539–541, 1972.
- [35] Sergio Speziale, Hauke Marquardt, and Thomas S Duffy. Brillouin scattering and its application in geosciences. *Reviews in Mineralogy and Geochemistry*, 78(1):543–603, 2014.

- [36] Francesca Palombo and Daniele Fioretto. Brillouin light scattering: applications in biomedical sciences. *Chemical reviews*, 119(13):7833–7847, 2019.
- [37] JG Dil. Brillouin scattering in condensed matter. *Reports on Progress in Physics*, 45(3):285, 1982.
- [38] Benjamin J Eggleton, Christopher G Poulton, Peter T Rakich, Michael J Steel, and Gaurav Bahl. Brillouin integrated photonics. *Nature Photonics*, 13(10):664–677, 2019.
- [39] Robert Prevedel, Alba Diz-Muñoz, Giancarlo Ruocco, and Giuseppe Antonacci. Brillouin microscopy: an emerging tool for mechanobiology. *Nature methods*, 16(10):969–977, 2019.
- [40] Christina Conrad, Kelsey M Gray, Kimberly M Stroka, Imran Rizvi, and Giuliano Scarcelli. Mechanical characterization of 3d ovarian cancer nodules using brillouin confocal microscopy. *Cellular and molecular bioengineering*, 12:215–226, 2019.
- [41] Peter T Rakich, Charles Reinke, Ryan Camacho, Paul Davids, and Zheng Wang. Giant enhancement of stimulated brillouin scattering in the subwavelength limit. *Physical Review X*, 2(1):011008, 2012.
- [42] Flavien Gyger, Junqiu Liu, Fan Yang, Jijun He, Arslan S Raja, Rui Ning Wang, Sunil A Bhave, Tobias J Kippenberg, and Luc Thévenaz. Observation of stimulated brillouin scattering in silicon nitride integrated waveguides. *Physical review letters*, 124(1):013902, 2020.
- [43] Linfeng Yu, Chukun Huang, Ming Cheng, Kang Wang, Haotian Shi, Qiang Huang, and Junqiang Sun. On-chip stimulated brillouin scattering. *Chinese Optics Letters*, 22(2):020031, 2024.
- [44] Heedeuk Shin, Wenjun Qiu, Robert Jarecki, Jonathan A Cox, Roy H Olsson, Andrew Starbuck, Zheng Wang, and Peter T Rakich. Tailorable stimulated brillouin scattering in nanoscale silicon waveguides. *Nature communications*, 4(1):1–10, 2013.
- [45] Raphaël Van Laer, Bart Kuyken, Dries Van Thourhout, and Roel Baets. Interaction between light and highly confined hypersound in a silicon photonic nanowire. *Nature Photonics*, 9(3):199–203, 2015.
- [46] Eric A Kittlaus, Heedeuk Shin, and Peter T Rakich. Large brillouin amplification in silicon. *Nature Photonics*, 10(7):463–467, 2016.
- [47] Lionel Djadalojee, Albane Douillet, and Jules Grucker. Stimulated brillouin gain spectroscopy in a confined spatio-temporal domain (30 μm , 170 ns). *The European Physical Journal Applied Physics*, 89(3):30701, 2020.
- [48] Vitalyi E Gusev and Pascal Ruello. Advances in applications of time-domain brillouin scattering for nanoscale imaging. *Applied Physics Reviews*, 5(3), 2018.
- [49] A Gerakis, MN Shneider, and PF Barker. Coherent brillouin scattering. *Optics Express*, 19(24):24046–24054, 2011.
- [50] Ravi Pant, Enbang Li, D-Y Choi, CG Poulton, Stephen J Madden, Barry Luther-Davies, and Benjamin J Eggleton. Cavity enhanced stimulated brillouin scattering in an optical chip for multiorder stokes generation. *Optics letters*, 36(18):3687–3689, 2011.
- [51] Eric A Kittlaus, Nils T Otterstrom, and Peter T Rakich. On-chip inter-modal brillouin scattering. *Nature communications*, 8(1):15819, 2017.
- [52] Omer Shlomovits, Tomi Langer, and Moshe Tur. The effect of source phase noise on stimulated brillouin amplification. *Journal of Lightwave Technology*, 33(12):2639–2645, 2015.
- [53] PD Maker, RW Terhune, M Nisenoff, and CM Savage. Effects of dispersion and focusing on the production of optical harmonics. *Physical review letters*, 8(1):21, 1962.
- [54] RO Behunin, P Kharel, WH Renninger, H Shin, F Carter, E Kittlaus, and PT Rakich. Long-lived guided phonons in fiber by manipulating two-level systems. *arXiv preprint arXiv:1501.04248*, 2015.

- [55] Marc Nikles, Luc Thevenaz, and Philippe A Robert. Brillouin gain spectrum characterization in single-mode optical fibers. *Journal of Lightwave Technology*, 15(10):1842–1851, 1997.
- [56] Ugo Fano. Effects of configuration interaction on intensities and phase shifts. *Physical review*, 124(6):1866, 1961.
- [57] Mikhail F Limonov, Mikhail V Rybin, Alexander N Poddubny, and Yuri S Kivshar. Fano resonances in photonics. *Nature photonics*, 11(9):543–554, 2017.
- [58] Mikhail F Limonov. Fano resonance for applications. *Advances in optics and photonics*, 13(3):703–771, 2021.
- [59] Martin Kroner, Alexander O Govorov, Sebastian Remi, Benjamin Biedermann, Stefan Seidl, Antonio Badolato, Pierre M Petroff, Wei Zhang, R Barbour, BD Gerardot, et al. The nonlinear fano effect. *Nature*, 451(7176):311–314, 2008.
- [60] Andrey E Miroshnichenko, Sergej Flach, and Yuri S Kivshar. Fano resonances in nanoscale structures. *Reviews of Modern Physics*, 82(3):2257–2298, 2010.
- [61] Joo Hwan Ko, Jin-Hwi Park, Young Jin Yoo, Sehui Chang, Jiwon Kang, Aiguo Wu, Fang Yang, Sejeong Kim, Hae-Gon Jeon, and Young Min Song. Full-control and switching of optical fano resonance by continuum state engineering. *Advanced Science*, 10(32):2304310, 2023.
- [62] Linpeng Gu, Liang Fang, Hanlin Fang, Juntao Li, Jianbang Zheng, Jianlin Zhao, Qiang Zhao, and Xuetao Gan. Fano resonance lineshapes in a waveguide-microring structure enabled by an air-hole. *APL photonics*, 5(1), 2020.
- [63] Tobias J Kippenberg and Kerry J Vahala. Cavity optomechanics: back-action at the mesoscale. *science*, 321(5893):1172–1176, 2008.
- [64] Kerry Vahala, Maximilian Herrmann, Sebastian Knünz, Valentin Batteiger, Guido Saathoff, TW Hänsch, and Th Udem. A phonon laser. *Nature Physics*, 5(9):682–686, 2009.
- [65] Krishna C Balram, Marcelo I Davanço, Jin Dong Song, and Kartik Srinivasan. Coherent coupling between radiofrequency, optical and acoustic waves in piezo-optomechanical circuits. *Nature photonics*, 10(5):346–352, 2016.
- [66] A Schliesser and TJ Kippenberg. Cavity optomechanics with whispering-gallery-mode microresonators. In *Cavity Optomechanics: Nano-and Micromechanical Resonators Interacting with Light*, pages 121–148. Springer, 2014.
- [67] Serge Galliou, Maxim Goryachev, Roger Bourquin, Philippe Abbé, Jean Pierre Aubry, and Michael E Tobar. Extremely low loss phonon-trapping cryogenic acoustic cavities for future physical experiments. *Scientific reports*, 3(1):2132, 2013.
- [68] Ravi Pant, Christopher G Poulton, Duk-Yong Choi, Hannah Mcfarlane, Samuel Hile, Enbang Li, Luc Thevenaz, Barry Luther-Davies, Stephen J Madden, and Benjamin J Eggleton. On-chip stimulated brillouin scattering. *Optics express*, 19(9):8285–8290, 2011.
- [69] Manuel Cardona and Roberto Merlin. *Light scattering in solids IX*. Springer, 2007.
- [70] John R Ferraro. *Introductory raman spectroscopy*. Elsevier, 2003.
- [71] Reuben Shuker and Robert W Gammon. Raman-scattering selection-rule breaking and the density of states in amorphous materials. *Physical Review Letters*, 25(4):222, 1970.
- [72] E Duval, A Boukenter, and T Achibat. Vibrational dynamics and the structure of glasses. *Journal of Physics: Condensed Matter*, 2(51):10227, 1990.
- [73] G Winterling. Very-low-frequency raman scattering in vitreous silica. *Physical Review B*, 12(6):2432, 1975.

- [74] Robert John Nemanich. Low-frequency inelastic light scattering from chalcogenide glasses and alloys. *Physical Review B*, 16(4):1655, 1977.
- [75] AJ Martin and W Brenig. Model for brillouin scattering in amorphous solids. *physica status solidi (b)*, 64(1):163–172, 1974.
- [76] Valeriy K Malinovsky and Alexei P Sokolov. The nature of boson peak in raman scattering in glasses. *Solid state communications*, 57(9):757–761, 1986.
- [77] U Buchenau, M Prager, N Nücker, AJ Dianoux, N Ahmad, and WA Phillips. Low-frequency modes in vitreous silica. *Physical Review B*, 34(8):5665, 1986.
- [78] VK Malinovsky, VN Novikov, and AP Sokolov. Investigation of structural correlations in disordered materials by raman scattering measurements. *Journal of Non Crystalline Solids*, 90(1):485–488, 1987.
- [79] A.I Chumakov, Giulio Monaco, A Monaco, W.A Crichton, A Bosak, R Rüffer, A Meyer, F Kargl, Lucia Comez, Daniele Fioretto, et al. Equivalence of the boson peak in glasses to the transverse acoustic van hove singularity in crystals. *Physical review letters*, 106(22):225501, 2011.
- [80] Horace Lamb. On the vibrations of an elastic sphere. *Proceedings of the London Mathematical Society*, 1(1):189–212, 1881.
- [81] E Duval, A Boukenter, and B Champagnon. Vibration eigenmodes and size of microcrystallites in glass: observation by very-low-frequency raman scattering. *Physical Review Letters*, 56(19):2052, 1986.
- [82] WH Renninger, P Kharel, RO Behunin, and PT Rakich. Bulk crystalline optomechanics. *Nature Physics*, 14(6):601–607, 2018.
- [83] Gregory S MacCabe, Hengjiang Ren, Jie Luo, Justin D Cohen, Hengyun Zhou, Alp Sipahigil, Mohammad Mirhosseini, and Oskar Painter. Nano-acoustic resonator with ultralong phonon lifetime. *Science*, 370(6518):840–843, 2020.
- [84] Jas S Sanghera, Leslie B Shaw, Paul Pureza, Vinh Q Nguyen, Dan Gibson, Lynda Busse, Ishwar D Aggarwal, Catalin M Florea, and Frederic H Kung. Nonlinear properties of chalcogenide glass fibers. *International Journal of Applied Glass Science*, 1(3):296–308, 2010.
- [85] Mark A Dubinskii and Larry D Merkle. Teo₂: Solid-state sbs material with exceptionally high gain. In *Advanced Solid-State Photonics*, page 451. Optica Publishing Group, 2004.
- [86] G Enright and BP Stoicheff. Depolarized brillouin spectrum of liquid cs₂. *The Journal of Chemical Physics*, 60(6):2536–2539, 1974.
- [87] Robert W Coakley and Robert W Detenbeck. Brillouin-scattering measurements of the acoustic absorption coefficient in liquid cs 2. *JOSA*, 65(1):6–9, 1975.
- [88] Naoya Uchida and Yoshiro Ohmachi. Elastic and photoelastic properties of teo₂ single crystal. *Journal of Applied Physics*, 40(12):4692–4695, 1969.
- [89] H Schweppe. Elastic and piezoelectric properties of paratellurite (teo₂). *Ultrasonics*, 8(2):84–87, 1970.
- [90] Yoshiro Ohmachi, Naoya Uchida, and Nobukazu Niizeki. Acoustic wave propagation in teo 2 single crystal. *The Journal of the Acoustical Society of America*, 51(1B):164–168, 1972.
- [91] PS Peercy, IJ Fritz, and GA Samara. Temperature and pressure dependences of the properties and phase transition in paratellurite (teo₂): Ultrasonic, dielectric and raman and brillouin scattering results. *Journal of Physics and Chemistry of Solids*, 36(10):1105–1122, 1975.
- [92] Romain Fleury, DL Sounas, and Andrea Alu. Non-reciprocal optical mirrors based on spatio-temporal acousto-optic modulation. *Journal of Optics*, 20(3):034007, 2018.
- [93] Dan Owen Harris. Multichannel acousto-optic crossbar switch. *Applied optics*, 30(29):4245–4256, 1991.

- [94] Naoya Uchida. Optical properties of single-crystal paratellurite (te o 2). *Physical Review B*, 4(10):3736, 1971.
- [95] D Heiman, DS Hamilton, and RW Hellwarth. Brillouin scattering measurements on optical glasses. *Physical Review B*, 19(12):6583, 1979.
- [96] JA Bucaro and HD Dardy. High-temperature brillouin scattering in fused quartz. *Journal of Applied Physics*, 45(12):5324–5329, 1974.
- [97] Humphrey J Maris. Phonon propagation with isotope scattering and spontaneous anharmonic decay. *Physical Review B*, 41(14):9736, 1990.
- [98] Bertram Alexander Auld. *Acoustic fields and waves in solids*. Rипol Klassik, 1973.
- [99] Arkadiusz Ciesielski, Lukasz Skowronski, Wojciech Pacuski, and Tomasz Szoplik. Permittivity of ge, te and se thin films in the 200–1500 nm spectral range. predicting the segregation effects in silver. *Materials Science in Semiconductor Processing*, 81:64–67, 2018.
- [100] VI Balakshii, VB Voloshinov, GA Knyazev, and LA Kulakova. Investigation into the acoustooptic properties of tellurium crystals by anisotropic diffraction of light. *Technical Physics*, 53:1336–1343, 2008.
- [101] Siqi Lin, Wen Li, Zhiwei Chen, Jiawen Shen, Binghui Ge, and Yanzhong Pei. Tellurium as a high-performance elemental thermoelectric. *Nature communications*, 7(1):10287, 2016.
- [102] VB Voloshinov, VS Khorkin, LA Kulakova, and N Gupta. Optic, acoustic and acousto-optic properties of tellurium in close-to-axis regime of diffraction. *Journal of Physics Communications*, 1(2):025006, 2017.
- [103] VS Khorkin, VB Voloshinov, AI Efimova, and LA Kulakova. Acousto-optic properties of germanium-, selenium-, silicon-, and tellurium-based alloys. *Optics and Spectroscopy*, 128:244–249, 2020.
- [104] VB Voloshinov, VI Balakshy, LA Kulakova, and N Gupta. Acousto-optic properties of tellurium that are useful in anisotropic diffraction. *Journal of optics a: pure and applied optics*, 10(9):095002, 2008.
- [105] VF Kozhevnikov, WB Payne, JK Olson, A Allen, and PC Taylor. Sound velocity in liquid and glassy selenium. *Journal of non-crystalline solids*, 353(32-40):3254–3259, 2007.
- [106] Patricia A Hartig and Joseph J Loferski. Infrared index of refraction of tellurium crystals. *Journal of the Optical Society of America*, 44(1):17–18, 1954.
- [107] Andreas Geilen, Alexandra Popp, Debayan Das, Saher Junaid, Christopher G Poulton, Mario Chemnitz, Christoph Marquardt, Markus A Schmidt, and Birgit Stiller. Extreme thermodynamics in nanolitre volumes through stimulated brillouin–mandelstam scattering. *Nature Physics*, 19(12):1805–1812, 2023.
- [108] I Roch, Ph Bidaud, D Collard, and Lionel Buchaillot. Fabrication and characterization of an su-8 gripper actuated by a shape memory alloy thin film. *Journal of Micromechanics and Microengineering*, 13(2):330, 2003.
- [109] Robert W Boyd, Kazimierz Rzaewski, and Paul Narum. Noise initiation of stimulated brillouin scattering. *Physical review A*, 42(9):5514, 1990.
- [110] Prashanta Kharel, Ryan O Behunin, William H Renninger, and Peter T Rakich. Noise and dynamics in forward brillouin interactions. *Physical Review A*, 93(6):063806, 2016.
- [111] D Rieger, S Günzler, M Spiecker, A Nambisan, W Wernsdorfer, and IM Pop. Fano interference in microwave resonator measurements. *Physical Review Applied*, 20(1):014059, 2023.